Magmatic development of the Jan Mayen - East Greenland area, NE Atlantic

Pingchuan Tan

Preface

The work presented in this PhD thesis is a result from my employment as a PhD candidate at The Centre for Earth Evolution and Dynamics, University of Oslo, during 2014-2018. The thesis project targets an area in the NE Atlantic ocean with substantial on-axis and off-axis volcanism. The area was not well constrained, and geophysical investigations were mostly lacking. The thesis consists of an introduction of the project, a geological background, data and methods, and three scientific papers. The first paper, which is published in the *Journal of Geophysical Research: Solid earth*, presented the crustal model of the Eggvin Bank based on the seismic refraction data collected in 2011. In the second paper, we present basement and sedimentary pattern across the WJMFZ and the Logi Ridge based on six single channel seismic reflection lines collected by University of Bergen and University of Oslo, and two multi channel seismic reflection lines by Norwegian Petroleum Directorate (NPD) in 2011. The third paper, accepted by *Journal of Geophysical Research: Solid earth*, presented a 3D lithospheric density model over the greater Jan Mayen-East Greenland region. The modeling was mainly completed in Potsdam during the spring semester in 2016 in collaboration with Dr. Judith Sippel and Christian Meeßen at GeoForschungsZentrum (GFZ), Potsdam, Germany. The PhD study was supported by a 4-year doctoral fellowship from University of Oslo.

Acknowledgements

Contents

Contents

Part I

Introduction

1 Introduction

The Cenozoic igneous activity in the North Atlantic region is extensive outside of Iceland (Fig. 1.1). Both the Northeast Atlantic Igneous Province (NAIP) (e.g. *White*, 1997; *Eldholm and Grue*, 1994; *Voss and Jokat*, 2007) and the Faeroe-Iceland-Greenland Ridge (e.g. *Eldholm and Grue*, 1994) (Fig. 1.1) are widely considered to be associated with the evolution of the Iceland plume. However, far less is known to what extent more distal igneous areas also are affected by plume activity. Jan Mayen has an active volcano derived from deep, low-degree mantle melting (e.g. *Trønnes et al.*, 1999). North of Jan Mayen, the Jan Mayen Plateau has an up to 12 km thick oceanic crust (*Kandilarov et al.*, 2012). West of Jan Mayen, the Eggvin Bank is an unusually shallow area, where the majority of the seamounts are located between Northern Kolbeinsey Ridge (NKR) and Jan Mayen. It is confined to the south by a small offset on the spreading ridge, whereas the northern boundary is the West Jan Mayen Fracture Zone (WJMFZ), an active transform fault between the Kolbeinsey and Mohn's ridges (Fig. 1.2). The NKR including Eggvin Bank shows enriched incompatible elements and radiogenic isotopic compositions (e.g. *Haase et al.*, 2003; *Mertz et al.*, 2004; *Elkins et al.*, 2011, 2016). Also the area north of the WJMFZ has an isolated seamount and a large ridge (Logi Ridge). However, only the Vesteris Seamount has been dredged and dated, showing recent magmatism of non plume origin (*Haase and Devey*, 1994) (Fig. 1.2). A recent high-resolution mantle tomography model for the North Atlantic shows abnormally low S-wave velocities in the asthenosphere under the area, coinciding with the magmatic surface activity (*Rickers et al.*, 2013). Farther to the west, an island on the East Greenland coast (Traill Ø) is located landward of the WJMFZ and form the westernmost end of a large elongate magnetic high (Trail Ø Igneous Complex (TIC)). The landward end of the magnetic anomaly is tied to syenitic magmatism on the Traill Ø dated to 34-40 Ma (*Noble et al.*, 1988; *Price et al.*, 1997; *Larsen et al.*, 2014).

In terms of the origin and development of these postbreakup igneous areas, there are some challenging questions. Among these are:
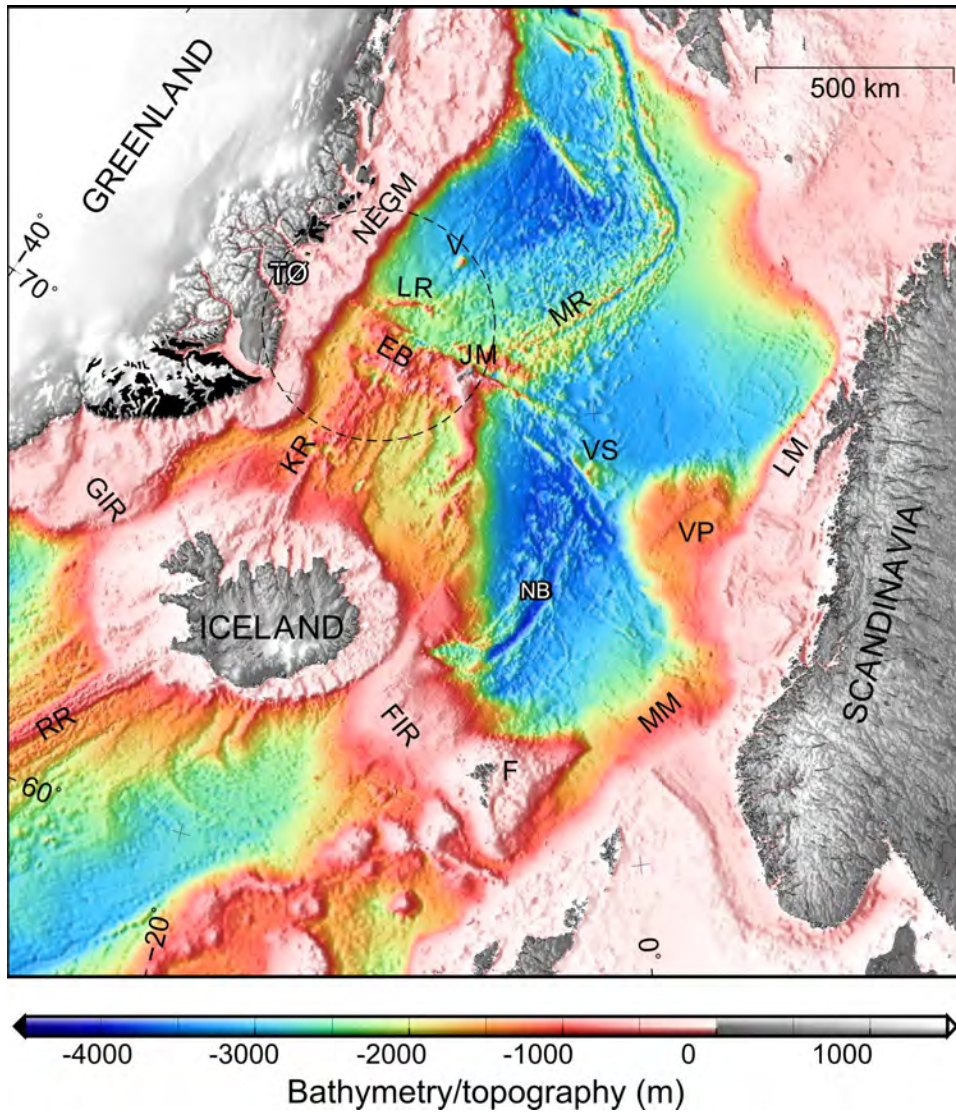
Figure 1.1: Bathymetry map (ETOPO2v2) (*National Geophysical Data Center*, 2006), where the study area is shown by the dashed circle. Black areas onshore Greenland indicate Early Cenozoic basalt flows or intrusions (*Noble et al.*, 1988). EB: Eggvin Bank, F: Faeroes, FIR: Faeroes-Iceland Ridge, GIR: Greenland-Iceland Ridge, JM: Jan Mayen, KR: Kolbeinsey Ridge, LM: Lofoten Margin, LR: Logi Ridge, MM: Møre Margin, MR: Mohn's Ridge, NB: Norway Basin, NEGM: Northeast Greenland Margin, RR: Reykjanes Ridge, TØ: Traill Ø, VP: Vøring Plateau, VS: Vøring Spur, and V: Vesteris Seamount.
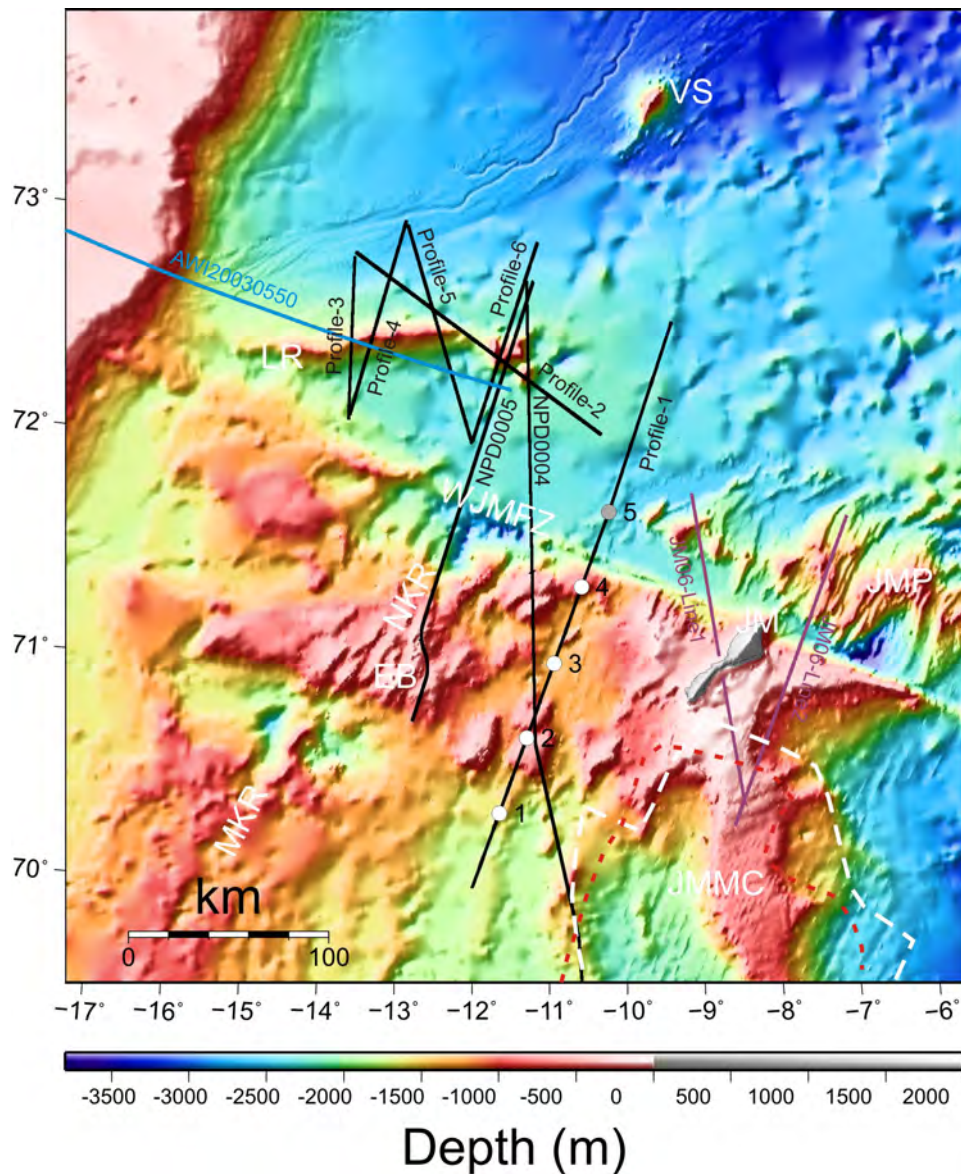
Figure 1.2: International Bathymetric Chart of the Arctic Ocean (IBCAO) (v.3) of the study area (*Jakobsson et al.*, 2012). Profile 1 is the OBS profile, where circles show OBS positions, and white fill indicates useful data. Profile 2-6, NPD0004, and NPD0005 are seismic reflection profiles across the WJMFZ and Logi Ridge. Several previous OBS based crustal studies are shown (Jan Mayen microcontinent (JM06-Line1,JM06-Line2) (*Kandilarov et al.*, 2012), Logi Ridge (AWI20030550) (*Voss and Jokat*, 2007). The white dashed line represents the location of the continental ocean boundary (COB) around the JMMC by *Breivik et al.* (2012a) incorporating results from *Kandilarov et al.* (2012), while the red dashed line shows the COB by *Peron-Pinvidic et al.* (2012a,b). EB: Eggvin Bank, JM: Jan Mayen, JMMC: Jan Mayen Mirocotinent, JMP: Jan Mayen Plateau, LR: Logi Ridge, MKR: Middle Kolbeinsey Ridge, NKR: Northern Kolbeinsey Ridge, WJMFZ: West Jan Mayen Fracture Zone, VS: Vesteris Seamount.

1. The Eggvin Bank is characterized by unusually shallow area, where the spreading axis almost reaches the sea surface. What is the crustal structure of the Eggvin Bank? The origin of the Eggvin Bank has been the subject of debate. Older publications have proposed quite different models for the formation of the Eggvin Bank: e.g., underlying continental crust extending from JMMC (*Campsie et al.*, 1990), a separate mantle plume under Jan Mayen (e.g. *Schilling*, 1999; *Elkins et al.*, 2016) or lateral flow of Iceland plume material (*Mertz et al.*, 2004).

2. Previous studies have suggested that magmatism near the WJMFZ may be related to different plate tectonic processes (e.g. *Gaina et al.*, 2017a; *Gernigon et al.*, 2009). Several studies proposed the shallow bathymetry north of the WJMFZ could be supported by hot asthenospheric flow (*Breivik et al.*, 2008; *Rickers et al.*, 2013; *Hoggard et al.*, 2017). Dynamic topography in the NE Atlantic is unevenly distributed, and transient by nature. Presently, the Logi Ridge is located above an unusually shallow seafloor. In order to constrain the mechanism behind the ridge formation, the timing of its development needs to be determined, and how that relates to the dynamic topography development.

3. Several studies suggest that strong lateral mantle flow, related to the Iceland Plume, extends at least as far north as the southern border of the Eggvin Bank (e.g. *Jones et al.*, 2002), but how the plume interacts with the lithosphere is debated (e.g. *Xue and Allen*, 2005; *Marquart et al.*, 2007; *Shorttle et al.*, 2010; *Koptev et al.*, 2017). Using the observed seismic anisotropy patterns beneath Iceland, *Xue and Allen* (2005) suggest that there is a ridge-channelled flow of material away from Iceland towards the southern end of the Kolbeinsey Ridge. Based on a regional tomography model and observed gravity field, *Marquart et al.* (2007) pointed out that the Kolbeinsey Ridge is dominated by a divergent flow, which is explained by a combination of plume and spreading flux along the ridge. A later examination of geophysical and geochemical data along the Kolbeinsey Ridge, on the other hand, motivated *Shorttle et al.* (2010) to suggest that the Iceland Plume spreads in a radial, pancake-like fashion. Recent high-resolution 3D thermo-mechanical numerical modeling suggests that flow of the plume material along the Kolbeinsey Ridge is constrained by pre-existing lithospheric structures related to the rifting of the Jan Mayen microcontinent off East Greenland (*Koptev et al.*, 2017). In this thesis, I also address a question whether the post-breakup igneous events (e.g. Eggvin Bank, Logi Ridge) in the NE Atlantic are affected by the plume flow.

In order to answer these questions, we have integrated seismic reflection and refraction profiles, mantle tomography results, bathymetry, and gravity data. The overall objectives are to: understand the magmatic development of the Jan Mayen-East Greenland area, NE

Atlantic; and related the findings to fundamental earth processes, especially associated with how the plume interacts with the oceanic lithosphere.

1.1 Geological setting

The part of the NE Atlantic surrounding our study area comprise two active spreading ridges (Mohn's Ridge and Kolbeinsey Ridge), one extinct mid-ocean ridge (Aegir Ridge), and one micro-continent (Jan Mayen Mirocontinent (JMMC)) (Fig. 1.1). In the eastern part, Mohn's Ridge and the Aegir Ridge were separated by the East Jan Mayen Fracture Zone (EJMFZ) in the Palogene, until spreading on the Aegir Ridge ceased in the Late Oligocene. To the west, the WJMFZ offsets the Kolbeinsey Ridge right-laterally by around 200 km, presently an active transform. The JMMC is located between the Aegir Ridge and the Kolbeinsey Ridge.

The NE Atlantic developed in two major tectonic events. Initial breakup between Greenland and Norway established three spreading axes in the Early Eocene (55-54 Ma); the Reykjanes Ridge in the south, the Aegir Ridge in the middle, and the Mohn's Ridge to the north (Fig. 1.3b). These margin segments were to various degrees influenced by the Iceland Plume resulting in volcanic margins (*Voss and Jokat*, 2007; *Breivik et al.*, 2009, 2014). During the Early Oligocene, the cessation of Labrador Sea spreading between Greenland and North America caused a major change in the relative plate motion between the Greenland and Eurasian plates, from NW-SE to E-W (*Gaina et al.*, 2009). Meanwhile, the average full spreading rate of Mohn's Ridge decreases from 40 mm/yr to 10 mm/yr from Early Eocene fo Early Oligocene (*Mosar et al.*, 2002) (Fig. 1.4). After that, the spreading on the Mohn's Ridge is symmetrical but moderately oblique at a full rate of 16 mm/yr, mostly producing a thin oceanic crust (4-5 km) (*Klingelhöfer et al.*, 2000a,b; *Gaina et al.*, 2017b; *Mosar et al.*, 2002).

The second major tectonic event is the rifting of the JMMC off the East Greenland margin south of the Mohn's Ridge. It occurred around 24-25 Ma due to establish the spreading axis jump from the Aegir Ridge to the Kolbeinsey Ridge (*Nunns*, 1982) (Fig. 1.3f). The spreading along the Kolbeinsey Ridge is slow (full rate: 16-18 mm/yr) and nearly orthogonal (*Appelgate*, 1997; *Mosar et al.*, 2002) (Fig. 1.4). The Kolbeinsey Ridge is divided into three different sections (southern, middle and northern part). Crustal thickness along the Southern Kolbeinsey Ridge (SKR) increases from 9.5 km to 12 km toward Iceland (*Hooft et al.*, 2006), while the Middle Kolbeinsey Ridge (MKR) and surrounding Iceland Plateau has a fairly homogeneous crustal thickness on average 9 km (*Hooft et al.*, 2006; *Kodaira*
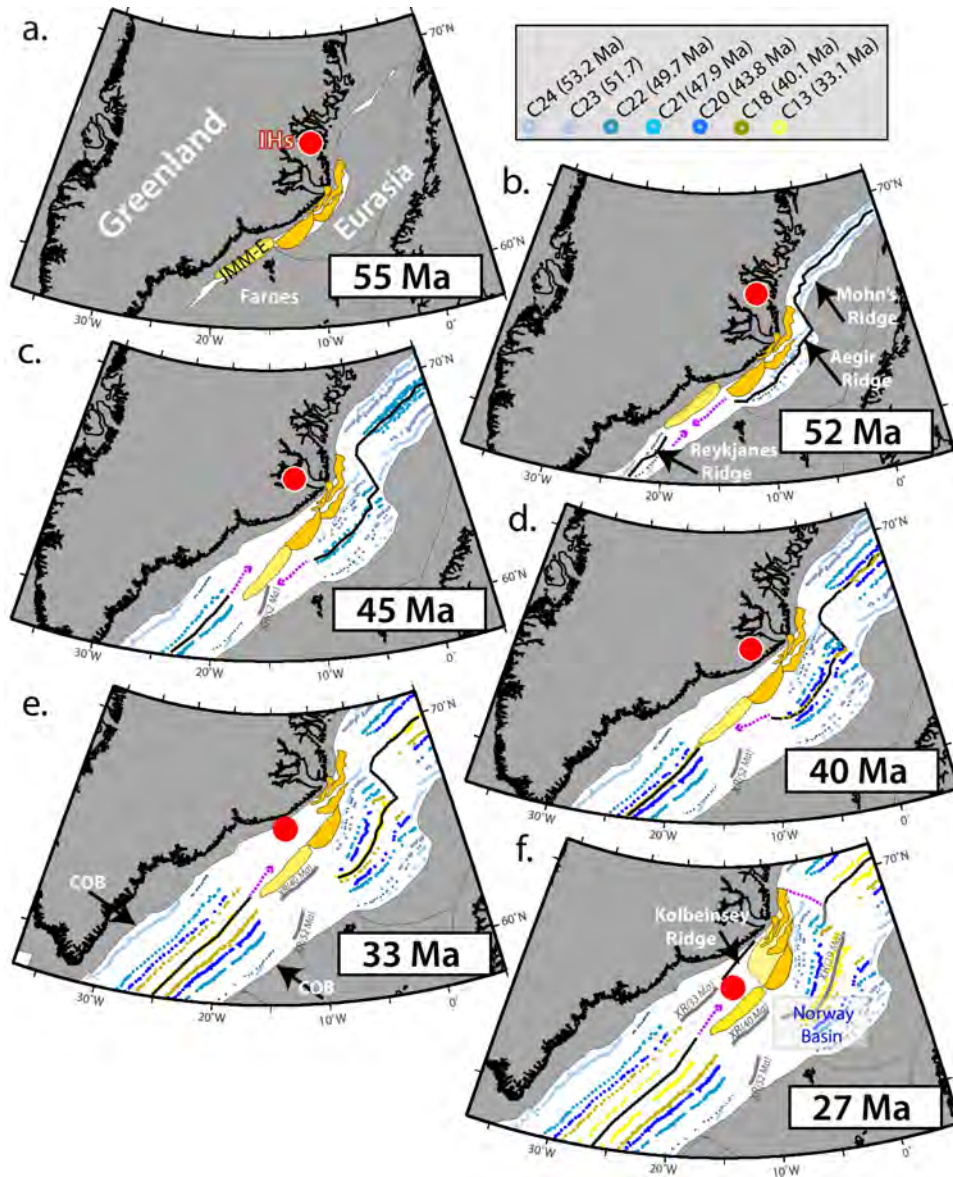
Figure 1.3: Evolution of NE Atlantic plate boundaries from pre-breakup (55 Ma) to 27 Ma, modified from *Torsvik et al.* (2015). Circles of different color mark the various magnetic anomalies. Main tectonic blocks of JMMC are shown in orange. Red circle infers Iceland Hotspot Location.
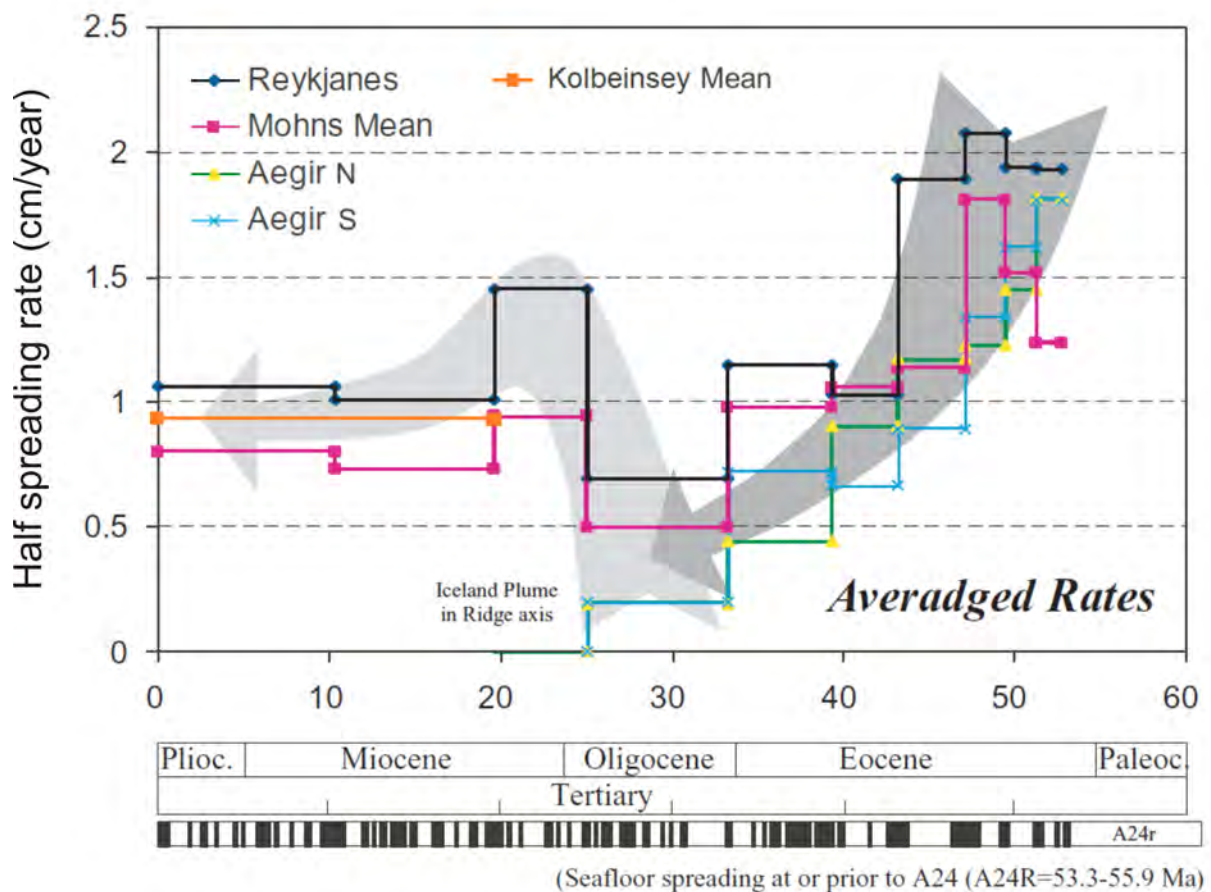
Figure 1.4: Half spreading rates, modified from *Mosar et al.* (2002), based on magnetic anomalies on the seafloor. Average half-spreading rates of Mohns and Kolbeinsey Ridge are indicated by magenta and orange solid lines. Reykjanes Ridge, which is located south of Iceland (Fig. 1.1), is represented by blue dots with black line. Northern and southern Aegir Ridge is shown by yellow/green and light blue profile respectively.

et al., 1997, 1998a). Thick crust along both the SKR and MKR is due to the thermal influence of the Iceland Plume with a homogeneous and depleted mantle source (*Elkins et al.*, 2011; *Hooft et al.*, 2006).

The JMMC has large crustal thickness variations. The maximum thickness is observed at the northern boundary of the JMMC (25 km), while the minimum could be as low as 3 km (*Kandilarov et al.*, 2012; *Kodaira et al.*, 1998a; *Breivik et al.*, 2012a). The eastern side of JMMC is a volcanic rifted margin (*Breivik et al.*, 2012b), while the western side is a non-volcanic rifted margin (*Kodaira et al.*, 1998b). The very thin Jan Mayen Basin crust (∼5 km) is created by a prolonged extensional phase prior to the Kolbeinsey Ridge formation (*Kodaira et al.*, 1998a; *Mjelde et al.*, 2008).

1.2 Data

In the early fall of 2011, a marine geophysical survey, including single-channel and wide-angle seismic study, was conducted between an Mayen and East Greenland, using the R/V Håkon Mosby. It is a collaboration between the Department of Geoscience, University of Oslo, Department of Earth Science, University of Bergen, and the Institute of Seismology and Volcanology, Hokkaido University, Sapporo, Japan. Onboard there were five Ocean Bottom Seismeters (OBSs), a digital ministreamer, and two different airgun arrays. The large array has four equal-sized Bolt air-guns with a total volume of 78.6 l used for the OBS work and fired every 200 m (Fig. 1.2). The smaller source is a tuned airgun array of 12.5 l, which was used for the reflection seismic surveying and fired every 50 m. Gravity was logged continuously, and a marine magnetometer was deployed during shooting.

The expedition resulted in six (approximately total 850 km length) good-quality single-channel seismic reflection lines and four wide-angle velocity data sets along a single profile. The ocean bottom seismometers (OBS) were deployed approximately N-S from the Greenland Basin across the Eggvin Bank (Fig. 1.2). Four OBSs returned good data sets, while OBS 5 in the north failed. Each OBS is composed of 4.5 Hz three-component geophones. The air-gun signals were recorded by a digital audio tape recorder with a 16 bit analog to digital converter sampling at 256 Hz. A single-channel streamer was also used to record near-vertical seismic reflection data, which was used to constrain sedimentary thickness for the starting velocity model. The OBS profile is presented in Paper 1, used to discuss the crustal structure and development of the Eggvin Bank.

In Paper 2, we present the six single-channel reflection seismic (SCS) and two multi-channel reflection seismic (MCS) by Norwegian Petroleum Directorate (NPD) (*Sandstå*

et al., 2012) collected the same year across the WJMFZ and the Logi Ridge (Fig. 1.2). The reflection profile was represented as two way travel time and seafloor ages along the profile are derived using the ages of *Gaina et al.* (2017b).

Paper 3 is not based on our own data, but compiles regional data sets. The crustal model was constructed based on the published seismic reflection and refraction lines in our study area (e.g. *Voss and Jokat*, 2007; *Breivik et al.*, 2012a; *Kodaira et al.*, 1997; *Hermann and Jokat*, 2016; *Kandilarov et al.*, 2012, 2015; *Weigel et al.*, 1995), crustal model of the Mohn's Ridge (*Klingelhöfer et al.*, 2000a), Moho depth of NE Atlantic only used in the NKR and nearby Eggvin Bank where refraction seimics are lacking (*Haase et al.*, 2016), sediment thickness of world's ocean and marginal seas (*Divins*, 2004) and CRUST 1.0 (*Laske et al.*, 2013). The mantle temperature and density model was derived from a V_{SH} mantle tomography model from 50 km to 250 km (*Rickers et al.*, 2013). The tomography model is based on non-linear full-waveform inversion techniques and measurements of the instantaneous phase misfit. Compared to the global S-wave model S20RTS (*Ritsema et al.*, 1999) and European full-waveform model (EU-TF) (*Fichtner and Trampert*, 2011), the V_{SH} model (NA-IP) (*Rickers et al.*, 2013) is characterized by a significantly improved resolution for both the upper and lower mantle; therefore, it images small-scale anomalies, such as spreading ridges and plume distribution under the NE Atlantic Region. The V_{SH} model comes with a horizontal grid spacing of 100 km and a depth-dependent vertical spacing of 10 km in the uppermost 350 km, 20 km between 350 and 700 km, and 50 km between 700 and 1300 km depth. The input gravity data is a recently published Arctic gravity field model (*Gaina et al.*, 2011). It has 10×10 km grid resolution and contains free-air gravity anomalies offshore and bouguer anomalies onshore (Jan Mayen Island) (*Gaina et al.*, 2011). Compared to other gravity field data (*Andersen et al.*, 2010; *Sandwell et al.*, 2014), this gravity field shows relatively longer wavelength of the gravity anomalies, which is expected to be sufficiently sensitive to density anomalies at larger depth.

1.3 Methods

For the first study, we use wide-angle seismic data recorded by three-component ocean bottom seismometers (OBS) across the Eggvin Bank. To facilitate the interpretation of the OBS recordings, the data were frequency filtered (5-12 Hz), a spiking deconvolution applied, together with amplitude scaling. The best information comes from the first arrivals, usually constraining velocity, while later arrivals often are reflections that can further constrain model geometry. First, the vertical component recording P-wave arrival

times are reduced by 8 km/s and picked as a function of distance, and the pick of the arriving phase is assigned an uncertainty usually equal to a typical cycle width of the phase (*Breivik et al.*, 2003). The misfit between the interpreted and modeled traveltimes within this uncertainty is estimated by using χ^2 analysis, where a value of 1 or lower per phase represents a fit (*Zelt and Smith*, 1992), and can be used to estimate uncertainty within the model. We use Rayinvr forward/inverse ray tracing software (*Zelt and Ellis*, 1988; *Zelt and Smith*, 1992) to build the 2D velocity modeling along the Profile-1 (Fig. 1.2). Similarly, S-wave arrivals from the horizontal components are reduced by 4.6 km/s and interpreted and modeled, giving the Vp/Vs ratio of different parts of the crust, which can constrain large lithology contrasts, if present. We use the correlation between seismic velocity and crustal thickness (H-V$_p$ analysis) (e.g. *Holbrook et al.*, 2001) to estimate the connection between the seismic properties and underlying mantle melting processes.

For the second study, we use reflection seismic data, recorded as two-way travel times. During seismic interpretation, the goal is to map out how mass transport from the Logi Ridge interacts with the regional sedimentation. Sedimentation and subsidence rates are determined from the interpretation by converting the time section to depth. For depth conversion we used a regional empirical velocity-depth trend for the sedimentary package (Vp= 1.8 + 0.7Z km/s, Z: depth in km) based on nearby seismic refraction studies (*Kandilarov et al.*, 2012; *Voss and Jokat*, 2007) (Fig. 1.2). Parts of the Logi Ridge have flat tops, indicating that it has been eroded at the sea surface. By assuming only age-dependent thermal subsidence of the oceanic crust, we can estimate the subsidence history to the time when the ridge was last sub-aerially exposed (e.g. *Caplan-Auerbach et al.*, 2000). Two somewhat different methods that both assume that erosion of the ridge stops after it has subsided below sealevel, can be applied: The ridge height records the oceanic depth at the time of submergence (Eq. 1.1):

$$d_i + 0.30\sqrt{t_s - t} = H_g; t = t_s - (\frac{H_g - d_i}{0.30})^2 \tag{1.1}$$

where d_i is the depth of the mid-oceanic ridge at 0 Ma, t_s is the age of the underlying crust, H_g is the height of the seamount, and the thermal subsidence rate is 0.30 km/Ma$^{1/2}$. While the present depth to the top records the amount of subsidence since the submergence (Eq. 1.2):

$$(\sqrt{t_s} - \sqrt{t_s - t})0.30 = D_g; t = t_s - (\sqrt{t_s} - \frac{D_g}{0.30})^2 \tag{1.2}$$

where D_g is the depth of the seamount top, and the other parameters as in Eq. 1.1. Both require correction of the regional sedimentation load at different times. The effect

of sediment loading has been removed using local Airy isostatic correction (*Le Douaran and Parsons*, 1982):

$$B_s = B - \frac{(\rho_s - \rho_w)}{(\rho_a - \rho_w)} Z_s \qquad (1.3)$$

where B is the basement depth, B_s is the basement depth corrected for sediment loading, ρ_a is the density of asthenospheric mantle (3200 kg/m^3), ρ_w is the density of water (1030 kg/m^3), Z_s is the sediment thickness, and the average sediment density (ρ_s) is derived from empirical velocity-density relationships (*Ludwig et al.*, 1970) based on a regional seismic refraction study (*Voss and Jokat*, 2007).

The third study is based on 3D gravity modeling of the upper 250 km of the Asthenosphere/Lithosphere of the greater Jan Mayen-East Greenland region. Sedimentary and crustal structures were compiled from regional reflection and refraction seismic lines, jointly interpolated with Petrel (by Schlumberger 1998-2013) using the Minimum Tension Gridding to create a 3D model with a lateral grid size of 10×10 km. Based on the published interpretations, we divided the crustal and sedimentary cover into 10 different units with distinct density. We obtain the temperature and related density structures of the mantle between 50 and 250 km from a shear-wave velocity (Vs) tomography model (*Rickers et al.*, 2013). The Vs model has been rescaled by applying the Triangulation Method of software OpendTect (*Huck*, 2012) to create a regular grid with 10× 10 km horizontal and 10 km vertical dimension. The Vs to temperature conversion was performed using the empirical equation of *Priestley and McKenzie* (2006), while conversion of temperature to density followed the approach of *Bai et al.* (2014), which is based on both pressure and temperature. To assess the density configuration between the Moho and 50 km depth, which has the poorest constraints from observational data, we combine forward (IGMAS+ (e.g. *Schmidt et al.*, 2011))and inverse 3D gravity modeling (fatiando a terra (for Python 2.7; (*Uieda et al.*, 2013))). First, we calculate the gravity response of an initial 3D density model that includes the data-constrained densities of the sediments, crust and deeper mantle, while including a constant density of 3300 kg/m^3 for the shallowest unconstrained mantle (forward gravity modelling). As a result of this step, we obtain the difference between the observed and the modelled gravity anomalies, i.e. the residual of this initial 3D density model. In a second step, we use these residual gravity anomalies to invert for the density configuration of the shallowest mantle above 50 km depth (inverse gravity modelling). We tested the sensitivity of the gravity response of the entire model with regard to both density and layer thickness variations. To determine the resolution

of the 3D gravity inverse model, we imposed a checkerboard pattern with a dimension of 125 km×125 km, and a density perturbation of ±50 kg/m^3 in the uppermost mantle.

1.4 Summary of papers

In this study, we have integrated wide-angle seismic refraction data, seismic reflection data, mantle tomography results, and gravity data in order to understand the magmatic development of the Jan Mayen-East Greenland area, NE Atlantic.

1.4.1 Paper 1

The Eggvin Bank has igneous oceanic crust at our profile position, but shows large variations in thickness, from 8 km to 13 km, where a 2-5 km increase is associated with two 20-30 km wide segments under the main seamounts. Results from P wave traveltime modeling show oceanic crustal velocities, with a low-velocity upper crust (2.8 km/s to 4.8 km/s), a middle crust (5.5 km/s to 6.5 km/s), and a low-gradient, high-velocity lower crust (6.7 km/s to 7.35 km/s). These typical oceanic crustal velocities and relatively high crustal V_p/V_s-ratios (1.82-1.88) indicate a mafic composition and are inconsistent with continental crust extending from the JMMC to the Eggvin Bank. Correlation between lower crust seismic velocity (V_p) and crustal thickness (H) shows a positive H-V_p correlation in the northern Eggvin Bank, but an overall poor H-V_p correlation in the south. Based on this, we suggest that there could be some thermal Iceland plume influence (high degree of mantle melting) under the northern Eggvin Bank, while the elevated magmatism in the southern part of the Eggvin Bank may be mostly affected by an enriched mantle source. The latter is seen at the NKR spreading axis (e.g. *Haase et al.*, 2003; *Elkins et al.*, 2011, 2016), and appears to have been present for a large part of the Eggvin Bank development.

1.4.2 Paper 2

North of the WJMFZ, we have used reflection seismic data in order to constrain the Logi Ridge development. Three different basement characters are observed: rough basement represents abyssal hills typical for the Atlantic Ocean; smooth basement is the result of basalt flows overprinting early sediments; irregular basement was formed by basalt flows and possible intra-basement intrusions.

The sedimentary strata have two distinct sedimentary units. The lower unit consists of pelagic sedimentation with basalt and/or gravity-driven debris flows close to the Logi Ridge, recording different development stages of the ridge. The upper unit contains pelagic sedimentation only. The age of the unit boundary is Middle Miocene ($\sim$12 Ma), tied to an IODP drill site north of our study area (*Myhre et al.*, 1995). Contourite deposits, which are formed by the East Greenland deep-water current coming from the north, are identified in the upper unit along the northern flank of the Logi Ridge. A correlation between sediment thickness and oceanic age gives an average sedimentation rate for the lower unit of 3.8 cm/ky. Based on the estimated age of the boundary, the sedimentation rate of the upper unit is 5.8 cm/ky. The change in character between these units could be related to both the major climate and paleoceanographic changes during the final opening of the Fram Strait.

Both the western (LRW) and eastern (LRE) parts of the Logi Ridge have flat tops, indicating that these have been eroded at the sea surface. There is considerable mass transport off the ridge during its development. Building of the ridge appears to have taken place from the Oligocene and well into the Early Miocene. From then on, there are mostly erosion products coming off the ridge until the late Middle Miocene ($\sim$12 Ma). After that, the ridge was submerged, and significant erosion ceased. However, there are obvious signs of later igneous growth of the crust to the south and east of the main ridge, some of that apparently quite recent. By comparing the dating of ridge development from the sedimentary record with those from dating methods based on seamount height and current top seamount depth, we can estimate to what extent the dynamic topography has changed since the last submergence of the ridge. This suggests that the study area has experienced dynamic uplift in the range of 0.05-0.2 km since the Middle Miocene. This only accounts for a small part of the 0.65 km bathymetric asymmetry over the Mohn's Ridge (*Breivik et al.*, 2008), showing that most of the dynamic uplift occurred before the end of the ridge development in the Middle Miocene, suggesting a causative relationship. The timing of the Logi Ridge development coincides with the rifting of the JMMC off from East Greenland, and this has been tied to the migration of the Iceland plume to underneath the East coast of Greenland (*Mjelde et al.*, 2008). Most likely, the Logi Ridge development is also related to this event.

1.4.3 Paper 3

A three-dimensional structural and density model of the crust and upper mantle over the greater Jan Mayen-East Greenland region is obtained from a combination of seismic

refraction/reflection lines, a V_s mantle tomography model, and forward and inverse 3D gravity modeling. The structure above the Moho and below 50 km is determined by observational data. The least constrained part is the uppermost mantle comprising mostly the lithosphere, between the Moho and 50 km, and we used inverse 3D gravity modeling to derive the density configuration of this part. For most of the area, the shallow mantle low-density trend (< 50 km depth) shows good correlation with the V_s constrained mantle density trends between 50 and 90 km; and with basement depth corrected for sediment loading. Beneath the southernmost part of the Middle Kolbeinsey Ridge (MKR) region, the low-density mantle anomaly coincides with the spreading axis, but it is increasingly deviating eastwards of it to the north. It crosses the WJMFZ and becomes weaker approaching the Mohn's spreading ridge. We interpret this as the result of thermal erosion of the lithosphere by hot asthenospheric flow out from the Iceland Plume. The deviation of the flow may be due to the lithospheric thickness increase north of the northern termination of the Kolbeinsey Ridge against the WJMFZ. Farther to the east, this thickness difference over the fracture zone is reduced, and eventually the lithosphere is thinnest to the north close to the Mohn's Ridge. The Jan Mayen magmatism as well as the predominance of seamounts on the eastern side of the Eggvin Bank, correlates well with this zone. Several eastwards axis jumps of the MKR during the last 5.5 Ma may also be caused by this thermal erosion. Therefore, the uppermost asthenospheric flow appears to be sensitive to the bottom lithospheric topography, but at a more regional scale instead of a local scale.

1.4.4 Conclusion remarks

This thesis is the first broad and systematic study of the magmatic development of the Jan Mayen-East Greenland area, NE Atlantic. In summary, the three works show a complex magmatic development of the area. The strongest plume influence is in the south part of our study area, where a hot and depleted asthenosphere is affecting MKR seafloor spreading. In the south, the hot asthenosphere lies underneath the spreading ridge, while the hot anomaly increasingly deviates to the east of the spreading ridge northwards. However, the Eggvin Bank appears to be mostly isolated from this hot asthenosphere, though eastern parts may have seen episodic influence from the Iceland plume in the past. Jan Mayen magmatism is deep and of low degree melting (*Trønnes et al.*, 1999), but could be the result of heating of the lithosphere from below, tied to the hot asthenospheric flow we have mapped out. Across the WJMFZ, the adjacent Jan Mayen Plateau surrounding the southern tip of the Mohn's Ridge has an unusually thick

oceanic crust (*Kandilarov et al.*, 2012), correlating well with the hot asthenospheric flow. In addition, our study suggests that it is unlikely that development of the igneous Logi Ridge is tied to this shallow asthenospheric flow. Instead, the formation of the Logi Ridge is associated with the development of the dynamic topography from the Oligocene to the Early Miocene, which could be tied to the migration of the Iceland plume to underneath the East Greenland coast, weakening the lithosphere there (*Mjelde et al.*, 2008). Possibly, both the Eggvin Bank and the Logi Ridge could have a deeper source with an enriched and heterogeneous mantle entrained at the outer part of the Iceland plume.

1.5 Outlook

The three studies included in the thesis apply different methods at quite different scales. We have tried to compare some of these through 2D gravity modeling of the crustal velocity model from the OBS study. Here we make use of the ship track gravity, which has higher resolution than satellite-derived gravity. The thermal structure of oceanic lithosphere is primarily controlled by its cooling history. Forward gravity models in such a setting must include the whole lithosphere to obtain realistic results. In the 3D gravity modeling study, we have used inverse modeling to find the average density structure of the lithosphere. We can compare this approach with that of using a forward 2D finite element temperature modeling algorithm for the spatial domain to simulate the temperature development based on the oceanic age along the transect (*Lee et al.*, 1980). See *Breivik et al.* (1999) for a description of parameters and procedure. Lithospheric mantle density is then derived in the same manner as in paper 3, using the approach of *Bai et al.* (2014). In order to avoid edge effects during the gravity modeling, we have extended the density at the ends of the transect by 1000 km.

Along Profile 1, we test the 2D gravity response of the model with regard to different crustal and mantle density models. In Figure 1.5, an initial crustal density model was built based on the crustal velocity model, and densities are derived from Rayinvr using its internal conversion (*Zelt and Smith*, 1992). Mantle density is based on the oceanic age development along the profile. Track gravity data is used here, which gives higher resolution than satellite-derived gravity (Fig. 1.5). The model crosses the WJMFZ, where there is a marked mantle density contrast over the fracture zone. This approach results in a good fit between the calculated and observed gravity (Fig. 1.5). Then we test the gravity response with the mantle density from Figure 1.5, and the crustal density model derived from inverse 3D density model (Paper 3) (Fig. 1.6). The crustal density model contains

four different layers with distinct density, and shows a much simpler density structure compared to the crustal density model from Figure 1.5. This approach results in a good fit between the calculated and observed gravity at large wavelength. Local gravity misfits are mainly due to the simpler crustal density structure used. Similarly, we test the gravity response using the high-resolution crustal model from Figure 1.5, and the mantle density derived from the 3D gravity model (Paper 3) down to 250 km. It has a reasonable fit in the northern part of the profile (Fig. 1.7). However, in the southern part, the calculated gravity is lower than the ship-track gravity, and the gravity misfit (up to 30 mGal) is increasing southwards (Fig. 1.7). Most likely, this is tied to mass variations outside of the profile. In order to test that, we compare the results of the true 3D model with the 2D forward gravity model using the same crustal and mantle density structure derived from the 3D density modeling in Paper 3 (Fig. 1.8). Both approaches show similar results in the north, but the 2D forward model gives ∼20 mGal lower gravity along the southern part, proving the 3D effect in the southern part of the profile. A minor contribution to the misfit, is due to the satellite gravity being somewhat lower than the ship track gravity in the southern part.

The results of forward and inverse modeling of the uppermost mantle along the test profile are similar, even if the longest wavelengths, which are related to asthenospheric structure, may not be adequately controlled in the 2D forward model. However, we also have to understand the difference in resolution and the limitations the different methods have. For the 2D forward model, only a complex crustal density structure can be used to reproduce the ship track gravity data in detail. This indicates ship track gravity data can be used to constrain the crustal model, while satellite derived gravity could not. On the other hand, there is a benefit to 3D gravity modeling if density varies a lot over a short distance outside of the profile. For the 3D gravity modeling, we only have satellite derived gravity available, and the 3D density structure has similar resolution as the satellite derived gravity, and should be valid at a regional scale. These tests also show that even if the forward thermal model gives a variable density depth distribution in the mantle above 50 km, the 3D averaging of density into homogeneous, narrow columns for the same part appears to be a good approximation when it comes to gravity response.
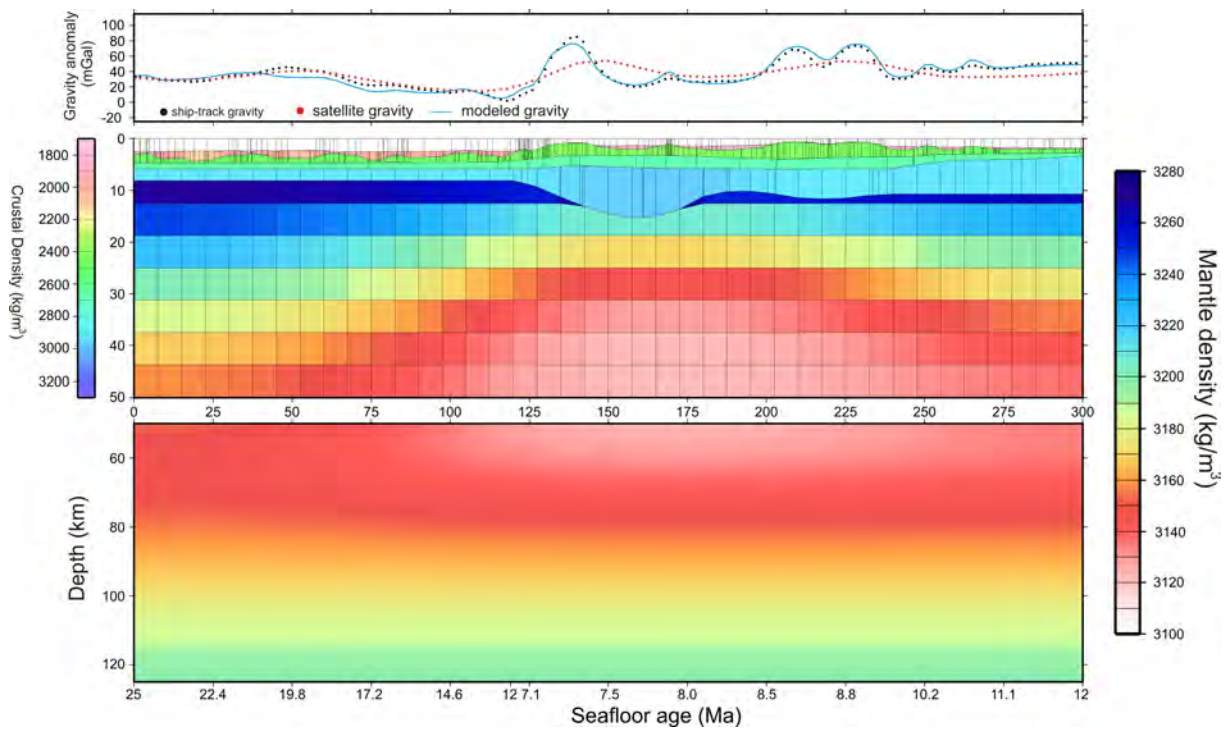
Figure 1.5: Results of 2D forward gravity along Profile 1. The mantle density is down to 125 km of the forward modeling based on the temporal development of the oceanic lithosphere along profile. The oceanic seafloor ages are indicated at the bottom of the figure. High resolution ship track-data is compared to satellite-derived gravity (*Gaina et al.*, 2011). The crustal density model of the forward modeling is derived from the OBS modeling, showing a complex crustal density structure. This approach results in a good fit between the calculated and observed gravity of both fine structure and regional level without any adjustments.
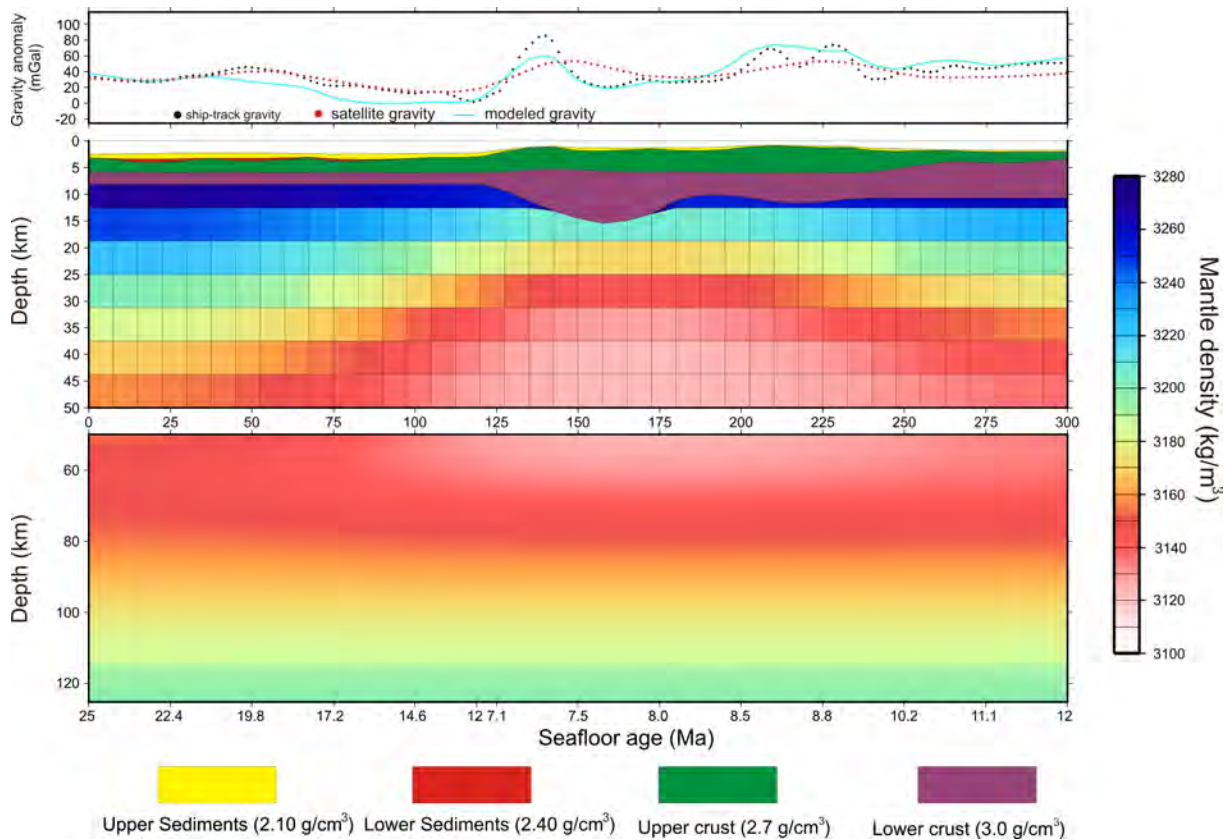
Figure 1.6: Results of 2D forward gravity along Profile 1. The mantle density configuration is the same as Figure 1.5, while the crustal density model is derived from the 3D inverse density model (Paper 3), consisting of four different layers. This approach results in a good fit between the calculated and observed gravity at large wavelength, but does not reproduce fine detail.
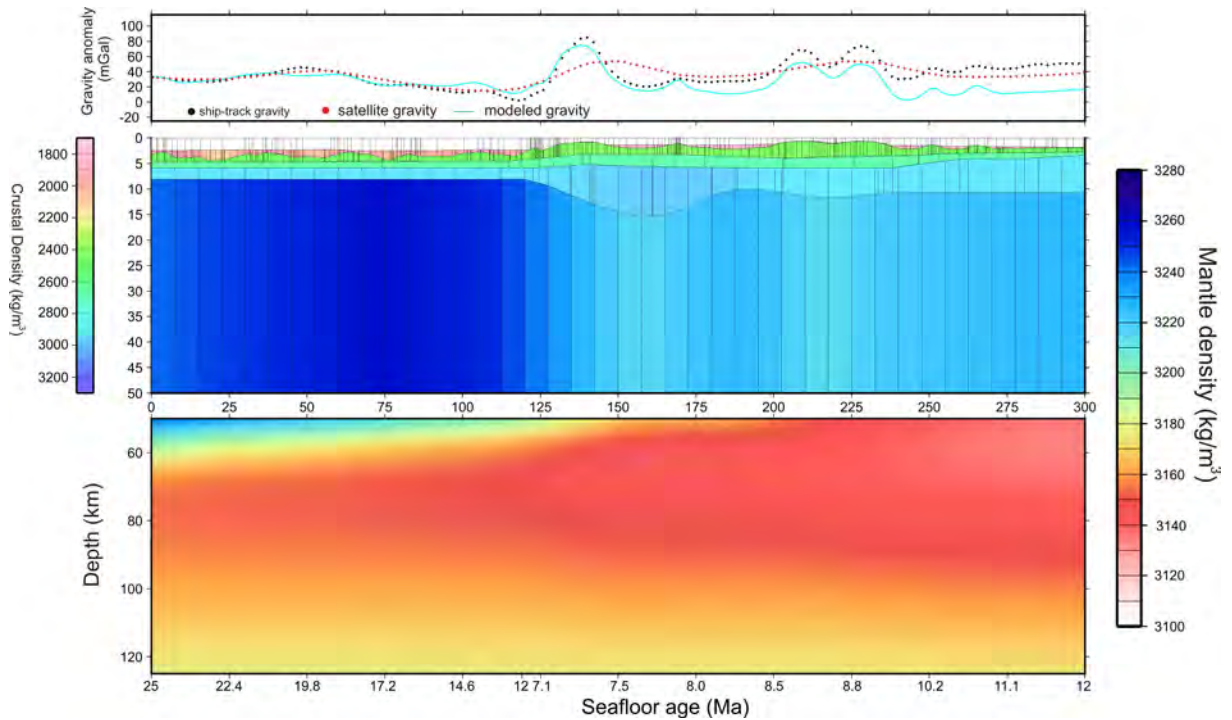
Figure 1.7: Results of 2D forward gravity along Profile 1. The mantle density is derived from the 3D gravity model (Paper 3) down to 250 km. The upper 125 km is shown here, where most of the lateral density contrasts occur (Fig. 4.3b in Paper 3). It has a reasonable fit in the northern part of the profile, and handles the mantle transition over the WJMFZ well. However, in the southern part the misfit between the observed and calculated gravity is increasing southwards.
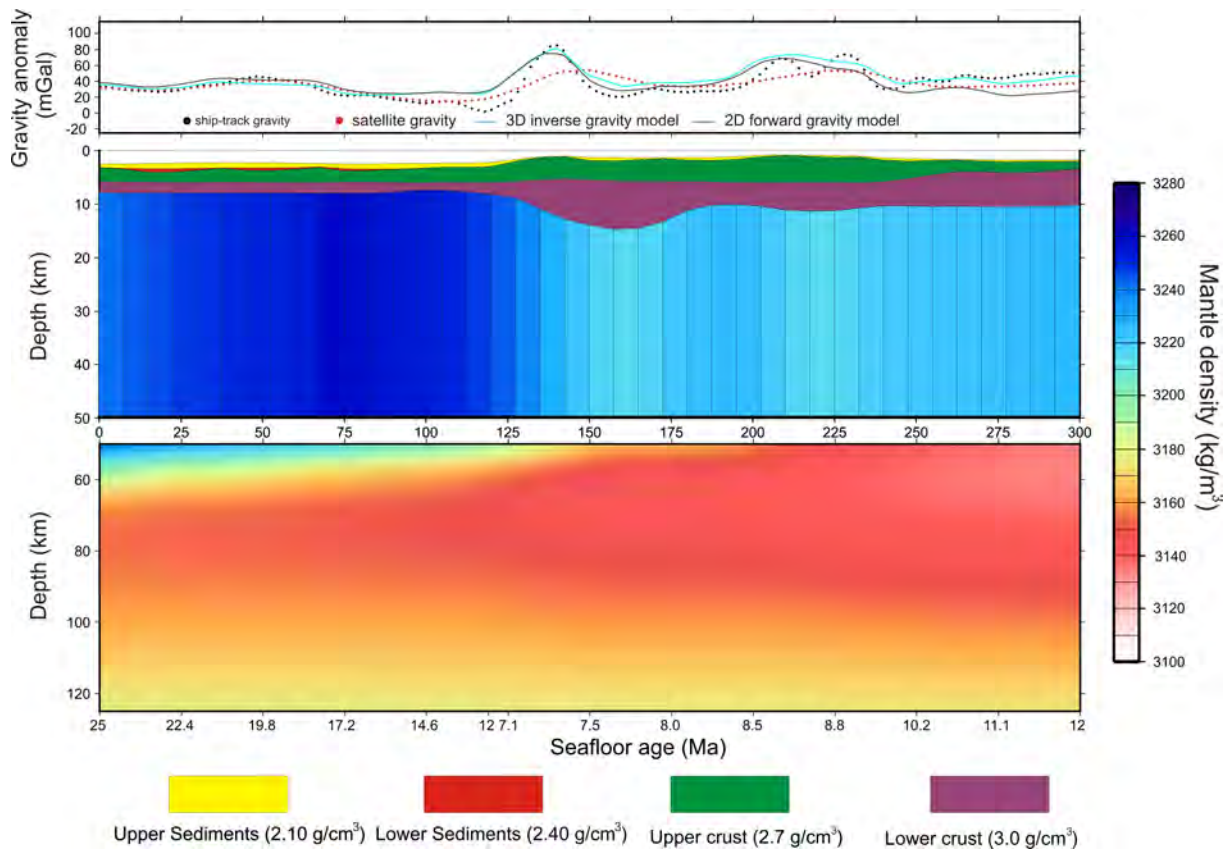
Figure 1.8: Results of 3D inverse gravity modeling (Paper 3) extracted along Profile 1. The mantle density is down to 250 km, shown to 125 km. Using the same crustal and mantle density model, we also shows the result of 2D forward gravity along the profile. Compared to 3D inverse model, the 2D forward model shows similar results along the northern and middle parts of the profile, but is ∼20 mGal lower along the southern part.

References

Abdelmalak, M. M., S. Planke, J. I. Faleide, D. A. Jerram, D. Zastrozhnov, S. Eide, and R. Myklebust (2016), The development of volcanic sequences at rifted margins: New insights from the structure and morphology of the Vøring Escarpment, mid-Norwegian Margin, *J. Geophys. Res. Solid Earth*, *121*(7), 5212–5236.

Adam, C., and V. Vidal (2010), Mantle flow drives the subsidence of oceanic plates, *Science*, *328*(5974), 83–85.

Andersen, O. B., P. Knudsen, and P. Berry (2010), The DNSC08GRA global marine gravity field from double retracked satellite altimetry models, *J. Geodesy*, *84*(3), doi: DOI:10.1007/s00190-009-0355-9.

Antonow, M., P. M. Goldschmidt, and H. Erlenkeuser (1997), The climatesensitive Vesterisbanken area (central Greenland Sea): depositional environment and paleoceanography during the past 250,000 years, *Crzybowski Foundation Spe. Publ.*, pp. 101–118.

Appelgate, B. (1997), Modes of axial reorganization on a slow-spreading ridge: The structural evolution of Kolbeinsey Ridge since 10 Ma, *Geology*, *25*, 431–434.

Bai, Y., S. E. Williams, R. D. Müller, Z. Liu, and M. Hosseinpour (2014), Mapping crustal thickness using marine gravity data: Methods and uncertainties, *Geophysics*, *79*(2), G27–G36.

Barron, E. J., and J. M. Whitman (1981), Ocean sediments in space and time, in *The Oceanic Lithosphere*, vol. 39, edited by C. Emiliani, pp. 689–731, Wiley, New York.

Barton, P. J. (1986), The relationship between seismic velocity and density in the continental crust – A useful constraint ?, *Geophys. J. R. Astron. Soc.*, *87*, 195–208.

Batiza, R. (2001), Seamounts and off-ridge volcanism, *Encyclopedia of Ocean Sciences. San Diego, Academic Press*, *5*, 2696–2708.

Berger, D., and W. Jokat (2008), A seismic study along the East Greenland margin from 72 N to 77 N, *Geophys. J. Int.*, *174*(2), 733–748.

Blischke, A., C. Gaina, J. R. Hopper, G. Péron-Pinvidic, B. Brandsdóttir, P. Guarnieri, O. Erlendsson, and K. Gunnarsson (2016), The Jan Mayen microcontinent: an update of its architecture, structural development and role during the transition from the Ægir Ridge to the mid-oceanic Kolbeinsey Ridge, *Geol. Soc. London Spec. Publ.*, *447*, SP447–5.

Bown, J. W., and R. S. White (1995), Effect of finite extension rate of melt generation at rifted continental marins, *J. Geophys. Res.*, *100*, 18,011–18,029.

Brandsdóttir, B., E. E. E. Hooft, R. Mjelde, and Y. Murai (2015), Origin and evolution of the Kolbeinsey Ridge and Iceland Plateau, N-Atlantic, *Geochem.Geophys.Geosyst.*, *16*, 612–634.

Breivik, A., R. Mjelde, J. I. Faleide, E. Flueh, and Y. Murai (2014), Magmatic development of the outer Vøring margin from seismic data, *J. Geophys. Res.*, *119*, 6733–6755, doi:10.1002/2014JB011040.

Breivik, A. J., J. Verhoef, and J. I. Faleide (1999), Effect of thermal contrasts on gravity modeling at passive margins: Results from the western Barents Sea, *J. Geophys. Res.*, *104*(B7), 15,293–15,311.

Breivik, A. J., R. Mjelde, P. Grogan, H. Shimamura, Y. Murai, and Y. Nishimura (2003), Crustal structure and transform margin development south of Svalbard based on ocean bottom seismometer data, *Tectonophysics*, *369*, 37–70.

Breivik, A. J., J. I. Faleide, and R. Mjelde (2008), Neogene magmatism northeast of the Aegir and Kolbeinsey Ridges, NE Atlantic: spreading ridge – mantle plume interaction?, *Geochem. Geophys. Geosyst.*, *9*(Q02004), doi:10.1029/2007GC001750.

Breivik, A. J., J. I. Faleide, R. Mjelde, and R. Flueh (2009), Magma productivity and early seafloor spreading rate correlation on the northern Vøring Margin, Norway – Constraints on mantle melting, *Tectonophysics*, *468*, 206–223, doi:10.1016/j.tecto.2008.09.020.

Breivik, A. J., R. Mjelde, J. I. Faleide, and Y. Murai (2012a), The eastern Jan Mayen microcontinent volcanic margin, *Geophys. J. Int.*, *188*, 798–818, doi:10.1111/j.1365-246X.2011.05307.x.

Breivik, A. J., R. Mjelde, A. K. Rai, and A. Frassetto (2012b), Geophyical survey of the Eggvin Bank and Logi Ridge-Greenland Sea, *Eos Trans. AGU*, *93*(52), Fall Meet. Suppl., Abstract T31B-2598.

Cammarano, F., and M. Guerri (2017), Global thermal models of the lithosphere, *Geophys. J. Int.*, *210*(1), 56–72.

Campsie, J., M. H. Rasmussen, L. C. Kovacs, F. Dittmer, J. C. Bailey, N. O. Hansen, and L. Johnson (1990), Chronology and evolution of the northern Iceland Plateau, *Polar Research*, *8*(2), 237–243.

Canales, J. P., J. J. Danobeitia, and A. B. Watts (2000), Wide-angle seismic constraints on the internal structure of Tenerife, Canary Islands, *J. Volcanol. Geotherm. Res.*, *103*, 65–81.

References

Cannat, M. (1996), How thick is the magmatic crust at slow spreading oceanic ridges ?, *J. Geophys. Res.*, *101*, 2847–2857.

Caplan-Auerbach, J., F. Duennebier, and G. Ito (2000), Origin of intraplate volcanoes from guyot heights and oceanic paleodepth, *J. Geophys. Res. Solid Earth*, *105*(B2), 2679–2697.

Caress, D. W., M. K. McNutt, R. S. Detrick, and J. Mutter (1995), Seismic imaging of hotspot-related crustal underplating beneath the Marquesas Islands, *Nature*, *373*, 600–603.

Charvis, P., A. Laesanpure, J. Gallart, A. Hirn, J. C. Lepine, B. de Voogd, Y. Hello, B. Pontoise, and T. A. Minshull (1999), Spatial distribution of hot spot material added to the lithosphere under La Reunion, from wide-angle seismic data, *J. Geophys. Res.*, *104*, 2875–2893.

Christensen, N. I. (1996), Poisson's ratio and crustal seismology, *J. Geophys. Res.*, *101*(B2), 3139–3156.

Christeson, G., G. Purdy, and G. Fryer (1994), Seismic constrains on shallow crustal emplacement processes at the fast spreading East Pacific Rise, *J. Geophys. Res.*, *99*, 17,957–17,974.

Davies, R., J. Cartwright, J. Pike, and C. Line (2001), Early Oligocene initiation of North Atlantic deep water formation, *Nature*, *410*(6831), 917–920.

Debaille, V., R. G. Trønnes, A. D. Brandon, T. E. Waight, D. W. Graham, and C. A. Lee (2009), Primitive off-rift basalts from Iceland and Jan Mayen: Os-isotopic evidence for a mantle source containing enriched subcontinental lithosphere, *Geochim. Cosmochim. Acta.*, *73*, 3423–3449.

Detrick, R., J. Collins, R. Stephen, and S. Swift (1994), In situ evidence for the nature of the seismic layer 2/3 boundary in oceanic crust, *Nature*, *370*, 288–290.

Dilek, Y. (1998), Structure and tectonics of intermediate-spread oceanic crust drilled at DSDP/ODP holes 504B and 896A, Costa Rica Rift, in Geolocial Evolution of Ocean Basin: Results From the Ocean Drilling Program, edited by A. Cramp et al., *Geol. Soc. Spec. Publ.*, *131*, 179–197.

Divins, D. L. (2004), Total sediment thickness of the world's oceans and marginal seas, World Data Cent. for Mar. Geol. and Geophys., Natl. Geophys. Data Cent., Boulder, Colo.

Doin, M. P., and L. Fleitout (1996), Thermal evolution of the oceanic lithosphere: an alternative view, *Earth Planet. Sci. Lett*, *142*(1-2), 121–136.

Eiken, O., and K. Hinz (1993), Contourites in the Fram Strait, *Sediment. Geol.*, *82*(1-4), 15–32.

Eldholm, O., and K. Grue (1994), North Atlantic volcanic margins: Dimensions and production rates, *J. Geophys. Res.*, *99*(B2), 2955–2968.

Elkins, L. J., K. W. W. Sims, J. Prytulak, T. Elliott, N. Mattielli, J. Blichert-Toft, J. Blusztajn, N. Dunbar, C. Devey, D. F. Mertz, J. G. Schilling, and M. Murrell (2011), Understanding melt generation beneath the slow-spreading Kolbeinsey Ridge using ^{238}U, ^{230}Th, and ^{231}Pa excesses, *Geochim. Cosmochim. Acta.*, *75*, 6300–6329.

Elkins, L. J., E. R. Rivers, K. W. W. Sims, J. Blichert-Toft, C. Devey, R. Chernow, R. Davis, and K. Meisenhelder (2013), Origins of anomalous ridge magmatism near Jan Mayen, *Mineral Mag.*, *77*(5), 1035.

Elkins, L. J., C. Hamelin, J. Blichert-Toft, S. R. Scott, K. W. W. Sims, I. A. Yeo, C. W. Devey, and R. B. Pedersen (2016), North Atlantic hotspot-ridge interaction near Jan Mayen Island, *Geochem. Persp. Lett.*, *2*, 55–67.

Engen, Ø., J. I. Faleide, and T. Karlberg Dyreng (2008), Opening of the Fram Strait gateway: A review of plate tectonic constraints, *Tectonophysics*, *450*, 51–69, doi:10.1016/j.tecto.2008.01.002.

Escartin, J., D. K. Smith, J. Cann, H. Schouten, C. H. Langmuir, and S. Escrig (2008), Central role of detachment faults in accretion of slow-spreading oceanic lithosphere, *Nature*, *455*, 790–294, doi:10.1038/nature07333.

Evans, J. R., and I. S. Sacks (1979), Deep structure of the Iceland Plateau, *J. Geophys. Res.*, *84*, 6859–6866.

Fichtner, A., and J. Trampert (2011), Resolution analysis in full waveform inversion, *Geophys. J. Int.*, *187*(3), 1604–1624.

Forsyth, D. W., N. Harmon, D. S. Scheirer, and R. A. Duncan (2006), Distribution of recent volcanism and the morphology of seamounts and ridges in the GLIMPSE study area: Implications for the lithospheric cracking hypothesis for the origin of intraplate, non–hot spot volcanic chains, *J. Geophys. Res. Solid Earth*, *111*(B11).

Fujie, G., S. Kodaira, M. Yamashita, T. Sato, and N. Takahashi, T.and Takahashi (2013), Systematic changes in the incoming plate structure at the Kuril trench, *Geophys. Res. Lett.*, *40*(1), 88–93.

Funck, T., W. H. Geissler, G. S. Kimbell, S. Gradmann, M. K. Erlendsson, Ö, and U. K. Petersen (2016), Moho and basement depth in the NE Atlantic Ocean based on seismic refraction data and receiver functions, *Geol. Soc. Spec. Pub.*, *477*, doi:10.1144/SP447.1.

Furmall, A. V. (2010), Melt production and ridge geometry over the past 10 Myr on the southern Kolbeinsey Ridge, Iceland, Master's thesis, University of Oregon, USA.

References

Gaina, C., L. Gernigon, and P. Ball (2009), Palaeocene–Recent plate boundaries in the NE Atlantic and the formation of the Jan Mayen microcontinent, *J. Geol. Soc.*, *166*, 601–616, doi:10.1144/0016-76492008-112.

Gaina, C., S. C. Werner, R. Saltus, S. Maus, and T. C.-G. GROUP (2011), Circum-Arctic mapping project: new magnetic and gravity anomaly maps of the Arctic., *J. Geol. Soc.*, *35*, 39–48.

Gaina, C., A. Nasuti, G. S. Kimbell, and A. Blischke (2017a), Break-up and seafloor spreading domains in the NE Atlantic, *Geol. Soc. London Spec. Publ.*, *447*, SP447–12.

Gaina, C., A. Blischke, W. H. Geissler, G. S. Kimbell, and Ö. Erlendsson (2017b), Seamounts and oceanic igneous features in the NE Atlantic: a link between plate motions and mantle dynamics, *Geol. Soc. London Spec. Publ.*, *447*(1), 419–442.

Geissler, W. H., C. Gaina, J. R. Hopper, T. Funck, A. Blischke, U. Arting, J. á Horni, G. Péron-Pinvidic, and M. M. Abdelmalak (2017), Seismic volcanostratigraphy of the NE Greenland continental margin, *Geol. Soc. London Spec. Publ.*, *447*(1), 149–170.

Gernigon, L., O. Olesen, J. Ebbing, S. Wienecke, C. Gaina, J. Mogaard, M. Sand, and R. Myklebust (2008), Geophyical insights and early spreading history in the vicinity of the Jan Mayen Fracture Zone, Norwegian-Greenland sea, *Tectonophysics*, *468*, 185–205.

Gernigon, L., O. Olesen, J. Ebbing, S. Wienecke, C. Gaina, J. O. Mogaard, M. Sand, and R. Myklebust (2009), Geophysical insights and early spreading history in the vicinity of the Jan Mayen Fracture Zone, Norwegian–Greenland Sea, *Tectonophysics*, *468*, 185–205, doi:10.1016/j.tecto.2008.04.025.

Goes, S., and S. Van der Lee (2002), Thermal structure of the north American uppermost mantle inferred from seismic tomography, *J.Geophys.Res.*, *107*(B3).

Götze, H. J., and B. Lahmeyer (1988), Application of three-dimensional interactive modeling in gravity and magnetics, *Geophyics*, *53*, 1096–1108.

Grose, C. J., and J. C. Afonso (2013), Comprehensive plate models for the thermal evolution of oceanic lithosphere, *Geochem. Geophys. Geosyst.*, *14*(9), 3751–3778.

Haase, C., J. Ebbing, and T. Funck (2016), A 3D crustal model of the NE Atlantic based on seismic and gravity data, *Geol. Soc. Spec. Pub.*, *447*.

Haase, K. M., and C. W. Devey (1994), The petrology and geochemistry of Vesteris Seamount, Greenland Basin – an intraplate alkaline volcano of non-plume origin, *J. Petrol.*, *35*(2), 295–328.

Haase, K. M., C. W. Devey, and M. Wieneke (2003), Magmatic processes and mantle heterogeneity beneath the slow-spreading northern Kolbeinsey Ridge segment, North Atlantic, *Contrib. Mineral. Petrol.*, *144*, 428–448.

Hampel, A., N. Kukowski, J. Bialas, C. Huebscher, and R. Heinbockel (2004), Ridge subduction at an erosive margin-the collision zone of the Nazca Ridge in southern Peru, *J. Geophys. Res.*, *109*, B02,101, doi:10.1029/2003JB002593.

Havskov, J., and K. Atakan (1991), Seismicity and volcanism of Jan Mayen Island, *Terra Nova*, *3*(5), 517–526.

Hermann, T. (2013), The Northeast Greenland Margin-Tectonic Evolution, Ph.D. thesis, University of Jena.

Hermann, T., and W. Jokat (2016), Crustal structure off Kong Oscar Fjord, east Greenland: Evidence for focused melt supply along the Jan Mayen Fracture Zone, *Tectonophysics*, *691*, 110–119.

Hieronymus, C. F., and D. Bercovici (2000), Non-hotspot formation of volcanic chains: Control of tectonic and flexural stresses on magma transport, *Earth Planet. Sci. Lett.*, *181*(4), 539–554.

Hoggard, M. J., J. Winterbourne, K. Czarnota, and N. White (2017), Oceanic residual depth measurements, the plate cooling model, and global dynamic topography, *J. Geophys. Res. Solid Earth*, *122*(3), 2328–2372.

Holbrook, W. S., W. D. Mooney, and N. I. Christensen (1992), The seismic structure of the deep continental crust, in *Continental lower crust*, edited by D. M. Fountain, R. Arculus, and R. W. Kay, pp. 1–43, Elsevier, Amsterdam.

Holbrook, W. S., H. C. Larsen, J. Korenaga, T. Dahl-Jensen, I. D. Reid, P. B. Kelemen, J. R. Hopper, G. M. Kent, D. Lizarralde, S. Bernstein, and R. S. Detrick (2001), Mantle thermal structure and active upwelling during continental breakup in the North Atlantic, *Earth Planet. Sci. Lett.*, *190*, 251–266.

Hooft, E. E. E., R. S. Detrick, D. R. Toomey, J. A. Collins, and J. Lin (2000), Crustal thickness and structure along three contrasting spreading segments of the Mid-Atlantic Ridge, 33.5°-35°N, *J. Geophys. Res.*, *105*(B4), 8205–8226.

Hooft, E. E. E., B. Brandsdóttir, R. Mjelde, H. Shimamura, and Y. Murai (2006), Asymmetric plume ridge interaction around Iceland: The Kolbeinsey Ridge Iceland Seismic Experiment, *Geochem. Geophys. Geosyst.*, *7*(5), 1–26.

Howe, J. A., T. M. Shimmield, R. Harland, and N. Eyles (2008), Late Quaternary contourites and glaciomarine sedimentation in the Fram Strait, *Sedimentology*, *55*(1), 179–200.

Howell, S. M., G. Ito, A. J. Breivik, A. Rai, R. Mjelde, B. Hanan, K. Sayit, and P. Vogt (2014), The origin of the asymmetry in the Iceland hotspot along the Mid-Atlantic Ridge from continental breakup to present-day, *Earth Planet. Sci. Lett.*, *392*, 143–153.

References

Huck, H. (2012), The Road to Open Source: Sharing a Ten Years Experience in Building OpendTect, the Open Source Seismic Interpretation Software, in *74th EAGE Conference and Exhibition-Workshops.*

Hunter, S. E., D. Wilkinson, J. Stanford, D. A. V. Stow, S. Bacon, A. M. Akhmetzhanov, and N. H. Kenyon (2007), The Eirik Drift: a long-term barometer of North Atlantic deepwater flux south of Cape Farewell, Greenland, *Geol. Soc. London Spec. Publ.*, *276*(1), 245–263.

Imsland, P. (1986), The volcanic eruption on Jan Mayen, January 1985: Interaction between a volcanic island and a fracture zone, *J. Volcanol. Geoth. Res.*, *28*, 45–53.

Ito, G. (2001), Reykjanes 'V'-shaped ridges originating from a pulsing and dehydrating mantle plume, *Nature*, *411*, 681–684.

Ito, G. T., and J. Lin (1995), Mantle temperature anomalies along the past and paleoaxes of the Galápagos spreading center as inferred from gravity analyses, *J. Geophys. Res.*, *100*(B3), 3733–3745.

Jacobson, R. S. (1992), Impact of crustal evolution on changes of the seismic properties of the uppermost oceanic crust, *Rev. Geophys.*, *30*(1), 23–42.

Jakobsson, M., J. B., B. Rudels, J. Nycander, M. Frank, L. Mayer, W. Jokat, F. Sangiorgi, M. ORegan, H. Brinkhuis, et al. (2007), The early Miocene onset of a ventilated circulation regime in the Arctic Ocean, *Nature*, *447*(7147), 986–990.

Jakobsson, M., L. A. Mayer, B. Coakley, J. A. Dowdeswell, S. Forbes, B. Fridman, H. Hodnesdal, R. Noormets, R. Pedersen, M. Rebesco, H.-W. Schenke, Y. Zarayskaya, A. D. Accettella, A. Armstrong, R. M. Anderson, P. Bienhoff, A. Camerlenghi, I. Church, M. Edwards, J. V. Gardner, J. K. Hall, B. Hell, O. B. Hestvik, Y. Kristoffersen, C. Marcussen, R. Mohammad, D. Mosher, S. V. Nghiem, M. T. Pedrosa, P. G. Travaglini, and P. Weatherall (2012), International Bathymetric Chart of the Arctic Ocean (IBCAO) Version 3.0, *Geophys. Res. Lett.*, *39*(L12609), doi:10.1029/2012GL052219.

Jha, K., E. M. Parmentier, and J. P. Morgan (1994), The role of mantle-depletion and melt-retention buoyancy in spreading-center segmentation, *Earth. Planet. Sci. Lett.*, *125*(1-4), 221–234.

Jones, S. M., N. White, and J. Maclennan (2002), V-shaped ridges around Iceland: Implications for spatial and temporal patterns of mantle convection, *Geochem. Geophys. Geosyst.*, *3*(10), 1059, doi:10.1029/2002GC000361.

Kandilarov, A., R. Mjelde, R. B. Pedersen, B. Hellevang, C. Papenberg, C. J. Petersen, L. Planert, and E. Flueh (2012), The northern boundary of the Jan Mayen Microcontinent, North Atlantic determined from ocean bottom seismic, multichannel seismic, and gravity data, *Mar. Geophys. Res.*, *33*(1), 55–76.

Kandilarov, A., R. Mjelde, E. Flueh, and R. B. Pedersen (2015), V_p/V_s-ratios and anisotropy on the northern Jan Mayen Ridge, North Atlantic, determined from ocean bottom seismic data, *Polar Sci.*, *9*(3), 293–310.

Kelemen, P. B., and W. S. Holbrook (1995), Origin of thick, high-velocity, igneous crust along the U.S. East Coast Margin, *J. Geophys. Res.*, *100*(B7), 10,077–10,094.

Keller, R. A., M. R. Fisk, R. A. Duncan, and W. M. White (1997), 16 my of hotspot and nonhotspot volcanism on the Patton-Murray seamount platform, Gulf of Alaska, *Geology*, *25*(6), 511–514.

Klingelhöfer, F., L. Géli, and R. S. White (2000a), Geophysical and geochemical constraints on crustal accretion at the very-slow spreading Mohns Ridge, *Geophys. Res. Lett.*, *27*(10), 1547–1550.

Klingelhöfer, F., L. Géli, L. Matias, N. Steinsland, and J. Mohr (2000b), Crustal structure of a super-slow spreading centre: a seismic refraction study of Mohns Ridge, 72°N, *Geophys. J. Int.*, *141*, 509–526.

Kodaira, S., R. Mjelde, H. Shimamura, K. Gunnarsson, and H. Shiobara (1997), Crustal structure of the Kolbeinsey Ridge, N. Atlantic, obtained by use of Ocean Bottom Seismographs, *J. Geophys. Res.*, *102*(B2), 3131–3151.

Kodaira, S., R. Mjelde, K. Gunnarsson, H. Shiobara, and H. Shimamura (1998a), Structure of the Jan Mayen microcontinent and implication for its evolution, *Geophys. J. Int.*, *132*, 383–400.

Kodaira, S., R. Mjelde, K. Gunnarsson, H. Shiobara, and H. Shimamura (1998b), Evolution of oceanic crust on the Kolbeinsey Ridge, north of Iceland, over the past 22 Myr, *Terra Nova*, *10*, 27–31.

Koptev, A., S. Cloetingh, E. Burov, T. François, and T. Gerya (2017), Long-distance impact of Iceland plume on NorwayâĂŹs rifted margin, *Sci. Rep.*, *7*.

Korenaga, J. (2008), Urey ratio and the structure and evolution of Earth's mantle, *Rev. Geophys.*, *46*(2).

Korenaga, J., W. S. Holbrook, G. M. Kent, P. B. Kelemen, R. S. Detrick, H. C. Larsen, J. R. Hopper, and T. Dahl-Jensen (2000), Crustal structure of the southeast Greenland margin from joint refraction and reflection seismic tomography, *J. Geophys. Res.*, *105*, 21,591–21,614.

Korenaga, J., P. B. Kelemen, and W. S. Holbrook (2002), Methods for resolving the origin of large igneous provinces from crustal seismology, *J. Geophys. Res.*, *107*(B9), 2178, doi:10.1029/2001JB001030.

References

Kroll, H., A. Kirfel, R. Heinemann, and B. Barbier (2012), Volume thermal expansion and related thermophysical parameters in the Mg, Fe olivine solid-solution series, *Eur. J. Mineral.*, *24*(6), 935–956.

Laberg, J. S., and T. O. Vorren (2004), Weichselian and Holocene growth of the northern high-latitude Lofoten Contourite Drift on the continental slope of Norway, *Sediment. Geol.*, *164*(1), 1–17.

Laberg, J. S., M. S. Stoker, K. I. T. Dahlgren, H. de Haas, H. Haflidason, B. O. Hjelstuen, T. Nielsen, P. M. Shannon, T. O. Vorren, T. C. E. van Weering, and S. Ceramicola (2005), Cenozoic alongslope processes and sedimentation on the NW European Atlantic margin, *Mar. Petrol. Geol.*, *22*, 1069–1088.

Larsen, L. M., A. K. Pedersen, C. Tegner, and R. A. Duncan (2014), Eocene to Miocene igneous activity in NE Greenland: northward younging of magmatism along the East Greenland margin, *J. Geol. Soc, London.*, *171*(4), 539–553.

Laske, G., G. Masters, Z. Ma, and M. Pasyanos (2013), Update on CRUST 1.0- A 1-degree Global Model of Earth's Crust., *Geophys.Res.Abstracts*, *15*, abstract EGU2013-2658.

Le Douaran, S., and B. Parsons (1982), A note on the correction of ocean floor depths for sediment loading, *J. Geophys. Res. Solid Earth*, *87*(B6), 4715–4722.

Lee, T.-C., A. Rudman, and A. Sjoreen (1980), Application of finite element analysis to terrestrial heatflow, Dept. of Nat. Resour., Geol. Surv., Indiana, Bloomington.

Lizarralde, D., J. B. Gaherty, J. A. Collins, G. Hirth, and S. D. Kim (2004), Spreading-rate dependence of melt extraction at mid-ocean ridges from mantle seismic data, *Nature*, *432*, 744–747, doi:10.1038/nature03140.

Ljones, F., A. Kuwano, R. Mjelde, A. J. Breivik, H. Shimamura, Y. Murai, and Y. Nishimura (2004), Crustal transect from the North Atlantic Knipovich Ridge to the Svalbard margin west of Hornsund, *Tectonophyics*, *378*, 17–41.

Ludwig, W. I., J. E. Nafe, and C. L. Drake (1970), Seismic refraction, *The Sea*, *4*(1), 53–84.

Maercklin, N. (2007), Supolar and supofilt: Su programs for polarization analysis and filtering of three-component data., doi:10.13140/2.1.1697.7926.

Marquart, G., H. Schmeling, and O. Čadek (2007), Dynamic models for mantle flow and seismic anisotropy in the North Atlantic region and comparison with observations, *Geochem. Geophys. Geosyst.*, *8*(2).

Mattingsdal, R., J. Knies, K. Andreassen, K. Fabian, K. Husum, K. Grøsfjeld, and S. De Schepper (2014), A new 6 Myr stratigraphic framework for the Atlantic–Arctic Gateway, *Quat. Sci. Rev.*, *92*, 170–178.

Maus, S., T. Sazonova, K. Hemant, J. D. Fairhead, and D. Ravat (2007), National geophysical data center candidate for the world digital magnetic anomaly map, *Geochem. Geophys. Geosyst.*, *8*(6).

McKenzie, D., and M. J. Bickle (1988), The volume and composition of melt generated by extension of the lithosphere, *J. Petrol.*, *29*(3), 625–679.

Menke, W., M. West, B. Brandsdóttir, and B. Sparks (1998), Compressional and shear velocity structure of the lithosphere in northern Iceland, *Bull. Seismol. Soc. Am.*, *88*, 1561–1571.

Mertz, D. F., W. D. Sharp, and K. M. Haase (2004), Volcanism on the Eggvin Bank (Central Norwegian-Greenland Sea, latitude ∼71°N): age, source, and relationship to the Iceland and putative Jan Mayen plumes, *J. Geodyn.*, *38*, 57–83, doi:10.1016/j.jog.2004.03.003.

Mjelde, R., R. Aurvåg, S. Kodaira, H. Shimamura, K. Gunnarsson, A. Nakanishi, and H. Shiobara (2002), Vp/Vs-ratios from the central Kolbeinsey Ridge to the Jan Mayen Basin, North Atlantic; implications for lithology, porosity and present-day stress field, *Mar. Geophys. Res.*, *23*(2), 123–145.

Mjelde, R., T. Raum, P. Digranes, H. Shimamura, H. Shiobara, and S. Kodaira (2003), Vp/Vs-ratio along the Vøring margin, NE Atlantic, derived from OBS-data: implications on lithology and stress-field, *Tectonophysics*, *369*, 175–197.

Mjelde, R., I. Eckhoff, S. Solbakken, S. Kodaira, H. Shimamura, K. Gunnarsson, A. Nakanishi, and H. Shiobara (2007), Gravity and S-wave modeling across the Jan Mayen Ridge, North Atlantic; implications for crustal lithology and continental break-up processes, *Mar. Geophys. Res.*, *28*, 27–41, doi:10.1007/s11001-006-9012-3.

Mjelde, R., T. Raum, A. J. Breivik, and J. I. Faleide (2008a), Crustal transect across the North Atlantic, *Mar. Geophys. Res.*, *29*, 73–87, doi:10.1007/s11001-008-9046-9.

Mjelde, R., A. J. Breivik, T. Raum, E. Mittelstaedt, G. Ito, and J. I. Faleide (2008b), Magmatic and tectonic evolution of the North Atlantic, *J. Geol. Soc.*, *165*, 31–42, doi:10.1144/0016-76492007-018.

Morgan, W. (1983), Hotspot tracks and the early rifting of the Atlantic, *Tectonophysics*, *94*, 123–139.

Mosar, J., G. Lewis, and T. H. Torsvik (2002), North Atlantic sea-floor spreading rates: implications of the Tertiary development of inversion structures of the Norwegian-Greenland Sea, *J. Geol. Soc.*, *159*, 503–515.

Müller, R. D., M. Sdrolias, C. Gaina, and W. R. Roest (2008), Age, spreading rates, and spreading asymmetry of the world's ocean crust, *Geochem, Geophys. Geosyst.*, *9*(4).

References

Myhre, A. M., J. Thiede, J. V. Firth, N. Ahagon, K. S. Black, J. Bloemendal, G. W. Brass, J. F. Bristow, N. Chow, M. Cremer, L. Davis, B. Flower, T. Fronval, J. Hood, D. Hull, N. Koc, B. Larsen, W. Lyle, M, J. McManus, O. L. E. Oconnel, S., F. R. Rack, T. Sato, R. P. Scherer, D. Spiegler, R. Stein, M. Tadross, S. Wells, D. Williamson, B. White, and T. Wolf-Welling (1995), North Atlantic-Arctic Gateways I. Proceedings of the Ocean Drilling Program, Initial Reports 151., in *Proceedings of the Ocean Drilling Program, Scientific Results*, vol. 151, pp. 159–220.

Naif, S., K. Key, S. Constable, and R. L. Evans (2013), Melt-rich channel observed at the lithosphere-asthenosphere boundary, *Nature*, *495*, 356–359, doi:10.1038/nature11939.

Nam, S. I., and R. Stein (1999), Late Quaternary variations in sediment accumulation rates and their paleoenvironmental implications: A case study from the East Greenland continental margin, *GeoResearch Forum*, *5*, 223–240.

National Geophysical Data Center (2006), 2-minute gridded global relief data (ETOPO2) v2. National Geophysical Data Center, NOAA, doi:10.7289/V5J1012Q.

Noble, R. H., R. M. Macintyre, and P. E. Brown (1988), Age constraints on Atlantic evolution: timing of magmatic activity along the E Greenland continental margin, *Geol. Soc. Spec. Publ.*, *39*, 201–214, doi:10.1144/GSL.SP.1988.039.01.19.

Nunns, A. (1982), The structure and evolution of the Jan Mayen Ridge and surrounding regions, in *Studies in continental margin geology*, vol. 34, edited by J. S. Watkins and C. L. Drake, pp. 193–208, Am. Assoc. Petrol. Geol., Tulsa, Oklahoma, USA.

Olesen, O., J. Ebbing, E. Lundin, E. Mauring, J. R. Skilbrei, T. H. Torsvik, E. K. Hansen, T. Henningsen, P. Midbøe, and M. Sand (2007), An improved tectonic model for the Eocene opening of the Norwegian-Greenland Sea: Use of modern magnetic data, *Mar. Petrol. Geol.*, *24*, 53–66, doi:10.1016/j.marpetgeo.2006.10.008.

Olsson, K. A., E. Jeansson, T. Tanhua, and J. Gascard (2005), The East Greenland Current studied with CFCs and released sulphur hexafluoride, *J. Marine. Syst.*, *55*(1-2), 77–95.

Oxburgh, E. M., E. R.and Parmentier (1977), Compositional and density stratification in oceanic lithosphere-causes and consequences, *J. Geol. Soc., London*, *133*(4), 343–355.

Parnell-Turner, R., N. White, T. Henstock, B. Murton, J. Maclennan, and S. M. Jones (2014), A continuous 55-million-year record of transient mantle plume activity beneath Iceland, *Nat. Geosci.*, *7*(12), 914–919.

Peron-Pinvidic, G., L. Gernigon, C. Gaina, and P. Ball (2012a), Insights from the Jan Mayen system in the Norwegian-Greenland sea-I. Mapping of a microcontinent, *Geophys. J. Int.*, *191*, 385–412.

Peron-Pinvidic, G., L. Gernigon, C. Gaina, and P. Ball (2012b), Insights from the Jan Mayen system in the Norwegian-Greenland sea-II. Architecture of a microcontinent, *Geophys. J. Int.*, *191*, 413–435.

Pilidou, S., K. Priestley, E. Debayle, and O. Gudmundsson. (2005), Rayleigh wave tomography in the North Atlantic: high resolution images of the Iceland, Azores and Eifel mantle plumes, *Lithos.*, *79*, 453–474.

Planke, S., P. A. Symonds, E. Alvestad, and J. Skogseid (2000), Seismic volcanostratigraphy of large-volume basaltic extrusive complexes on rifted margins, *J. Geophys. Res.*, *105*(B8), 19,335–19,351.

Poore, H. R., R. Samworth, N. J. White, S. M. Jones, and I. N. McCave (2006), Neogene overflow of Northern Component Water at the Greenland-Scotland Ridge, *Geochem. Geophys. Geosyst.*, *7*(6).

Poreda, R., J. G. Schilling, and H. Craig (1986), Helium and hydrogen isotopes in ocean-ridge basalts north and south of Iceland, *Earth Planet. Sci. Lett.*, *78*, 1–17.

Price, S., J. Brodie, A. Whitham, and R. Kent (1997), Mid-Tertiary rifting and magmatism in the Traill Ø region, East Greenland, *J. Geol. Soc.*, *154*, 419–434.

Priestley, K., and D. McKenzie (2006), The thermal structure of the lithosphere from shear wave velocities, *Earth Planet. Sci. Lett.*, *244*, 285–301.

Priestley, K., and D. McKenzie (2013), The relationship between shear wave velocity, temperature, attenuation and viscosity in the shallow part of the mantle, *Earth Planet. Sci. Lett.*, *381*, 78–91.

QGIS Devlopment Team (2009), *QGIS Geographic Information System*, Open Source Geospatial Foundation.

Rebesco, M., F. J. Hernández-Molina, D. Van Rooij, and A. Wåhlin (2014), Contourites and associated sediments controlled by deep-water circulation processes: state-of-the-art and future considerations, *Mar. Geol.*, *352*, 111–154.

Rickers, F., A. Fichtner, and J. Trampert (2013), The Iceland Jan Mayen plume system and its impact on mantle dynamics in the north atlantic region: Evidence from full-waveform inversion., *Earth Planet. Sci. Lett*, *367*, 39–51.

Ritsema, J., H. J. van Heist, and J. H. Woodhouse (1999), Complex shear wave velocity structure imaged beneath Africa and Iceland, *Science*, *286*, 1925–1928.

Rudels, B., H. J. Friedrich, and D. Quadfasel (1999), The Arctic circumpolar boundary current, *Deep Sea Research Part II: Topical Studies in Oceanography*, *46*(6), 1023–1062.

Sallarès, V., P. Charvis, E. R. Flueh, and J. Bialas (2003), Seismic structure of Cocos and Malpelo Volcanic Ridges and implications for hot spot-ridge interaction, *J. Geophys. Res.*, *108*(B12), 2564, doi:10.1029/2003JB002431.

References

Sallarès, V., P. Charvis, E. R. Flueh, J. Bialas, and the SALIERI Scientific Party (2005), Seismic structure of the Carnegie ridge and the nature of the Galápagos hotspot, *Geophys. J. Int.*, *161*, 763–788, doi:10.1111/j.1365-246X.2005.02592.x.

Sandstå, N. R., R. B. Pedersen, R. Williams, D. Bering, M. Magnus, M. Sand, and H. Brekke (2012), Submarine Fieldwork on the Jan Mayen Ridge: Integrated Seismic and ROV-Sampling. Norwegian Petroleum Directorate, Stavanger, Norway.

Sandwell, D. T. (2001), Cooling of the oceanic lithosphere and ocean floor topography. University of California, San Diego, CA, USA.

Sandwell, D. T., and Y. Fialko (2004), Warping and cracking of the Pacific plate by thermal contraction, *J. Geophys. Res.*, *109*(B10411), 1–12, doi:10.1029/2004JB003091.

Sandwell, D. T., R. D. Müller, W. H. Smith, E. Garcia, and R. Francis (2014), New global marine gravity model from CryoSat-2 and Jason-1 reveals buried tectonic structure, *Science*, *346*(6205), 65–67.

Schilling, J. (1999), Dispersion of the Jan Mayen and Iceland mantle plumes in the Arctic: A He-Pb-Nd-Sr isotope tracer study of basalts from the Kolbeinsey, Mohns, and Knipovich Ridges, *J.Geophys.Res.*, *104*, 10,543–10,569.

Schilling, J., M. Zajac, R. Evans, T. Johnston, W. White, J. Devine, and R. Kingsley (1983), Petrologic and geochemical variations along the Mid-Atlantic ridge from 29°N to 73°N, *Am. J. Sci.*, *283*, 510–586.

Schmidt, S., and H. J. Götze (1998), Interactive visualization and modification of 3-D models using GIS functions., *Phys.Chem.Earth*, *23*, 289–296.

Schmidt, S., C. Plonka, H.-J. Götze, and B. Lahmeyer (2011), Hybrid modelling of gravity, gravity gradients and magnetic fields, *Geophys. Prospect.*, *59*(6), 1046–1051.

Schoonman, C. M., N. J. White, and D. Pritchard (2017), Radial viscous fingering of hot asthenosphere within the Icelandic plume beneath the North Atlantic Ocean, *Earth Planet. Sci. Lett.*, *468*, 51–61.

Schutt, D. L., and C. E. Lesher (2006), Effects of melt depletion on the density and seismic velocity of garnet and spinel Iherzolite, *J. Geophys. Res.*, *111*, B05,401.

Scott, D. R., and D. Stevenson (1989), A self-consistent model of melting, magma migration and buoyancy-driven circulation beneath mid-ocean ridges, *J. Geophys. Res.*, *94*(B3), 2973–2988.

Shorttle, O., J. Maclennan, and S. M. Jones (2010), Control of the symmetry of plume-ridge interaction by spreading ridge geometry, *Geochem. Geophys. Geosyst.*, *11*(7).

Sleep, N. H. (1997), Lateral flow and ponding of starting plume material, *J. Geophys. Res.*, *102*(B5), 10,001–10,012.

Sørnes, A., and T. Navrestad (1975), Seismic survey about Jan Mayen, *Norsk Polarinst. Årbok*, pp. 37–52.

Stein, C. A., and S. Stein (1992), A model for the global variation in oceanic depth and heat flow with lithospheric age, *Nature*, *359*, 123–129.

Stixrude, L., and C. Lithgow-Bertelloni (2005), Mineralogy and elasticity of the oceanic upper mantle: Origin of the low-velocity zone, *J. Geophys. Res.*, *110*(B03204), doi: 10.1029/2004JB002965.

Stoker, M. S., T. C. E. Van Weering, and T. Svaerdborg (2001), A mid-to late Cenozoic tectonostratigraphic framework for the Rockall Trough, *Geol. Soc. London Spec. Publ.*, *188*(1), 411–438.

Storey, M., R. A. Duncan, and C. Tegner (2007), Timing and duration of volcanism in the North Atlantic Igneous Province: Implications for geodynamics and links to the Iceland hotspot, *Chem. Geol.*, *241*, 264–281, doi:10.1016/j.chemgeo.2007.01.016.

Talwani, M., and O. Eldholm (1977), Evolution of the Norwegian–Greenland Sea, *Geol. Soc. Am. Bull.*, *88*, 969–999.

Tan, P., A. J. Breivik, R. G. Trønnes, R. Mjelde, R. Azuma, and S. Eide (2017), Crustal structure and origin of the Eggvin Bank west of Jan Mayen, NE Atlantic, *J. Geophys. Res: Solid Earth.*, *122*, 43–62, doi:10.1002/2016JB013495, 2016JB013495.

Thiede, J., and G. Hempel (1991), Die Expedition ARKTIS-VII/1 mit FS "Polarstern", *Rep. Polar. Res.*, pp. 1–137.

Thiede, J., C. Jessen, P. Knutz, A. Kuijpers, N. Mikkelsen, N. Nørgaard-Pedersen, and R. F. Spielhagen (2011), Million years of Greenland Ice Sheet history recorded in ocean sediments, *Polarforschung*, *80*(3), 141–149.

Torsvik, T. H., H. E. F. Amundesn, R. G. Trønnes, P. V. Doubrovine, C. Gaina, N. J. Kusznir, B. Steinberger, F. Corfu, L. D. Ashwal, W. L. Griffin, S. C. Werner, and B. Jamtveit (2015), Continental crust beneath southeast Iceland, *Proc Natl Acad Sci U S A*, *112*, E1818–E1827.

Tripati, A. K., R. A. Eagle, A. Morton, J. A. Dowdeswell, K. L. Atkinson, Y. Bahé, C. F. Dawber, E. Khadun, R. M. Shaw, O. Shorttle, et al. (2008), Evidence for glaciation in the Northern Hemisphere back to 44 Ma from ice-rafted debris in the Greenland Sea, *Earth Planet. Sci. Lett.*, *265*(1), 112–122.

Trønnes, R. G., S. Planke, B. Sundvoll, and P. Imsland (1999), Recent volcanic rocks from Jan Mayen: Low-degree melt fractions of enriched northeast Atlantic mantle, *J. Geophys. Res.*, *104*(B4), 7153–7168.

References

Trønnes, R. G., V. Debaille, M. Erambert, F. M. Stuart, and T. Waight (2013), Mixing and progressive melting of deep and shallow mantle sources in the NE Atlantic and Arctic, *Mineral. Mag.*, *77*, 2357.

Tucholke, B. E., and N. C. Smoot (1990), Evidence for age and evolution of Corner seamounts and Great Meteor seamount chain from multibeam bathymetry, *J. Geophys. Res. Solid Earth*, *95*(B11), 17,555–17,569.

Turner, D. L., R. D. Jarrard, and R. B. Forbes (1980), Geochronology and origin of the Pratt-Welker seamount chain, Gulf of Alaska: A new pole of rotation for the Pacific plate, *J. Geophys. Res. Solid Earth*, *85*(B11), 6547–6556.

Uieda, L., and V. C. F. Barbosa (2011), 3D gravity inversion by planting anomalous densities, in *SBGf 2011 Expanded Abstracts*.

Uieda, L., V. C. Oliveira J., and V. C. Barbosa (2013), Modeling the Earth with fatiando a terra, in *Proceedings of the 12th Python in Science Conference (SciPy 2013)*, pp. 96–103.

Van Weering, T., M. Stoker, and M. Rebesco (2008), High-latitude contourites, *Developments in Sedimentology*, *60*, 457–489.

Verhoef, J., W. R. Roest, R. Macnab, J. Arkani-Hamed, et al. (1996), Magnetic anomalies of the Arctic and north Atlantic oceans and adjacent land areas, *Tech. rep.*, Geol. Surv. Canada, Dartmouth.

Vinje, T., and Ø. Finnekåsa (1986), *The ice transport through the Fram Strait*, vol. 186, 1–39 pp., Norsk Polarinstitutt Skrifter.

Vogt, P. R., G. L. Johnson, and L. Kristjansson (1980), Morphology and magnetic anomalies north of Iceland, *J. Geophys.*, *47*, 67–80.

Voss, M., and W. Jokat (2007), Continent-ocean transition and voluminous magmatic underplating derived from P-wave velocity of the East Greenland continental margin, *Geophys. J. Int.*, *170*, 580–604, doi:10.1111/j.1365-246X.2007.03438.x.

Voss, M., M. C. Schmidt-Aursch, and W. Jokat (2009), Variations in magmatic processes along the East Greenland volcanic margin, *Geophys. J. Int.*, *177*, 755–782.

Watts, A. B., and U. S. Ten Brink (1989), Crustal structure, flexure, and subsidence history of the Hawaiian Islands, *J. Geophys. Res.*, *94*, 10,473–10,500.

Weigel, W., E. R. Flüh, H. Miller, a. Butzke, G. a. Dehghani, V. Gebhardt, I. Harder, J. Hepper, W. Jokat, D. Kläschen, S. Kreymann, S. Schüßler, and Z. Zhao (1995), Investigations of the East Greenland continental margin between 70° and 72°N by deep seismic sounding and gravity studies, *Mar. Geophys. .*, *17*, 167–199.

White, R., D. Spence, S. R. Fowler, D. McKenzie, G. K. Westbrook, and A. Bowen (1987), Magmatism at rifted continental margins, *Nature*, *330*, 439–444.

White, R. S. (1989), Initiation of the Iceland Plume and opening of the North Atlantic, in *Extensional tectonics and stratigraphy of the North Atlantic margins*, edited by A. J. Tankard and H. R. Balkwill, pp. 149–154, AAPG Mem., 46, Tulsa, Oklahoma.

White, R. S. (1997), Rift-plume interaction in the North Atlantic, *Phil. Trans. R. Soc. Lond.*, *355*(1723), 319–339.

White, R. S., D. McKenzie, and K. O'Nions (1992), Oceanic crustal thickness from seismic measurements and rare earth element inversion, *J. Geophys. Res.*, *97*(B13), 19,683–19,715.

White, R. S., J. W. Bown, and J. R. Smallwood (1995), The temperature of the Iceland plume and origin of outward-propagating V-shaped ridges, *J. Geol. Soc.*, *152*, 1039–1045.

White, R. S., L. K. Smith, A. W. Roberts, P. A. F. Christie, N. J. Kusznir, and iSIMM Team (2008), Lower-crustal intrusion on the North Atlantic continental margin, *Nature*, *452*, 460–464, doi:10.1038/nature06687.

Wilkens, R. H., G. J. Fryer, and J. Karsten (1991), Evolution of porosity and seismic structure of upper oceanic crust: Importance of aspect ratios, *J. Geophys. Res.*, *96*(B11), 17,981–17,995.

Winkler, A., T. Wolf-Welling, K. Stattegger, and J. Thiede (2002), Clay mineral sedimentation in high northern latitude deep-sea basins since the Middle Miocene (ODP Leg 151, NAAG), *Int. J. Earth Sci.*, *91*(1), 133–148.

Wollenburg, I. (1993), Sedimenttransport durch das arktische Meereis: die rezente lithogene und biogene Materialfracht= Sediment transport by Arctic sea ice: the recent load of lithogenic and biogenic materia, *Berichte zur Polarforschung (Reports on Polar Research)*, *127*, 1–159.

Xue, M., and R. M. Allen (2005), Asthenospheric channeling of the Icelandic upwelling:Evidence from seismic anisotropy, *Earth Planet.Sci.Lett.*, *235*, 167–182.

Yaxley, G. M. (2000), Experimental study of the phase and melting relations of homogeneous basalt + peridotite mixures and implications for the petrogenesis of flood basalts, *Contib. Mineral. Petr.*, *139*, 326–338.

Ye, S., J. P. Canales, R. Rihm, J. J. Danobeitia, and J. Gallart (1999), A crustal transect through the northern and northeastern part of the volcanic edifice of Gran Canaria, Canary Islands, *J. Geodyn.*, *28*, 3–26.

References

Yeo, I. A., N. Augustin, C. W. Devey, M. Deutschmann, L. J. Elkins, T. Laurila, K. Meisenhelder, E. Rivers, M. Rothenbeck, and F. M. van der Zwan (2012), The Northern Kolbeinsey Ridge, North Atlantic: Excess volcanism and ridge relocations close to Jan Mayen, *Eos Trans. AGU*, *1*, 1734, Fall Meet. Suppl., Abstract #OS13B-1734.

Yeo, I. A., T. P. Lebas, N. Augustin, and A. Steinführer (2016), Segment-scale volcanic episodicity: Evidence from the North Kolbeinsey Ridge, Atlantic, *Earth Planet. Sci. Lett.*, *439*, 81–87.

Zelt, C. A., and R. M. Ellis (1988), Practical and efficient ray tracing in two-dimensional media for rapid traveltime and amplitude forward modelling, *Can. J. Explor. Geophys.*, *24*, 16–31.

Zelt, C. A., and R. B. Smith (1992), Seismic traveltime inversion for 2-D crustal velocity structure, *Geophys. J. Int.*, *108*, 16–34.

Zhang, Y., and T. Lay (1999), Evolution of oceanic upper mantle structure, *Phys.Earth Planet. In.*, *114*, 71–80.

Part II

Journal Publications

Paper 1. Crustal structure and origin of the Eggvin Bank west of Jan Mayen, NE Atlantic

Crustal structure and origin of the Eggvin Bank west of Jan Mayen, NE Atlantic

Pingchuan Tan[1], Asbjørn Johan Breivik[1], Reidar G. Trønnes[2], Rolf Mjelde[3], Ryosuke Azuma[4,5], and Sigurd Eide[6,7]

[1]Centre for Earth Evolution and Dynamics, Department of Geoscience, University of Oslo, Oslo, Norway

[2]Centre for Earth Evolution and Dynamics, Natural History Museum, University of Oslo, Oslo, Norway

[3]Department of Earth Science, University of Bergen, Bergen, Norway

[4]Institute of Seismology and Volcanology, Faculty of Science, Hokkaido University, Sapporo, Japan

[5]Research Center for Prediction of Earthquake and Volcanic Eruption, Graduation School of Science, Tohoku University, Sendai, Japan

[6]Navigeo, Oslo, Norway

[7]First Geo, Oslo, Norway

Abstract. The Eggvin Bank, located between the Jan Mayen Island and Greenland, is an unusually shallow area containing several submarine volcanic peaks, confined by two transforms on the Northern Kolbeinsey Ridge (NKR). We represent P and S wave velocity models for the Eggvin Bank based on an Ocean Bottom Seismometer profile collected in 2011, showing igneous crustal thickness variations from 8 km to 13 km. A 2-5 km increase is associated with two separate 20-30 km wide segments under the main seamounts. The oceanic crust has three layers: upper crust (L2A: 2.8-4.8 km/s); middle crust (L2B: 5.5-6.5 km/s); and lower crust (L3: 6.7-7.35 km/s). Both the thick Layer 2(A/B) and the high ratio of Layer 2(A/B) thickness to total crustal thickness indicate that secondary, intraplate magmatism built the seamounts of the Eggvin Bank. The seamount in the north where the crust is thickest has a flat top indicating subaerial exposure, but is deeper than those with rounded tops in the south, and is therefore probably older. Comparing lower-crustal seismic velocity with crustal thickness also indicates that the degree of mantle melting may be higher in the north than in the south. An enriched mantle source presently feeds the NKR magmatism, and probably influenced the Eggvin Bank development also

at earlier times. To what extent the Eggvin Bank has been influenced by the Iceland plume is uncertain, both an enriched mantle component and elevated mantle temperature may have played a role at different times and locations.

Key points:

• A seismic refraction and reflection study of the Eggvin Bank at the northern Kolbeinsey Ridge

• V_p and V_s models of the Eggvin Bank show 8-13 km igneous crustal thickness

• The Eggvin Bank is created by melting of an enriched mantle source both on and off-axis

1 Introduction

The impingement of the Iceland plume head caused extensive magmatism in the Northeast Atlantic during Paleocene-Early Eocene. During the first few million years after continental breakup volcanic margins characterized by thickened oceanic crust were created. After that, most excess volcanism occurred along the Faeroe-Iceland-Greenland ridge (e.g. *Eldholm and Grue*, 1994). Today, the Norwegian island of Jan Mayen has an active volcano, and recent research (*Kandilarov et al.*, 2012, 2015) has increasingly highlighted the surrounding areas affected by post-breakup magmatic processes (Fig. 2.1). The Eggvin Bank is located between Jan Mayen and the east coast of Greenland, straddling the axial zone of the Northern Kolbeinsey Ridge (NKR). It is an unusually shallow area, containing several submarine volcanic peaks as well as large central volcanic edifices as shallow as 30 m below sea-level (*Haase et al.*, 2003). The southern margin of the Eggvin Bank coincides with a small offset on the Kolbeinsey Ridge, whereas the northern boundary is the West Jan Mayen Fracture Zone (WJMFZ), partly a large transform fault between the Kolbeinsey and Mohn's ridges (Fig. 2.2). The NKR has a slow half-spreading rate of 9 mm/year (*Mosar et al.*, 2002; *Gaina et al.*, 2009). Compared with the middle Kolbeinsey Ridge (MKR), the magmatism at NKR including the Eggvin Bank is enriched in incompatible elements and radiogenic isotopic compositions (e.g. *Campsie et al.*, 1990; *Haase et al.*, 2003; *Mertz et al.*, 2004; *Elkins et al.*, 2011, 2016). The asymmetric bathymetry across the spreading axis, as well as indistinct magnetic lineations on the Eggvin Bank (*Maus et al.*, 2007) may indicate a significant off-axis magmatic activity. The majority of the seamounts are located between NKR and Jan Mayen. Large volcanic edifices with high magma supply straddle the spreading axis (*Yeo et al.*, 2012; *Elkins et al.*, 2013; *Yeo et al.*, 2016). The development of the Eggvin Bank is affected by the proximity to the

Kolbeinsey and Mohn's spreading ridges, the Jan Mayen Micro-Continent (JMMC), and the active WJMFZ (*Yeo et al.*, 2012; *Elkins et al.*, 2013).

The JMMC separated from east Greenland at about 24 Ma (*Talwani and Eldholm*, 1977; *Vogt et al.*, 1980; *Gaina et al.*, 2009) (Fig. 2.2). The continent-ocean transition (COT) along the JMMC margins was constrained by *Peron-Pinvidic et al.* (2012a,b) mainly based on seismic reflection data combined with magnetic and gravity data. Wide-angle seismic data further constrains the northern boundary of the JMMC which coincides with the continuation of the northern lineament of the East Jan Mayen Fracture Zone (EJMFZ) (*Kandilarov et al.*, 2012). Eastern and western boundaries have been defined by *Breivik et al.* (2012a), and *Kodaira et al.* (1998a), respectively (Fig. 2.2).

Based on early refraction data, *Sørnes and Navrestad* (1975) concluded that the crustal thickness in the Jan Mayen and Eggvin Bank area is around 16 km, while *Evans and Sacks* (1979) suggested that the crustal thickness is about 20 km based on the study of earthquakes along the WJMFZ. Two regional 3D crustal models of the NE Atlantic have recently been published. *Funck et al.* (2016) indicate a crustal thickness of 6-8 km in the Eggvin Bank, but lack seismic constraints there. With the added control of gravity using inversion, *Haase et al.* (2016) found a crustal thickness of 10-15 km. Other seismic refraction surveys document surrounding areas: the oceanic crustal thickness in the Greenland basin is around 4-5 km (*Klingelhöfer et al.*, 2000a; *Voss and Jokat*, 2007; *Voss et al.*, 2009; *Kandilarov et al.*, 2012); the northern Iceland plateau has a larger crustal thickness around 9.5 km (*Kodaira et al.*, 1998b; *Mjelde et al.*, 2002, 2007); the continental crustal thickness is more than 25 km at the northern boundary of the JMMC, while the oceanic crustal thickness north of the Jan Mayen island across the WJMFZ is up to 12 km (*Kandilarov et al.*, 2012).

The origin of the Eggvin Bank has been the subject of debate. Based on the early seismic studies and the geochemical analysis of dredged samples from the Eggvin Bank, *Campsie et al.* (1990) suggested that the thickened Eggvin Bank could be due to underlying continental crust extending from JMMC. Some authors have ascribed the Jan Mayen and Eggvin Bank volcanism to a mantle plume around Jan Mayen (e.g. *Schilling et al.*, 1983; *Elkins et al.*, 2016), and *Morgan* (1983) suggested that the Eggvin Bank could be a hot spot track. Several geochemical studies, however, suggest a likely connection with the lateral flow of Iceland plume material (e.g. *Trønnes et al.*, 1999; *Mertz et al.*, 2004). The V-shaped ridges along the Kolbeinsey spreading axis also indicate that the lateral flow of pulses from the Iceland plume extends all the way to the WJMFZ (*Jones et al.*, 2002). The Jan Mayen and Eggvin Bank volcanism has also been related to minor spreading or
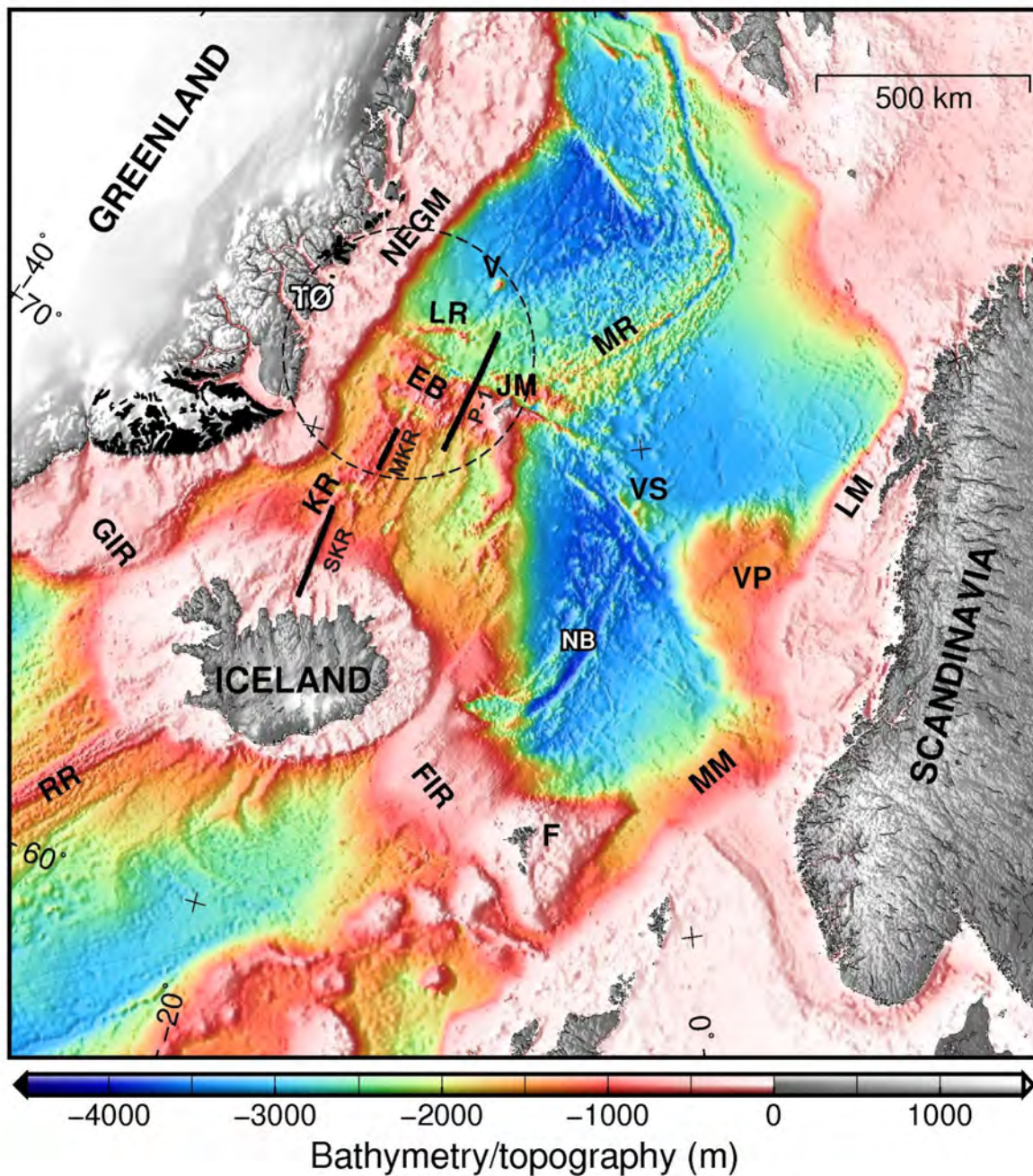
Figure 2.1: Bathymetry map (ETOPO2v2) (*National Geophysical Data Center*, 2006) showing regional features, where the study area (Fig. 2.2) is indicated by the dashed circle, and the studied profile is marked P-1 (Profile-1). The position of older OBS profiles by *Kodaira et al.* (1997) (MKR) and *Hooft et al.* (2006) (SKR) is also shown. Early Cenozoic basalt flows or intrusions are illustrated as black areas onshore Greenland (*Noble et al.*, 1988). EB: Eggvin Bank, F: Faeroes, FIR: Faeroes-Iceland Ridge, GIR: Greenland-Iceland Ridge, JM: Jan Mayen, KR: Kolbeinsey Ridge, LM: Lofoten Margin, LR: Logi Ridge, MKR: Middle Kolbeinsey Ridge, MM: Møre Margin, MR: Mohn's Ridge, NB: Norway Basin, NEGM: Northeast Greenland Margin, RR: Reykjanes Ridge, SKR: South Kolbeinsey Ridge, TØ: Traill Ø, VP: Vøring Plateau, VS: Vøring Spur, and V: Vesteris Seamount.
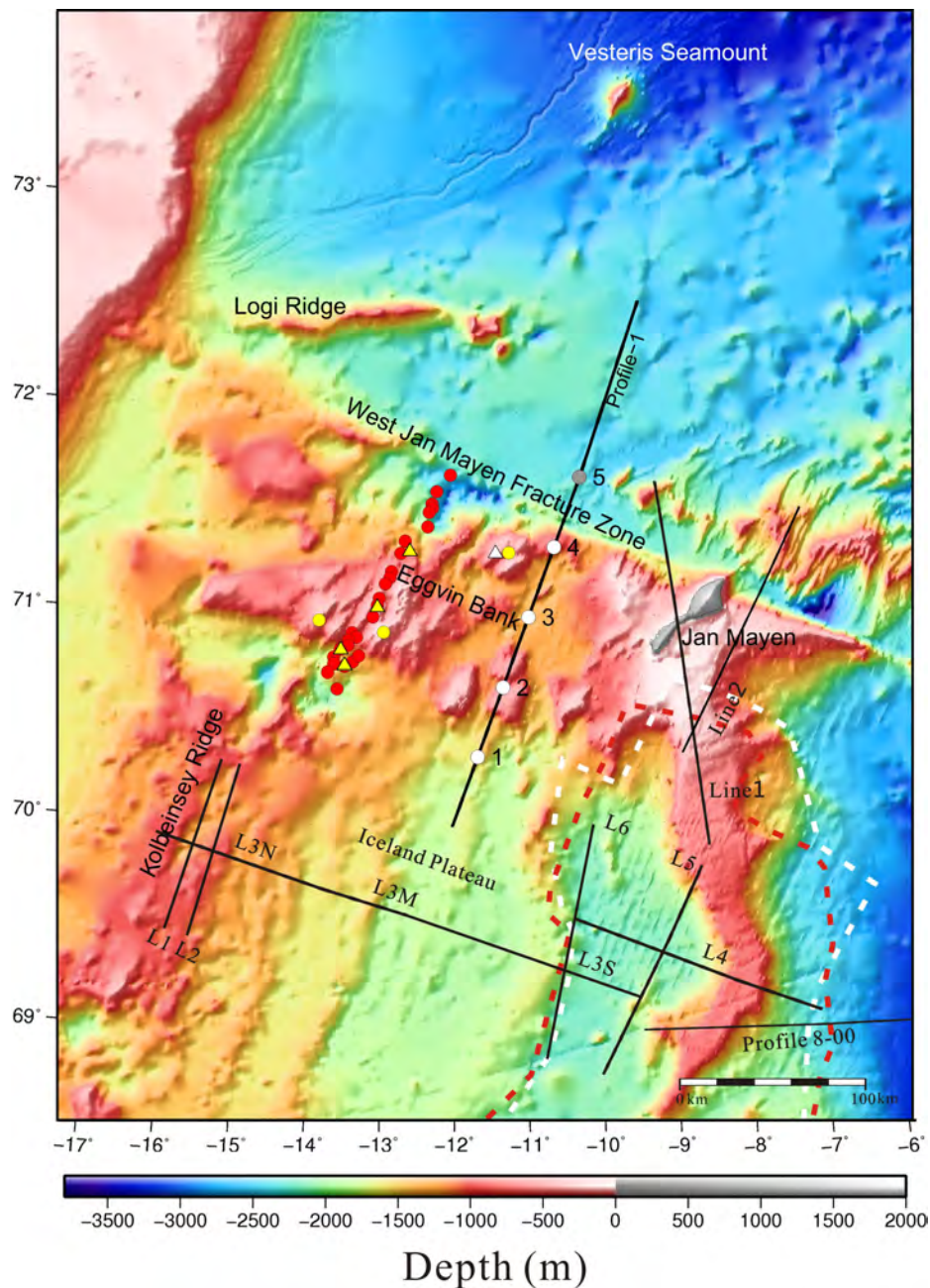
Figure 2.2: Layout of the survey shown on IBCAO (v.3) bathymetry (*Jakobsson et al.*, 2012). Profile-1 is the OBS profile, where circles show OBS positions, and white fill indicates useful data. Several previous OBS based crustal studies around Eggvin Bank are shown (Jan Mayen microcontinent (L3S, L4, L5, L6), Kolbeinsey Ridge (L1, L2, L3N), Iceland Plateau (L3M) (*Kodaira et al.*, 1997, 1998a,b), southern part of the Jan Mayen microcontinent (Profile 8-00) (*Breivik et al.*, 2012a), and northern part of the Jan Mayen microcontinent (Line1 and Line2) (*Kandilarov et al.*, 2012)). The north part of the Kolbeinsey ridge (NKR) has been investigated geochemically from dredged samples (red circles (*Haase et al.*, 2003), yellow circles (*Mertz et al.*, 2004), yellow triangles (*Elkins et al.*, 2011), and white triangles (*Campsie et al.*, 1990)). The white dashed line represents the location of the Continental Ocean Boundary (COB) around the JMMC by *Breivik et al.* (2012a) incorporating results from *Kandilarov et al.* (2012), while the red dashed line shows the COB by *Peron-Pinvidic et al.* (2012a,b).

leakage along WJFMZ (*Imsland*, 1986; *Havskov and Atakan*, 1991; *Gernigon et al.*, 2008; *Kandilarov et al.*, 2012). However, most of the magmatism is located to the south of the active transform, suggesting that this is not an important mechanism.

In this study, we use wide-angle seismic data in order to constrain the crustal velocity structure in detail along a single transect over the Eggvin Bank. This will be used to discuss the distribution of excess magmatism, process that can cause it, and to roughly address possible differences in timing of magmatic events along profile.

2 Data acquistion and processing

This marine geophysical survey was conducted between Jan Mayen and East Greenland during early fall of 2011 by the R/V Håkon Mosby. It is a collaboration between the Department of Geoscience, University of Oslo, Department of Earth Science, University of Bergen, and the Institute of Seismology and Volcanology, Hokkaido University, Sapporo, Japan. The seismic source consisted of four equal-sized Bolt air-guns with a total volume of 78.6 l, which were fired every 200 m. The ocean bottom seismometers (OBS) were deployed approximately N-S from the Greenland Basin across the Eggvin Bank (Fig. 2.2). Four OBSs returned good data sets, while OBS 5 in the north failed. Each OBS is composed of 4.5 Hz three-component geophones. The air-gun signals were recorded by a digital audio tape recorder with a 16 bit analog to digital converter sampling at 256 Hz. A single-channel streamer was also used to record near-vertical seismic reflection data.

The OBS pre-processing consisted of extracting a 60s record length of each shot, OBS position adjustment and linking to navigation. The OBS data processing consisted of 8 km/s or 4.6 km/s velocity reduction for P and S wave data respectively, 5-12 Hz band-pass filtering, offset-dependent amplitude scaling or automatic gain control (2s window), and spiking deconvolution. The sea-floor depth was obtained from echo-sounder recordings on board the ship. The single channel streamer profile was processed with spiking deconvolution, 5-60 Hz bandpass filter and amplitude corrections with a geometrical exponential factor of 1.2. It produced good-quality reflection seismic data, which was used to constrain sedimentary thickness for the starting velocity model (Fig. 2.3). Using a water velocity of 1480 m/s gave a good fit between the seafloor depth observed from echo-sounder recordings and the seabed in the seismic profile.
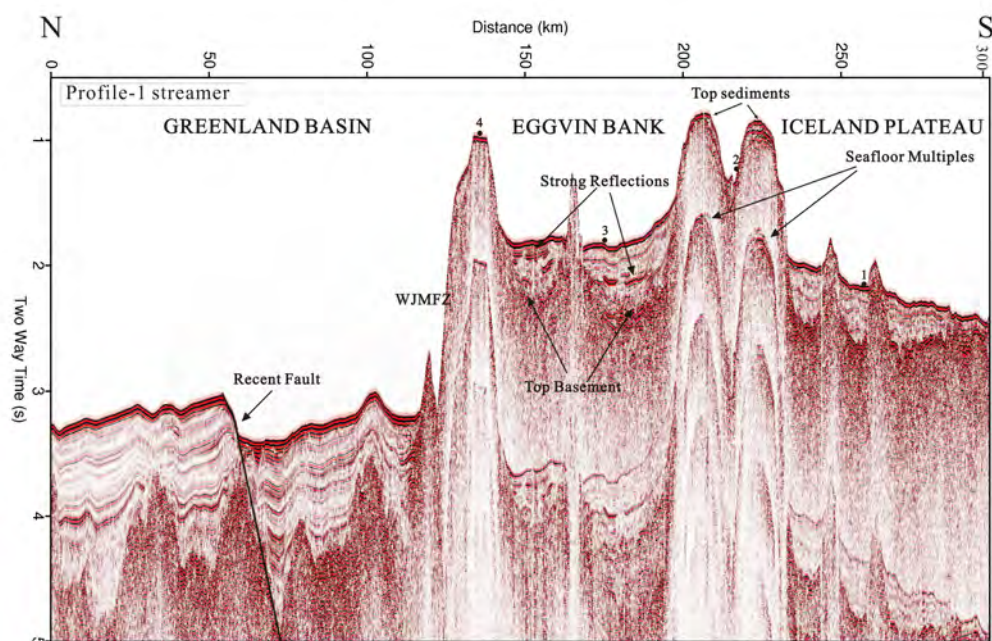
Figure 2.3: Single-channel streamer reflection seismic data of Profile-1. OBS locations are illustrated with black circles, with the instrument number above. WJFMZ: West Jan Mayen Fracture Zone.

3 Geological setting

The sediments at the Eggvin Bank and in the surrounding areas consist of mud and silt with some additional ice-drafted materials deposited during the last glacial periods (e.g. *Haase et al.*, 2003; *Thiede and Hempel*, 1991). A thick sedimentary sequence is observed in the Greenland Basin. The oceanic crust north of the WJMFZ dates from chrons C6-C7 (*Maus et al.*, 2007; *Engen et al.*, 2008), which indicates that all sediments deposited along profile in the Greenland Basin are younger than 25 Ma. A normal fault offsetting sedimentary strata observed in the Greenland Basin indicates recent tectonic activity north of the Eggvin Bank. Three large seamounts are observed along the Eggvin Bank profile with two of them having thin sedimentary units on top (Fig. 2.3). The northern seamount is almost sediment free and has a flat top, indicating that it has been eroded above or near the sea surface. At a half-spreading rate of 9 mm/year, the age would be around 7 Ma in the northern Eggvin Bank, increasing to around 10-11 Ma in the southern Eggvin Bank at the profile position. The sedimentary layers between the southern and northern seamounts have some strong discontinuous reflective layers, which could be interpreted as basaltic intrusions or flows. The upper sedimentary layers on

the Eggvin Bank are inclined and follow the slopes of the surrounding peaks, while the sedimentary package on the Iceland Plateau, which has crust around 13.5 Ma old along the profile (*Maus et al.*, 2007; *Engen et al.*, 2008), decrease in thickness towards the south.

4 Velocity modeling

4.1 P-wave modeling

The 2D velocity modeling was done with Rayinvr forward/inverse ray tracing software developed by *Zelt and Ellis* (1988); *Zelt and Smith* (1992). The model is processed layer by layer from top water layer to bottom mantle layer by fitting traveltimes with increasing offsets. The model is built on a limited number of velocity and depth nodes. The thickness and velocity of the sedimentary package was calculated by an empirical velocity-depth trend (V_p=1.8+0.7Z km/s, Z: depth in km) based on nearby crustal studies (*Kodaira et al.*, 1997; *Voss et al.*, 2009; *Breivik et al.*, 2012a; *Kandilarov et al.*, 2012). The bathymetry and top basement derived from the echo sound recordings and single-channel streamer reflection seismic line, respectively, are modeled with denser depth nodes. The misfit between the interpreted and modeled traveltimes is estimated by using χ^2 analysis. The χ^2 value evaluates the goodness of fit by the given uncertainty of the interpretation, and a value of 1 or lower per phase represents a fit (*Zelt and Smith*, 1992). The main uncertainties are arrival time picking, instrument location, shot timing and the bathymetry (*Hooft et al.*, 2000; *Ljones et al.*, 2004). Minor relocations of some OBSs had to be made (OBS1: 19 m shallower, OBS2: 14 m shallower, OBS3: 12 m shallower). Location uncertainties of up to a few tens of meters would affect travel times by 10-20 ms with typical upper basement/sediment velocities. In this study, we have manually picked a total of 479 refractions and 101 reflections picks. Each pick of arriving phase is assigned an uncertainty in time. It is often assigned to a typical cycle width of the phase (*Breivik et al.*, 2003). The uncertainties of the short offset arrivals from sedimentary layers, and upper and middle parts of crust (P_{g1} and P_{g2}), which are usually clear and marked by higher frequency than later arrivals, are estimated to ± 50 ms, while lower part of crust (P_{g3}) and Moho arrivals ($P_M P$ and P_n) are assigned uncertainties of ± 75 ms and ± 100 ms, respectively. The arrivals from most layers (except P_{g1}) have a fit with χ^2 less than 1 (Tab. 2.1). The ray tracing and traveltime fit of OBSs 1, 2, 3 and 4 are illustrated in Figs. 2.4-2.7, and the velocity model in Fig. 2.8.

Figure 2.4: Data, interpretation and ray tracing of OBS1, (a) Vertical component data of OBS1 reduced by 8 km/s (5-12 Hz band-pass filtered and offset-dependent scaling). (b) Comparison between calculated (black solid line) and interpreted traveltime (colored vertical bars) for OBS1 with data in the background. (c) Ray tracing of the velocity model.
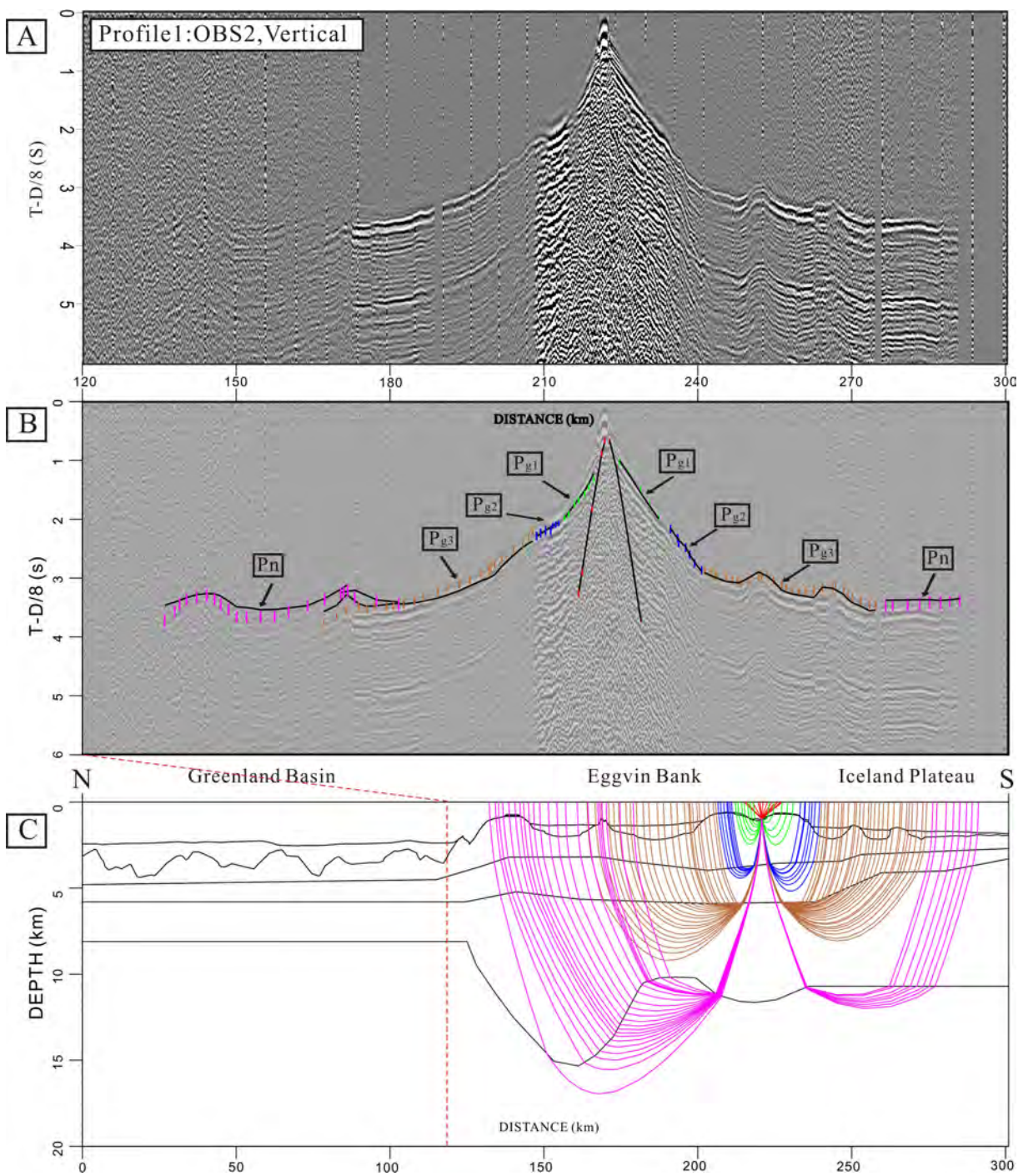
Figure 2.5: Data, interpretation and ray tracing of OBS2. (a) Vertical component data of OBS2 reduced by 8 km/s (5-12 Hz band-pass filtered and offset-dependent scaling). (b) Comparison between calculated (black solid line) and interpreted traveltime (colored vertical bars) for OBS2 with data in the background. (c) Ray tracing of the velocity model.
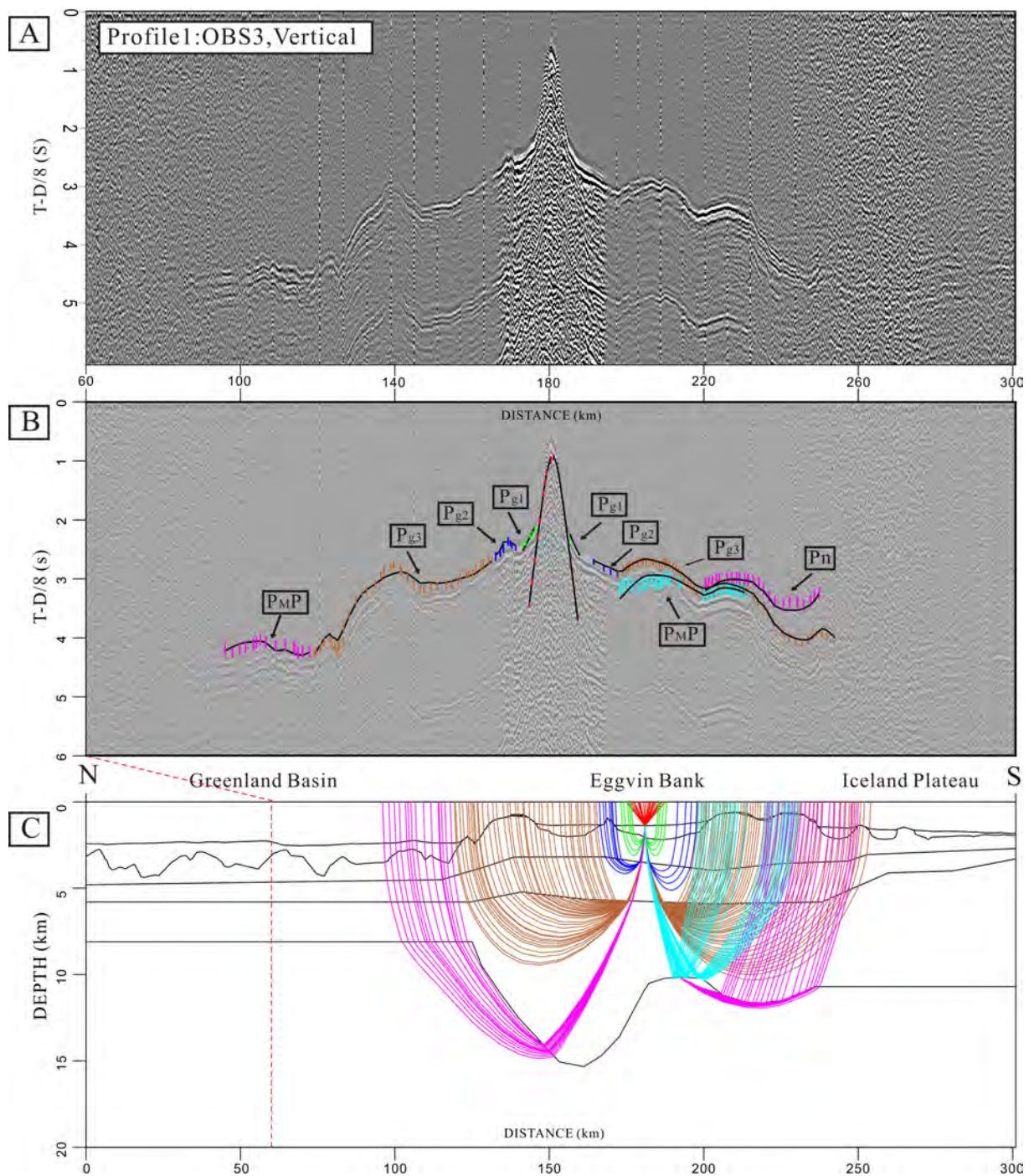
Figure 2.6: Data, interpretation and ray tracing of OBS3. (a) Vertical component data of OBS3 reduced by 8 km/s (5-12 Hz band-pass filtered and offset-dependent scaling). (b) Comparison between calculated (black solid line) and interpreted traveltime (colored vertical bars) for OBS3 with data in the background. (c) Ray tracing of the velocity model.
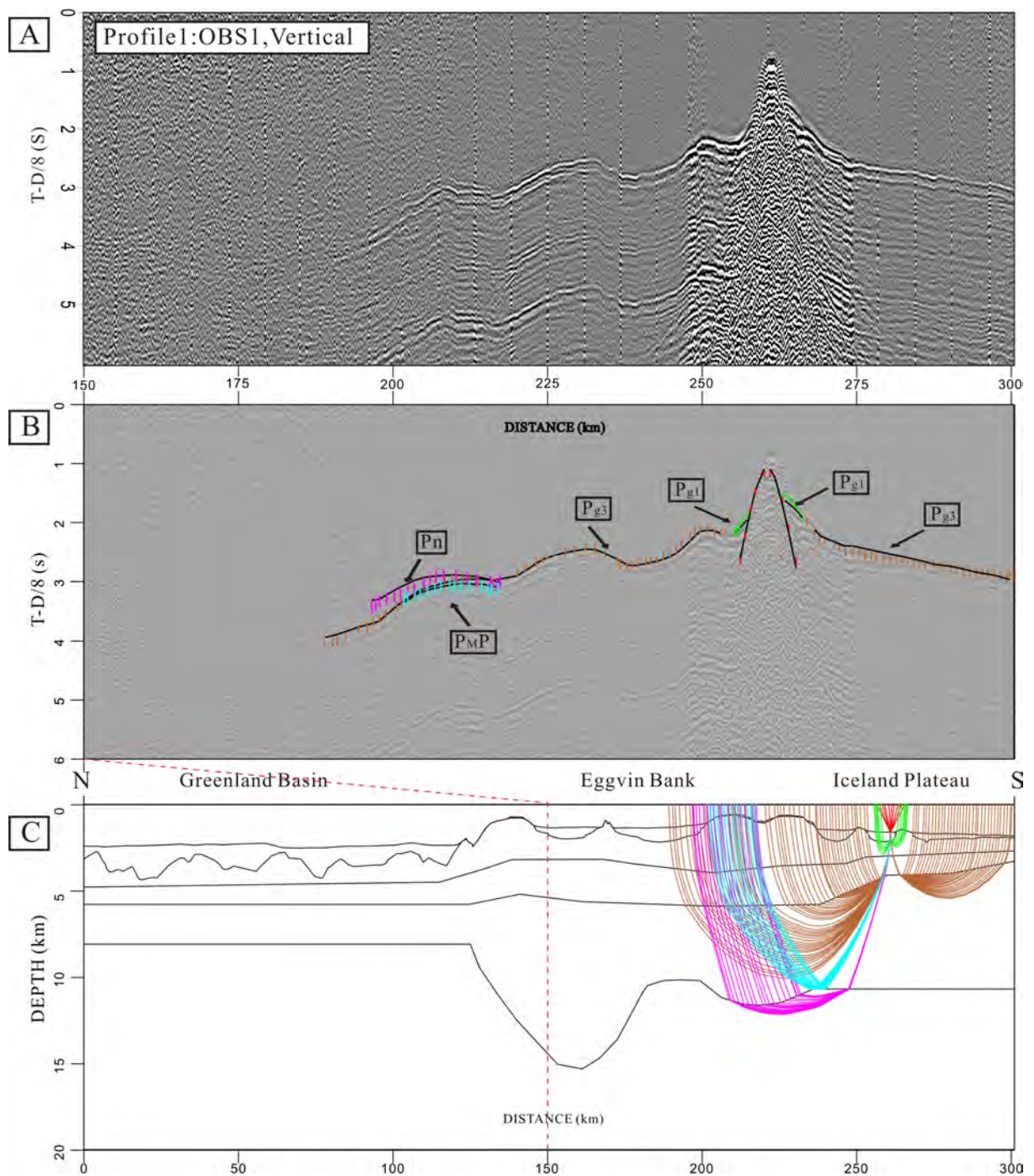
Figure 2.7: Data, interpretation and ray tracing of OBS4. (a) Vertical component data of OBS4 reduced by 8 km/s (5-12 Hz band-pass filtered and automatic gain control (2s window) scaling). (b) Comparison between calculated (black solid line) and interpreted traveltime (colored vertical bars) for OBS4 with data in the background. (c) Ray tracing of the velocity model.
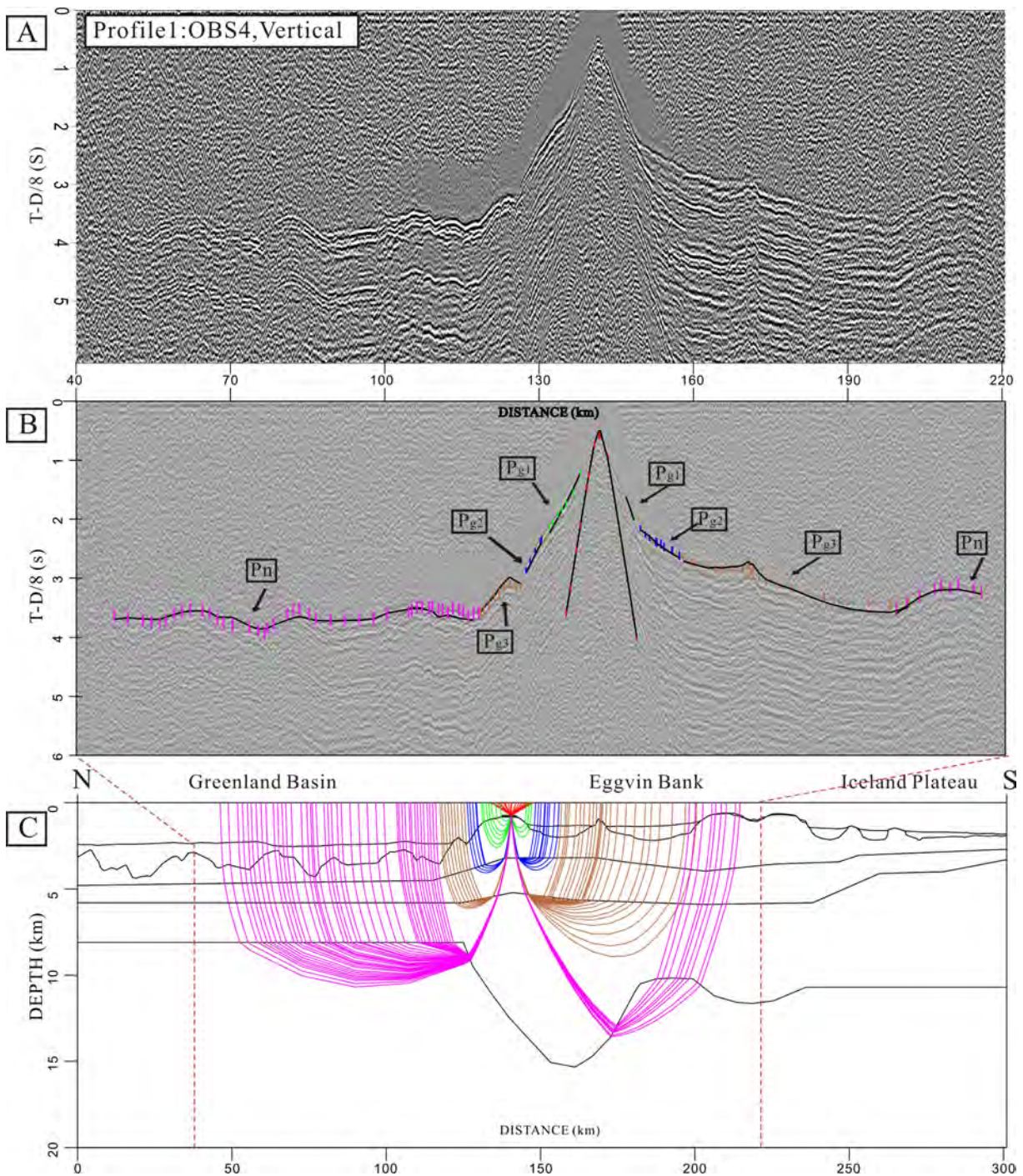
Table 2.1: Seismic model fit statistics for individual major phases (P wave), and summary for all phases.

Phase	No. rays	RMS Δt (ms)	χ^2
Water	60	41	0.689
P_{g1}	42	50	1.029
P_{g2}	39	40	0.518
P_{g3}	259	66	0.777
P_n	139	78	0.615
$P_M P$	41	72	0.534
All phases	580	65	0.707

Poor seismic coverage of the Greenland Basin gives limited information about the crust there, while most parts of the Eggvin Bank and the Iceland Plateau to the south (135-280 km) are better covered. The crust was modeled using of three layers, a lower velocity upper crust (2.8 km/s-4.8 km/s), middle crust (5.5 km/s-6.5 km/s) and a high velocity, low-gradient lower crustal layer (6.7 km/s-7.35 km/s). Compared to the avarage oceanic crust (*White et al.*, 1992; *Christeson et al.*, 1994), the velocities of upper crust, middle crust, and lower crust are within the range of the oceanic layer 2A, layer 2B, and layer 3, respectivity. Layer 2A is extrusive and consists of pillow lavas, layer 2B corresponds to sheeted dikes and layer 3 corresponds to gabbros (*Detrick et al.*, 1994; *Dilek*, 1998). The upper layer (layer 2A), including the seamounts and the uppermost crystalline crust, is well constrained by the P_{g1} and P_{g2} phases. The thickness of 2A is about 1-1.5 km thick in the Iceland Plateau, but increase to about 2.5 km in the seamounts of the Eggvin Bank. The basement velocity of the seamounts are below 3.15 km/s, which is lower than the 3.5-3.8 km/s velocity found in the Iceland Plateau to the south. There are only indirect constraints on the upper-crustal velocity north of the WJMFZ, where the P_n arrival times are modulated by the top basement topography, indicating similar velocities as to the south of the Eggvin Bank. The middle crust (layer 2B) is well constrained by the refracted arrivals. It is thicker at the Eggvin bank (average 2.5 km) than at the Iceland Plateau (average 1 km). The oceanic layer 2 (upper and middle crustal layer) thickness is quite uniform (4.2 ± 0.5 km) along the Eggvin Bank regardless of the total crustal thickness. Therefore crustal thickening is mainly resulting from lower crustal variations. There are two crustal roots with quite different Moho depths. The northern (135 km-190 km) has a maximum crustal thickness around 13 km and is constrained by upper mantle refractions (P_n) of OBSs 2-4. The crustal thickness in the south (190 km-235 km) is constrained by P_n and a few Moho reflections ($P_m P$) of OBSs 1-3 to a maximum of

around 10 km. The velocity of the lower crust (layer 3) is controlled in this part of the model by P_{g3} phases (6.7 km/s to 7.35 km/s). The upper mantle velocity is at 7.7 km/s unusually low under the northern seamount. There is some freedom in the model to reduce Moho depth and lower crustal velocity here, but that would require even lower mantle velocity. Ray tracing through inverse modeling by adjusting a set of selected lower-crustal velocities, Moho depth, and upper mantle velocities in this region, show the best fit for a velocity of 7.7 and 7.35 km/s in the upper mantle and lower crust, respectively. The southern 100 km of the model covers thinner ocean crust(8.5 km), where the velocity in the lower crust (layer 3) ranges from 6.7 to 7.15 km/s and the upper mantle velocity is estimated to 7.9-7.95 km/s. This result is consistent with the the study of the nearby Iceland Plateau (*Kodaira et al.*, 1997, 1998a).

Based on the average velocity of each layer, Fig. 2.9 represents the crustal velocity anomalies between 135 km and 301 km. In the upper crustal layer, low velocity anomalies are found beneath the seamounts at the Eggvin Bank. The velocity anomalies in the two main peaks at 135-150 km and 200-220 km have amplitudes of -0.1 km/s and -0.3 km/s respectively, while the amplitude increase to -0.4 km/s under the smaller peak between 160 km and 175 km. The near-surface velocities under the seamounts at 200-220 km and 160-175 km are mainly constrained by P_{g1} and P_{g2} from OBS2 (Fig. 2.5) and P_{g2} from OBS3 (Fig. 2.6), respectively. The variations in near-surface velocities may be associated with the formation ages of the seamounts. The low velocity anomalies may indicate relatively young extrusives with high density of cracks, and higher porosity and low degree of compaction (*Jacobson*, 1992; *Hooft et al.*, 2006), while the porosity could be reduced by cementation processes for older extrusives. Strong discontinuous reflections observed between 140 km and 190 km in the sediments may represent intrusions or lava flows, indicating that magmatic activity occurred after some sedimentation had taken place (Fig. 2.3). Upper crustal velocities start to increase at the southernmost peak of the Eggvin Bank, and becomes up to 0.4 km/s higher than average past 255 km. The middle crustal high velocity (≤ 0.2 km/s) found in the central Eggvin Bank (175-230 km) may be due to the presence of high density basaltic intrusives (*Menke et al.*, 1998). In addition, the upper and middle/lower crust (layer 2/layer 3) thickness ratio varies from 1:1 to 1:3 from the Eggvin Bank to the Iceland Plateau, indicating more extrusives at the Eggvin Bank. The lower crust velocity anomalies in the Eggvin bank have large variations between the two crustal roots. The northern root between 135 and 190 km has an up to 0.15 km/s increase, while the southern root (190 km - 235 km) structure is -0.1 km/s
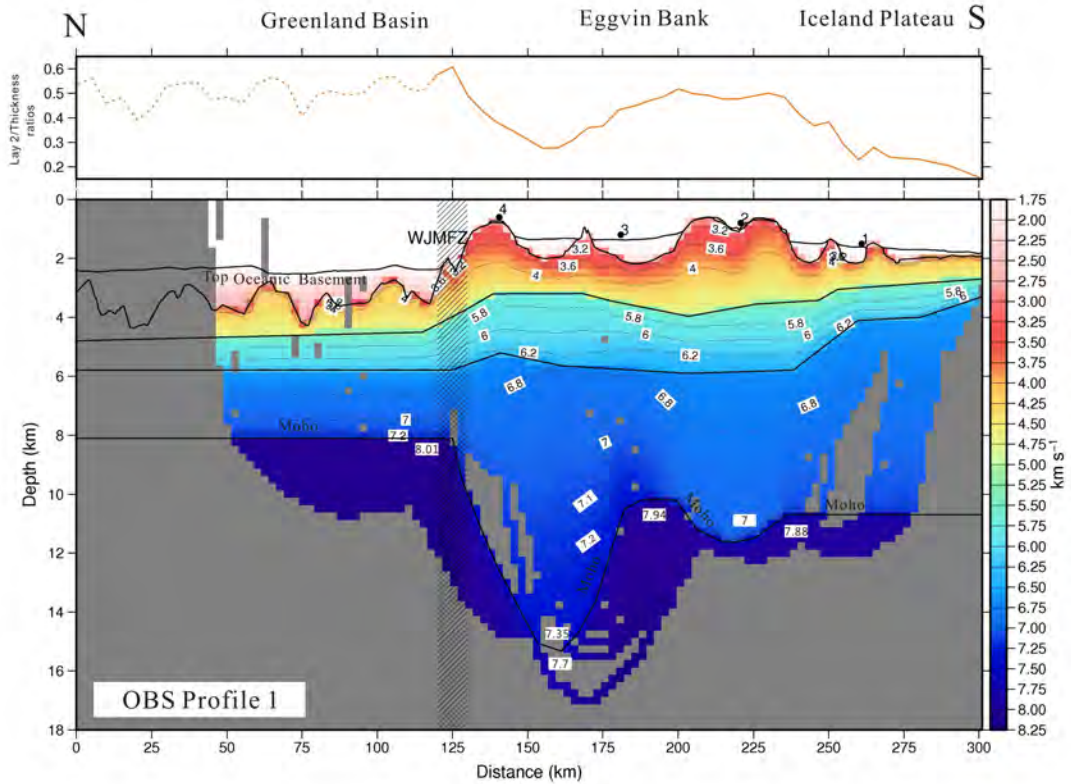
Figure 2.8: Gridded crustal velocity model of profile 1. The area not covered by rays are masked. The OBS locations are illustrated on the seafloor with numbers. The West Jan Mayen Fracture Zone (WJMFZ) is presented by hachures. Velocity contour interval is 0.4 km/s in the upper crust, 0.2 km/s in the middle crust, and 0.1 km/s in the lower crust. The velocities of the upper mantle are also shown. V_P velocities are given by small numbers. The Layer 2 thickness/total crustal thickness-ratio along profile is shown above.
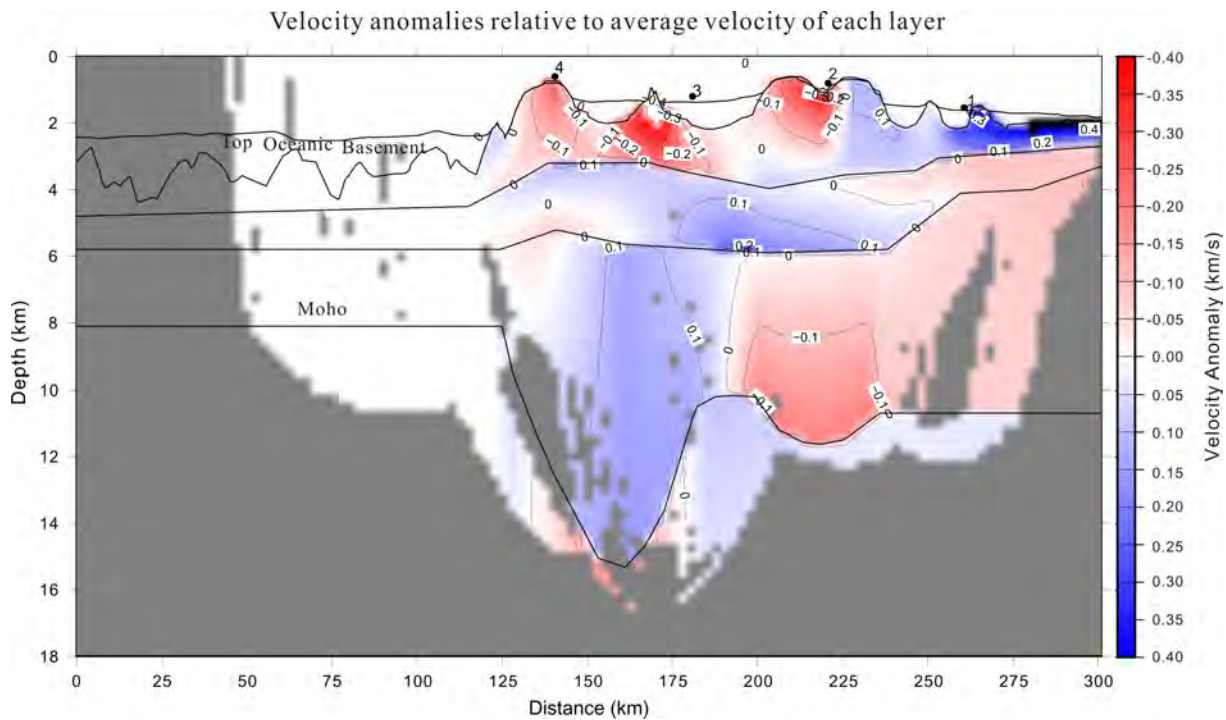
Figure 2.9: Velocity anomalies relative to mean velocity of each layer between 120 km and 301 km.

below average. This variation may indicate different melting degrees or source in these two areas.

4.2 P-wave model resolution and uncertainties

The ray coverage density (2.5 by 0.25 km distance-depth grid) is shown in Fig. 2.10a. Areas near OBSs and the upper parts of the lower-crust have the highest ray coverage density. In order to estimate the model sensitivity to nodes, we determined the resolution values of the P-wave velocity and depth nodes of both upper and lower bundaries by using the inversion function of rayinvr (*Zelt and Smith*, 1992). We show gridded velocity resolution values in Fig. 2.10b. Depth node resolution is also indicated by the size of the circle enclosing it, larger meaning better constraints. The upper crustal (layer 2A, 2B) velocities, which are constrained by short offset refracted arrivals (P_{g1}, P_{g2}), are not highly resolved at distance from the OBSs. The best velocity constraints are found at upper parts of lower crust (layer 3) from 205 km to 250 km. The upper and middle crust (layer 2A, 2B) depth nodes in most parts of the Eggvin Bank (135-235 km) are well constrained (average above 0.5), while the Moho depth nodes are less well constrained.

The best Moho depth constraints are found at the WJMFZ and at the southern Eggvin Bank.

To quantify the uncertainties of the lower crustal velocity and Moho depth, we use an automated search through a range of selected lower crustal velocity nodes and Moho depth nodes (using P_{g3}, P_MP, and P_n phases). Changes in Moho depth can be accommodated with changes in V_p in the lower crust and still produce a reasonable fit. In each step, depth nodes are changed by 0.1 km, while velocity nodes will go through all iterations over a selected interval at 0.01 km/s steps. The fit statistics are documented after running through the chosen intervals between 135-190 km and between 190-235 km, 8183 different models in total. This gives a good indication of the maximum range of velocity and Moho depth within a resonable fit for the crustal roots at the northern and southern Eggvin Bank seperately (e.g *Breivik et al.*, 2012a, 2014). The contoured χ^2 and RMS Δt are summarized in Fig. 2.11. The loss of rays is indicated by the background shading. It starts at 1 percent loss, and reaches black at 10 percent loss. Based on $\chi^2 \leq 1$ and few rays lost, we estimate model uncertainties at the northern Eggvin Bank (135-190 km) to be -0.8/2.5 km for Moho depth and -0.4/0.35 km/s for the lower crustal velocity. For the southern Eggvin Bank (190-235 km), the uncertainties of the Moho depth and lower crustal velocity are estimated to be -1.1/1.5 km and ±0.3 km/s. Other geophysical data (e.g. gravity data) and isostasy analysis can sometimes supply further constraints. However, the uncertainty in lower-crustal/upper mantle velocities and Moho depth will translate into a similar uncertainty in lower-crustal/upper mantle densities and Moho depth. Additional uncertainties come from the expected changes of the lithospheric temperature/density structure next to the transform, and the unconstrained depth extent of the upper-mantle velocity/density anomaly. Therefore, a gravity/isostasy model is not expected to reduce the seismic model uncertainty.

4.3 S-wave modeling

The S wave data is extracted from the horizontal components of the OBS instruments. The orientation of the horizontal components is arbitrary on the seafloor, but can be estimated from a 3D polarization analysis (*Maercklin*, 2007). The two horizontal components are separately rotated into radial and transverse directions. The S wave energy will then be in the radial in-line direction mostly. Reorienting the instrument may therefore improve the S/N ratio. In this study, the horizontal components of OBS1, OBS3 and OBS4 have been re-oriented 305°, 202°, and 179° respectively, while OBS2 contained only one horizontal component with useful reading. Two types of S wave phases (PPS and PSS waves) have
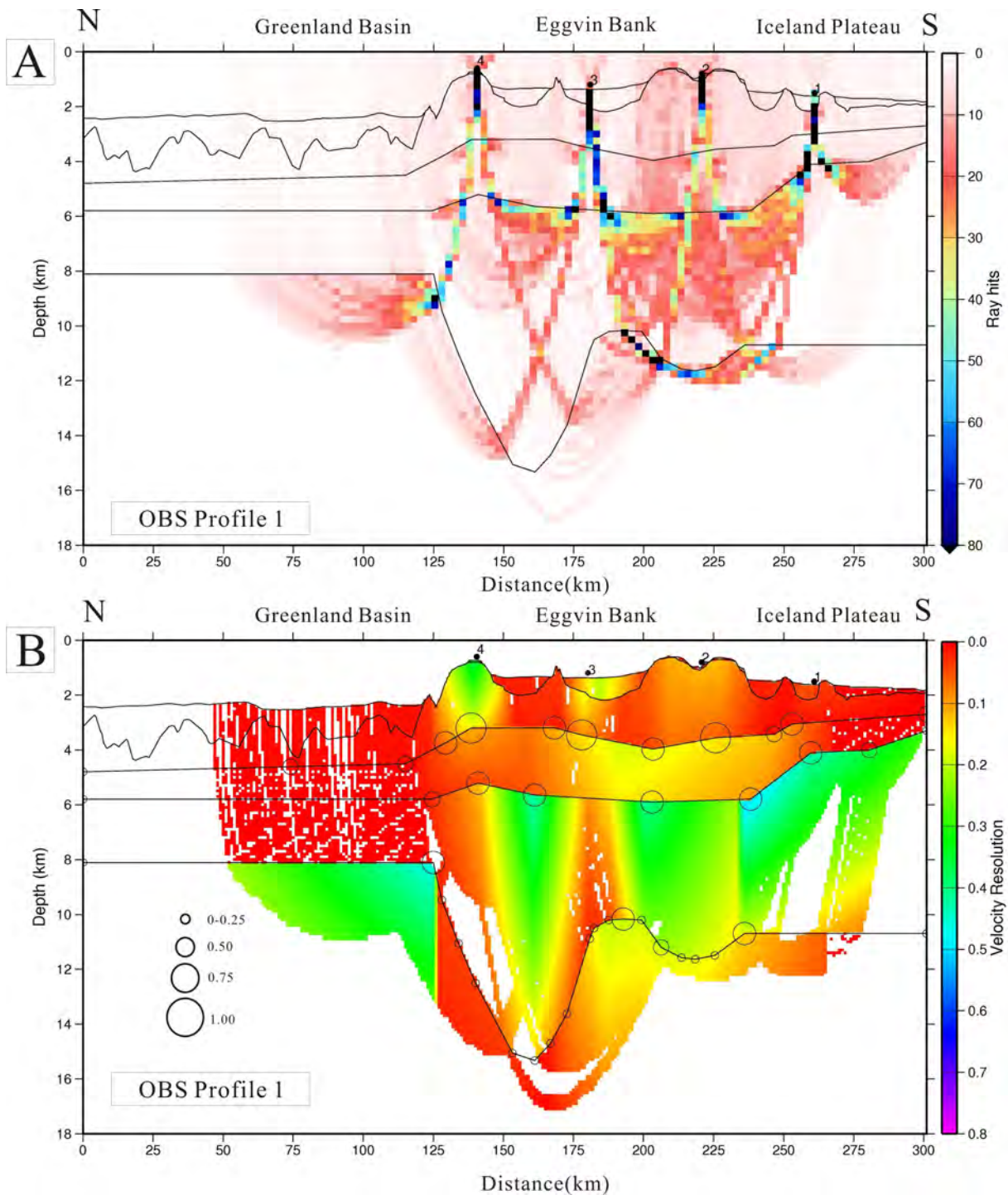
Figure 2.10: Ray coverage, velocity and depth node resolution. (A) Gridded ray coverage within a 2.5 by 0.25 km distance-depth grid. (B) Gridded P-wave resolution parameters obtained from ray-tracing inversion modeling. P wave velocity node resolution is shown by color, while depth node resolution is illustrated by the circle size.
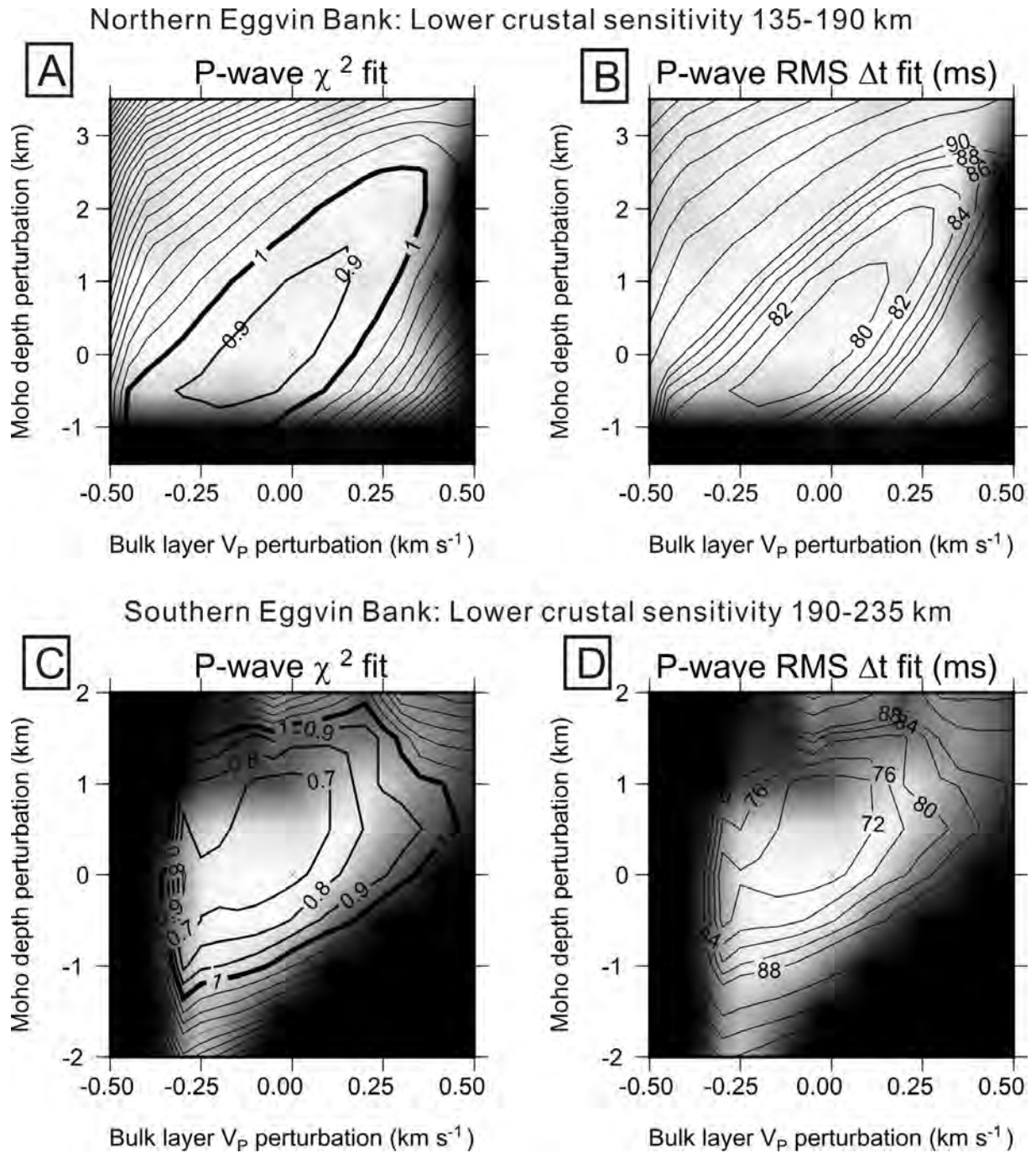
Figure 2.11: P-wave model sensitivity to lower crustal velocity variations against Moho depth based on P_{g3}, $P_M P$, and P_n phases. Model sensitivity for the northern Eggvin Bank (A and B) and southern Eggvin Bank (C and D). Increasing dark gray shading represents increasing loss of rays, black is at 10 percents loss
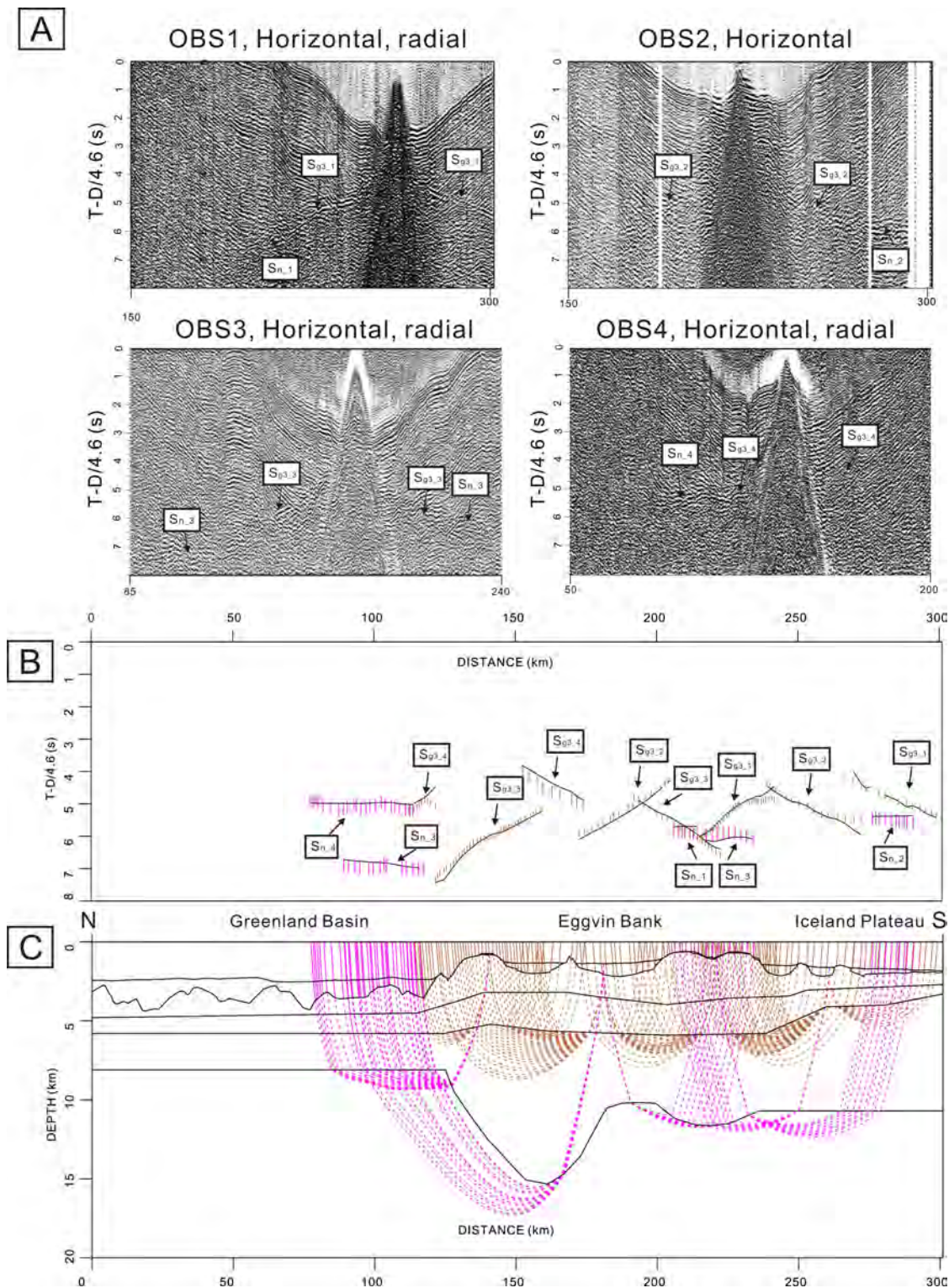
Figure 2.12: Horizontal, radial data (non-reoriented OBS2), PSS interpretation and ray tracing of OBS1 to OBS4. (a) Horizontal component data for OBS1-4 reduced by 4.6 km/s and phase identifications are shown on the recording section. (b) Comparison between calculated (black solid line) and interpreted traveltime (colored vertical bars). S_{g3_a}: S-wave in lower-crust in OBSa; S_{n_a}: S-wave in the upper mantle in OBSa (a is 1,2,3,4). (c) Ray tracing of the velocity model. The solid lines show P-wave paths, while the dashed lines represent the S-wave travel paths.

Table 2.2: Seismic model fit statistics for individual major phases (PSS-wave), and summary for all phases.

Phase	No. rays	RMS Δt (ms)	χ^2
S_{g3}	144	100	1.006
S_n	74	143	0.515
All phases	218	117	0.826

been identified from the horizontal components. PPS-waves propagate initially as P-waves and are converted into S-waves at an interface within the crust on the way up, whereas PSS-waves are converted on the way down, often at the seafloor or top basement. PSS phases give a direct estimate of the V_s in the crust, while PPS waves can give an indirect estimate in layers based on the delay time.

A velocity reduction of 8 km/s was applied to identify PPS-waves, while the identification of PSS waves is based on a velocity reduction of 4.6 km/s. The data from the latter are shown in Fig. 2.12a. The S wave modeling is based on the P-wave velocity model geometry. By assigning a poisson's ratio to each layer and determining the location of P-S conversion for each arrival, the S-wave velocity can be estimated (*Zelt and Ellis*, 1988; *Zelt and Smith*, 1992). The PSS arrival picks and modeled fit of all OBSs are shown in Fig. 2.12b-c. The PSS modeling has shown that all of the P-S conversions occurred at top basement. The model is constrained by S waves in the lower crust (S_{g3}) and in the upper mantle (S_n). The interpretation uncertainties of the S-wave arrivals from the lower crust and upper mantle are estimated to ±100 ms and ±200 ms respectively. PSS wave fit statistics are summarized in Tab. 2.2. The P and S wave velocity modeling results are used to generate a V_p/V_s ratio model (Fig. 2.13). The upper parts of the lower crust and the southern crustal root have the highest ray coverage density. The sediments in Eggvin Bank and Iceland Plateau have high V_p/V_s ratios (4.2 to 7.14) (constrained by PPS waves), which is interpreted as high porosity, uncompacted sediments (e.g. *Mjelde et al.*, 2003). Due to the presence of quartz, the V_p/V_s ratio of felsic crystalline rocks (1.71) is smaller than mafic crystalline rocks (1.84) (e.g. *Holbrook et al.*, 1992). The relatively high V_p/V_s ratios (1.82-1.88) for the crust indicate a mafic composition, and there is no obvious signature of continental crust extending from JMMC (*Campsie et al.*, 1990). This is consistent with the typical oceanic crust observed in the P wave velocity model and agrees with the proposed COB of both *Breivik et al.* (2012a) and *Peron-Pinvidic et al.* (2012a,b) (Fig. 2.2). The upper and middle crust have higher V_p/V_s ratios (1.87-1.88) than the lower crust (1.82-1.85). This difference is most likely due to a decreased fracture density with depth (*Mjelde et al.*, 2002). In the Eggvin Bank, the upper and middle crust have

similar V_p/V_s-ratios, while lower crust shows variations between different regions. The upper mantle V_p/V_s ratio increases under the northern crustal root, but the ray coverage is low there.

5 Discussion

5.1 The cause of excess magmatism

Wide angle refraction studies along other portions of the Kolbeinsey Ridge indicate a relatively smooth increase in crustal thickness towards Iceland (Fig. 2.14). Crustal thickness along the Southern Kolbeinsey Ridge (SKR) increase up to 13 km towards Iceland (*Hooft et al.*, 2006). The crustal thickness adjacent to the Middle Kolbeinsey Ridge (MKR) axis appears to be slightly more variable with an average of about 9-9.5 km (*Kodaira et al.*, 1997). Furthermore, the crust formed at the MKR shows no significant lateral variations in the igneous crustal thickness since 22 Ma (*Kodaira et al.*, 1998b). However, the crustal thickness of the Eggvin Bank shows large variations, from 8 km to 13 km. This thick crust is also in agreement with a recent 3D crustal model based on seismically constrained gravity inversion, where the crustal thickness over the Eggvin Bank is estimated to 10-15 km (*Haase et al.*, 2016). In contrast to the Eggvin Bank, the southern transects show little lower-crustal velocity variation. The northern Eggvin Bank has 0.2 km/s higher lower-crustal velocity and 3 km thicker crust compared with southern Eggvin Bank (190-220 km) (Fig. 2.9). While there is some uncertainty to how pronounced this difference is, it could indicate changes in magmatic processes and how these affect total magma production and composition along profile. Both mantle composition and mantle melting degree will be important in that respect. A high melt degree caused by high mantle temperature results in melts with high MgO content relative the FeO content, yielding thick, high-velocity igneous crust (e.g. *White*, 1989; *Kelemen and Holbrook*, 1995; *Korenaga et al.*, 2002; *Sallarès et al.*, 2005). If the crust is created on-axis over a hot mantle plume, there will be a positive correlation between the crustal thickness and seismic velocity (*Holbrook et al.*, 2001). High mantle upwelling rates (active upwelling relative to passive upwelling driven by seafloor spreading) leads to increased mantle volumes circulating through the melting zone. For a constant mantle temperature this will yield thicker oceanic crust with little change in seismic velocity as thickness changes (*Holbrook et al.*, 2001; *White et al.*, 2008). On the other hand, if crustal thickness variations were only caused by the presence of a fertile mantle component in the melting zone, this would result in a negative correlation
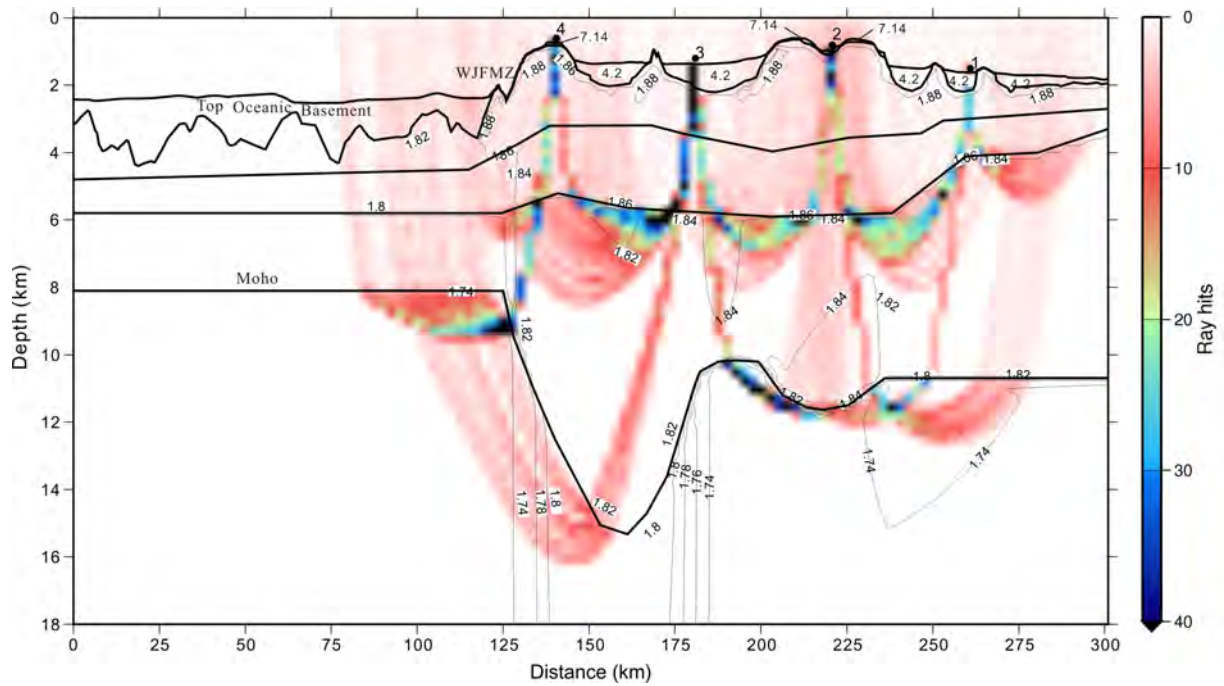
Figure 2.13: Contoured Vp/Vs-ratios based on Vp and Vs velocity modeling. The background picture shows the Vs gridded ray coverage (2.5 by 0.25 km distance depth grid).
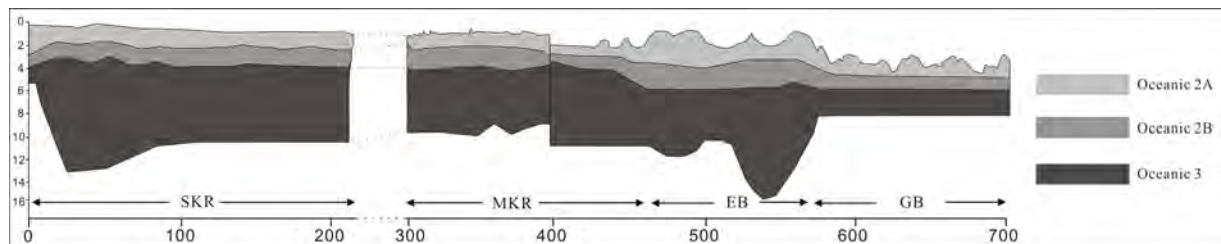
Figure 2.14: Combined transect from SKR to Eggvin Bank. The location is shown in Fig. 2.1. The crustal profile of SKR and MKR are derived from *Hooft et al.* (2006) and *Kodaira et al.* (1997), respectively. The Eggvin Bank is from this study. The Eggvin Bank profile is on older crust, and therefore deeper. The layers from top to bottom are oceanic 2A, oceanic 2B, and oceanic 3. SKR: South Kolbeinsey Ridge, MKR: Middle Kolbeinsey Ridge, EB: Eggvin Bank, GB: Greenland Basin.

between crustal thickness and seismic velocity (e.g. *Korenaga et al.*, 2002; *Sallarès et al.*, 2005). These three end-member models are valid for a single melt event, such as at a seafloor spreading axis. If a thick crust is created by multiple, low-degree melting events, FeO would most likely be high, and the velocity would be lower and resemble the result of active upwelling or of an extra fertile mantle.

5.2 H-V_p analysis

The connection between the seismic properties that can be measured in igneous crust and the underlying mantle melting processes can be estimated based on the correlation between seismic velocity and crustal thickness (H-V_p analysis) (e.g. *Holbrook et al.*, 2001). The average velocity of upper and middle crustal layers (Layer 2) is strongly influenced by fissures and cracks (*Wilkens et al.*, 1991; *Jacobson*, 1992). The lower crust (Layer 3) is dominated by unaltered, low porosity gabbroic rocks, where velocity is mainly controlled by compositional variations.

We have used the pressure corrections from *Holbrook et al.* (2001) to calculate the average lower-crustal velocities (Fig. 2.15). For the temperature correction, we assume 10 °C at the seafloor with 520 °C fixed at 20 km depth and a linear gradient (*Tan et al.*, 2016). Following *Holbrook et al.* (2001), we assigned all crustal velocities below 6.85 km/s to the value of 6.85 km/s to eliminate the effect of porosity.

5.3 H-V_p results

The relationship between average lower-crustal velocities and total crustal thickness is shown in Fig. 2.15. Based on the best fit model, the northern Eggvin Bank has a positive H-V_p correlation, while the southern Eggvin Bank shows a poor H-V_p correlation. In the northern Eggvin Bank, the crustal thickness increase from 8 km to 13 km associated with a V_p increase of 0.1 km/s to just above 7.0 km/s. The southern Eggvin Bank, however, has a low velocity (around 6.85 km/s for crustal thickness exceeding 10 km), where the V_p remains almost unchanged over crustal thickness variations of 8 km to 11 km.

Based on the sensitivity analysis (Fig. 2.11), the minimum (the shallowest Moho and lowest lower-crustal velocity) and maximum velocity models (the deepest Moho and highest lower-crustal velocity) show large variations of the H-V_p correlations (Fig. 2.15B). The northern Eggvin Bank maximum velocity model shows a positive H-V_p correlation with larger crustal thickness and high lower-crustal V_p. However, the minimum velocity model has a more horizontal H-V_p pattern, similar to southern Eggvin Bank. These different
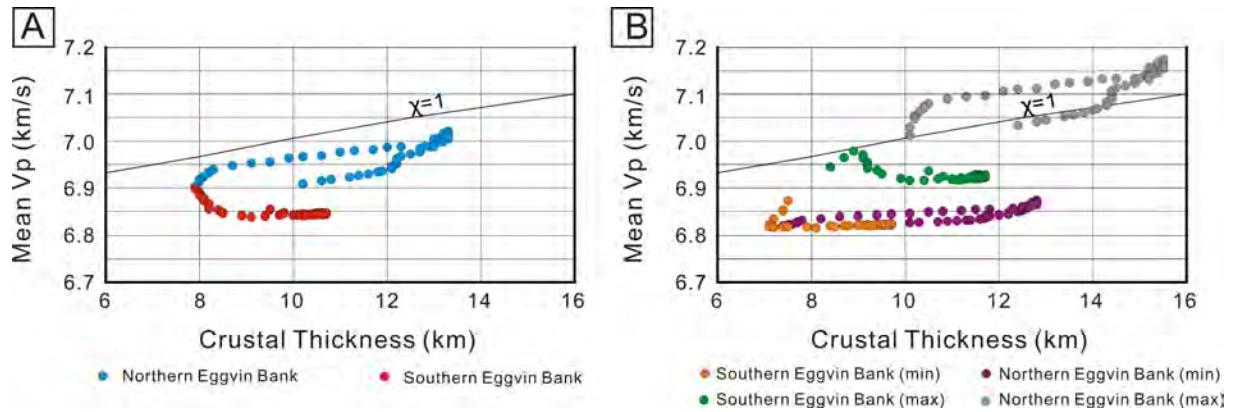
Figure 2.15: Crustal thickness versus mean V_p for the Eggvin Bank. Sampling interval is 1 km horizontally. (A). The northern Eggvin Bank comprises the region from 135 km-190 km, while the southern Eggvin Bank is the region from 190 km-220 km. $\chi{=}1$ shows passive decompression melting of normal mantle with increasing temperature (*McKenzie and Bickle*, 1988). The pressure corrections used by *Holbrook et al.* (2001), while the temperature correction assume a linear gradient from 10 °C at the seafloor to 520 °C at 20 km depth (*Tan et al.*, 2016). (B) Minimum and maximum velocity models indicated by the sensitivity analysis (Fig. 2.11).

H-V_p patterns would require different mantle melting processes. We prefer the positive H-V_p correlation in the northern Eggvin Bank, but a horizontal H-V_p pattern can not be completely ruled out. Both the maximum and minimum velocity models of the southern Eggvin Bank have a poor H-V_p correlation with low average V_p.

If real, the positive H-V_p correlation for the northern Eggvin Bank (Fig. 2.15a) may have two alternative explanations. If the entire crustal section was created at the spreading center, it would represent a single melting event governed by elevated mantle temperature. However, another scenario involving additional off-axis melting could still result in a positive H-V_p correlation. If one of the major melting episodes are driven by excess temperature, the next episode would not necessarily overprint the positive H-V_p correlation. If that happened, most likely the primary oceanic crust formed at the spreading center (on-axis event) should have high Mg/Fe ratios (high degrees of melting) and the secondary addition to the igneous crust may results from relatively lower degrees of melting, which is expected since the thicker lithosphere will result in a shorter melt-extraction column and the residual asthenosphere has become more refractory.

A poor H-V_p correlation of the southern Eggvin Bank indicate that the lower-crustal composition changes little with crustal thickness variations (e.g. *White*, 1989). If all crust was formed on-axis, that would require active upwelling with low-degree melting and/or

enriched components to explain excess crustal thickness. However, multiple melting events with crustal off-axis additions generated by relatively low degree of partial melting could also result in basalts with low Mg/Fe ratio and a poor H-V_p correlation (e.g. *Yaxley*, 2000; *Korenaga et al.*, 2002). To what degree this also applies to the north is uncertain, but it could be noted that both curves are low in the diagram, consistent with multiple melting events.

The Layer 2 thickness of SKR and MKR is uniformly 3.5 km thick (Fig. 2.14). Along the Eggvin Bank, Layer 2 is slightly thicker (4.2 ± 0.5 km), whereas Layer 3 is considerably more variable and thicker (4.5-9.5 km). Clearly, there has been significantly more of extrusive magmatism at the Eggvin Bank creating the seamounts. Normal oceanic crust, which is formed at a sea-floor spreading axis through a single melting event, has generally a uniform proportion of Layer 2 to total crustal thickness of around 25%, so that most of the crustal thickening is accommodated by Layer 3 (*Korenaga et al.*, 2000; *Sallarès et al.*, 2003; *Hampel et al.*, 2004; *Sallarès et al.*, 2005). However, the proportion of Layer 2 for off-axis crust, created by multiple melting events, is mostly around 50% (*Watts and Ten Brink*, 1989; *Caress et al.*, 1995; *Charvis et al.*, 1999; *Ye et al.*, 1999; *Canales et al.*, 2000). Along the Eggvin Bank profile, the average ratio of Layer 2 thickness versus total crustal thickness is 0.36 in the northern region, while it is 0.46 in southern region (Fig. 2.8). Minimum and maximum models give ratios of 0.29 to 0.39 in the north. In the south it varies from 0.44 to 0.52. The high ratio both in the north and the south indicates that the formation of the seamounts is probably not at the spreading center. The northern seamount has a flat top (730 m deep), which indicates that it has been eroded above or near sea level; while in the south the profile crosses the summit of the shallowest one, which has a rounded top of 460 m depth, even if the crust is 3-4 Ma older. The southernmost seamount has a depth of 550 m on the profile, but it is located slightly to the side of the summit. These observations suggest that the southern seamounts are younger, since they are shallower but without obvious signs that they were subaerially exposed. This indicates that the southern but possibly also the northern Eggvin Bank is created by multiple melting events on and off-axis, and that the southern Eggvin Bank seamounts have a younger formation age than the northern seamount.

5.4 Upper mantle velocities

The anomalously low V_p (7.7 km/s) as well as relatively high Vp/Vs-ratios (1.8) in the upper mantle observed in the northern region (140 km-170 km) (Figs. 2.8, 2.13) could represent partial serpentinization of mantle material (e.g. *Bown and White*, 1995; *Mjelde*

et al., 2002; *Fujie et al.*, 2013). If the mantle serpentinization is due to the influence of WJMFZ, it is most likely to occur along the fracture zone. However, the relatively high V_p (8.01 km/s) and lower V_p/V_s-ratios (1.73) in the mantle under the WJMFZ indicate that the anomalous V_p and V_p/V_s-ratio in the upper mantle south of it are due to other factors. Lower velocities in the upper mantle could also be interpreted as melt retention in the upper mantle (e.g. *Cannat*, 1996). Based on mineralogical studies, *Haase et al.* (2003) pointed out that the WJMFZ could cool the ascending magmas by up to 100 °C compared to southern NKR. This could have increased the effect of conductive cooling and made melt extraction less effective, with more melt solidified in the upper mantle (e.g. *Lizarralde et al.*, 2004). The elevated V_p/V_s ratio in the uppermost mantle (Fig. 2.13) supports melt retention, since gabbro has a higher ratio than peridotite (*Christensen*, 1996).

5.5 Geochemistry of the Eggvin Bank

None of the seamounts along Profile 1 have been sampled, although several studies have sampled younger seamounts nearby as well as the seafloor spreading axis (Fig. 2.2). The dredged samples from NKR, near-axis, and off-axis seamounts at the Eggvin Bank are enriched in incompatible elements (*Campsie et al.*, 1990; *Mertz et al.*, 2004; *Elkins et al.*, 2011, 2016). This indicates elevated proportions of enriched source components under the NKR and surrounding Eggvin Bank at the present, and probably also in the past. The NKR basalts are isotopically similar to basalts from sources with recycled oceanic crust, erupted in the Southern Flank Zone and on the Reykjanes Peninsula in Iceland (e.g. *Mertz et al.*, 2004; *Debaille et al.*, 2009; *Trønnes et al.*, 2013), whereas the off-axis Eggvin Bank basalts are compositionally intermediate between basalts from the Jan Mayen area and the NKR. An enriched mantle source appears to be the main reason for the anomalous magmatism at the Eggvin Bank, and may also determine the location of the spreading ridge offset from the MKR. Source variations could have produced differences in the magmatism between northern and southern parts of the Eggvin Bank in the past. The southern part should be dominated by an enriched mantle source, since the crust was likely formed by multiple melting events with lower mantle-melting degrees. However, the northern part shows signs of mantle melting driven by elevated temperature, where the enriched mantle source may have played a lesser role.

The northeast Atlantic region has been significantly influenced by the Iceland plume to varying degrees since the time of continental break-up (e.g. *Hooft et al.*, 2006; *Howell et al.*, 2014). Isotopic constrains, thermal anomalies and V-shaped ridges suggest that the

Iceland plume affects the entire length of the Kolbeinsey Ridge (*Poreda et al.*, 1986; *Jones et al.*, 2002; *Pilidou et al.*, 2005). As demonstrated by *Mertz et al.* (2004), dispersion of enriched material from a putative Jan Mayen plume cannot explain the radiogenic Nd-Pb isotope compositions of basalts from the Eggvin Bank and the NKR. These basalt compositions, however, are consistent with sources emplaced by deep-level northward flow of Iceland plume material, ascending into the melting zone south of the WJMFZ.

6 Summary and Conclusions

The crustal structure of the Eggvin Bank has been investigated from refraction/reflection data along one seismic profile. Results from P wave traveltime modeling show oceanic crustal velocities, with a low-velocity upper crust (2.8 km/s to 4.8 km/s), a middle crust (5.5 km/s to 6.5 km/s), and a low-gradient, high-velocity lower crust (6.7 km/s to 7.35 km/s). These typical oceanic crustal velocities and relatively high crustal V_p/V_s-ratios (1.82-1.88) indicate a mafic composition and are inconsistent with continental crust extending from the JMMC to the Eggvin Bank. However, the anomalously thick crust and the morphology of the Eggvin Bank differ from typical oceanic crust at the Kolbeinsey Ridge to the south. The crust has large variations in thickness, from 8 km to 13 km, where a 2-5 km increase is associated with two 20-30 km wide segments under the main seamounts.

Based on the increase of the layer 2 thickness and the high ratio of layer 2 thickness to total crustal thickness, we infer that secondary, intraplate magmatism probably played an important role in building the seamounts of the Eggvin Bank. The flat top of the seamount in the north indicates subaerial exposure despite being deeper, and is therefore probably older than the shallower seamounts with rounded tops in the south.

We correlate lower-crust seismic velocity (V_p) and crustal thickness (H) in order to estimate the formation mechanisms in the Eggvin Bank. Along Profile-1, the northern Eggvin Bank tends toward a positive H-V_p correlation, though there is some uncertainty to this result. This indicates that the northern Eggvin Bank could be created by higher degree of mantle melting driven by elevated temperature. The southern Eggvin Bank is characterized by an overall poor H-V_p correlation and low V_p in the lower-crust, which is compatible with multiple melting events with low mantle-melting degree. An enriched mantle source presently feeds the NKR magmatism, which may have influenced the development of the Eggvin Bank also at earlier times, being an important source for the off-axis magmatism. To what extent the Eggvin Bank has been influenced by the Iceland

plume is uncertain, both an enriched mantle component and elevated mantle temperature may have played a role in its development at different times and locations.

References

Bown, J. W., and R. S. White (1995), Effect of finite extension rate of melt generation at rifted continental marins, *J. Geophys. Res.*, *100*, 18,011–18,029.

Breivik, A., R. Mjelde, J. I. Faleide, E. Flueh, and Y. Murai (2014), Magmatic development of the outer Vøring margin from seismic data, *J. Geophys. Res.*, *119*, 6733–6755, doi:10.1002/2014JB011040.

Breivik, A. J., R. Mjelde, P. Grogan, H. Shimamura, Y. Murai, and Y. Nishimura (2003), Crustal structure and transform margin development south of Svalbard based on ocean bottom seismometer data, *Tectonophysics*, *369*, 37–70.

Breivik, A. J., R. Mjelde, J. I. Faleide, and Y. Murai (2012), The eastern Jan Mayen microcontinent volcanic margin, *Geophys. J. Int.*, *188*, 798–818, doi:10.1111/j.1365-246X.2011.05307.x.

Campsie, J., M. H. Rasmussen, L. C. Kovacs, F. Dittmer, J. C. Bailey, N. O. Hansen, and L. Johnson (1990), Chronology and evolution of the northern Iceland Plateau, *Polar Research*, *8*(2), 237–243.

Canales, J. P., J. J. Danobeitia, and A. B. Watts (2000), Wide-angle seismic constraints on the internal structure of Tenerife, Canary Islands, *J. Volcanol. Geotherm. Res.*, *103*, 65–81.

Cannat, M. (1996), How thick is the magmatic crust at slow spreading oceanic ridges?, *J. Geophys. Res.*, *101*, 2847–2857.

Caress, D. W., M. K. McNutt, R. S. Detrick, and J. Mutter (1995), Seismic imaging of hotspot-related crustal underplating beneath the Marquesas Islands, *Nature*, *373*, 600–603.

Charvis, P., A. Laesanpure, J. Gallart, A. Hirn, J. C. Lepine, B. de Voogd, Y. Hello, B. Pontoise, and T. A. Minshull (1999), Spatial distribution of hot spot material added

References

to the lithosphere under La Reunion, from wide-angle seismic data, *J. Geophys. Res.*, *104*, 2875–2893.

Christensen, N. I. (1996), Poisson's ratio and crustal seismology, *J. Geophys. Res.*, *101*(B2), 3139–3156.

Christeson, G., G. Purdy, and G. Fryer (1994), Seismic constrains on shallow crustal emplacement processes at the fast spreading East Pacific Rise, *J. Geophys. Res.*, *99*, 17,957–17,974.

Debaille, V., R. G. Trønnes, A. D. Brandon, T. E. Waight, D. W. Graham, and C. A. Lee (2009), Primitive off-rift basalts from Iceland and Jan Mayen: Os-isotopic evidence for a mantle source containing enriched subcontinental lithosphere, *Geochim. Cosmochim. Acta.*, *73*, 3423–3449.

Detrick, R., J. Collins, R. Stephen, and S. Swift (1994), In situ evidence for the nature of the seismic layer 2/3 boundary in oceanic crust, *Nature, 370*, 288–290.

Dilek, Y. (1998), Structure and tectonics of intermediate-spread oceanic crust drilled at DSDP/ODP holes 504B and 896A, Costa Rica Rift, in Geolocial Evolution of Ocean Basin: Results From the Ocean Drilling Program, edited by A. Cramp et al., *Geol. Soc. Spec. Publ., 131*, 179–197.

Eldholm, O., and K. Grue (1994), North Atlantic volcanic margins: Dimensions and production rates, *J. Geophys. Res.*, *99*(B2), 2955–2968.

Elkins, L. J., K. W. W. Sims, J. Prytulak, T. Elliott, N. Mattielli, J. Blichert-Toft, J. Blusztajn, N. Dunbar, C. Devey, D. F. Mertz, J. G. Schilling, and M. Murrell (2011), Understanding melt generation beneath the slow-spreading Kolbeinsey Ridge using ^{238}U, ^{230}Th, and ^{231}Pa excesses, *Geochim. Cosmochim. Acta.*, *75*, 6300–6329.

Elkins, L. J., E. R. Rivers, K. W. W. Sims, J. Blichert-Toft, C. Devey, R. Chernow, R. Davis, and K. Meisenhelder (2013), Origins of anomalous ridge magmatism near Jan Mayen, *Mineral Mag.*, *77*(5), 1035.

Elkins, L. J., C. Hamelin, J. Blichert-Toft, S. R. Scott, K. W. W. Sims, I. A. Yeo, C. W. Devey, and R. B. Pedersen (2016), North Atlantic hotspot-ridge interaction near Jan Mayen Island, *Geochem. Persp. Lett.*, *2*, 55–67.

Engen, Ø., J. I. Faleide, and T. Karlberg Dyreng (2008), Opening of the Fram Strait gateway: A review of plate tectonic constraints, *Tectonophysics*, *450*, 51–69, doi:10.1016/j.tecto.2008.01.002.

Evans, J. R., and I. S. Sacks (1979), Deep structure of the Iceland Plateau, *J. Geophys. Res.*, *84*, 6859–6866.

Fujie, G., S. Kodaira, M. Yamashita, T. Sato, and N. Takahashi, T.and Takahashi (2013), Systematic changes in the incoming plate structure at the Kuril trench, *Geophys. Res. Lett.*, *40*(1), 88–93.

Funck, T., W. H. Geissler, G. S. Kimbell, S. Gradmann, M. K. Erlendsson, Ö, and U. K. Petersen (2016), Moho and basement depth in the NE Atlantic Ocean based on seismic refraction data and receiver functions, *Geol. Soc. Spec. Pub.*, *477*, doi:10.1144/SP447.1.

Gaina, C., L. Gernigon, and P. Ball (2009), Palaeocene–Recent plate boundaries in the NE Atlantic and the formation of the Jan Mayen microcontinent, *J. Geol. Soc.*, *166*, 601–616, doi:10.1144/0016-76492008-112.

Gernigon, L., O. Olesen, J. Ebbing, S. Wienecke, C. Gaina, J. Mogaard, M. Sand, and R. Myklebust (2008), Geophyical insights and early spreading history in the vicinity of the Jan Mayen Fracture Zone, Norwegian-Greenland sea, *Tectonophysics*, *468*, 185–205.

Haase, C., J. Ebbing, and T. Funck (2016), A 3D crustal model of the NE Atlantic based on seismic and gravity data, *Geol. Soc. Spec. Pub.*, *447*.

Haase, K. M., C. W. Devey, and M. Wieneke (2003), Magmatic processes and mantle heterogeneity beneath the slow-spreading northern Kolbeinsey Ridge segment, North Atlantic, *Contrib. Mineral. Petrol.*, *144*, 428–448.

Hampel, A., N. Kukowski, J. Bialas, C. Huebscher, and R. Heinbockel (2004), Ridge subduction at an erosive margin-the collision zone of the Nazca Ridge in southern Peru, *J. Geophys. Res.*, *109*, B02,101, doi:10.1029/2003JB002593.

Havskov, J., and K. Atakan (1991), Seismicity and volcanism of Jan Mayen Island, *Terra Nova*, *3*(5), 517–526.

Holbrook, W. S., W. D. Mooney, and N. I. Christensen (1992), The seismic structure of the deep continental crust, in *Continental lower crust*, edited by D. M. Fountain, R. Arculus, and R. W. Kay, pp. 1–43, Elsevier, Amsterdam.

References

Holbrook, W. S., H. C. Larsen, J. Korenaga, T. Dahl-Jensen, I. D. Reid, P. B. Kelemen, J. R. Hopper, G. M. Kent, D. Lizarralde, S. Bernstein, and R. S. Detrick (2001), Mantle thermal structure and active upwelling during continental breakup in the North Atlantic, *Earth Planet. Sci. Lett.*, *190*, 251–266.

Hooft, E. E. E., R. S. Detrick, D. R. Toomey, J. A. Collins, and J. Lin (2000), Crustal thickness and structure along three contrasting spreading segments of the Mid-Atlantic Ridge, 33.5°-35°N, *J. Geophys. Res.*, *105*(B4), 8205–8226.

Hooft, E. E. E., B. Brandsdóttir, R. Mjelde, H. Shimamura, and Y. Murai (2006), Asymmetric plume ridge interaction around Iceland: The Kolbeinsey Ridge Iceland Seismic Experiment, *Geochem. Geophys. Geosyst.*, *7*(5), 1–26.

Howell, S. M., G. Ito, A. J. Breivik, A. Rai, R. Mjelde, B. Hanan, K. Sayit, and P. Vogt (2014), The origin of the asymmetry in the Iceland hotspot along the Mid-Atlantic Ridge from continental breakup to present-day, *Earth Planet. Sci. Lett.*, *392*, 143–153.

Imsland, P. (1986), The volcanic eruption on Jan Mayen, January 1985: Interaction between a volcanic island and a fracture zone, *J. Volcanol. Geoth. Res.*, *28*, 45–53.

Jacobson, R. S. (1992), Impact of crustal evolution on changes of the seismic properties of the uppermost oceanic crust, *Rev. Geophys.*, *30*(1), 23–42.

Jakobsson, M., L. A. Mayer, B. Coakley, J. A. Dowdeswell, S. Forbes, B. Fridman, H. Hodnesdal, R. Noormets, R. Pedersen, M. Rebesco, H.-W. Schenke, Y. Zarayskaya, A. D. Accettella, A. Armstrong, R. M. Anderson, P. Bienhoff, A. Camerlenghi, I. Church, M. Edwards, J. V. Gardner, J. K. Hall, B. Hell, O. B. Hestvik, Y. Kristoffersen, C. Marcussen, R. Mohammad, D. Mosher, S. V. Nghiem, M. T. Pedrosa, P. G. Travaglini, and P. Weatherall (2012), International Bathymetric Chart of the Arctic Ocean (IBCAO) Version 3.0, *Geophys. Res. Lett.*, *39*(L12609), doi:10.1029/2012GL052219.

Jones, S. M., N. White, and J. Maclennan (2002), V-shaped ridges around Iceland: Implications for spatial and temporal patterns of mantle convection, *Geochem. Geophys. Geosyst.*, *3*(10), 1059, doi:10.1029/2002GC000361.

Kandilarov, A., R. Mjelde, R. B. Pedersen, B. Hellevang, C. Papenberg, C. J. Petersen, L. Planert, and E. Flueh (2012), The northern boundary of the Jan Mayen Microcontinent, North Atlantic determined from ocean bottom seismic, multichannel seismic, and gravity data, *Mar. Geophys. Res.*, *33*(1), 55–76.

Kandilarov, A., R. Mjelde, E. Flueh, and R. B. Pedersen (2015), V_p/V_s-ratios and anisotropy on the northern Jan Mayen Ridge, North Atlantic, determined from ocean bottom seismic data, *Polar Sci.*, *9*(3), 293–310.

Kelemen, P. B., and W. S. Holbrook (1995), Origin of thick, high-velocity, igneous crust along the U.S. East Coast Margin, *J. Geophys. Res.*, *100*(B7), 10,077–10,094.

Klingelhöfer, F., L. Géli, and R. S. White (2000), Geophysical and geochemical constraints on crustal accretion at the very-slow spreading Mohns Ridge, *Geophys. Res. Lett.*, *27*(10), 1547–1550.

Kodaira, S., R. Mjelde, H. Shimamura, K. Gunnarsson, and H. Shiobara (1997), Crustal structure of the Kolbeinsey Ridge, N. Atlantic, obtained by use of Ocean Bottom Seismographs, *J. Geophys. Res.*, *102*(B2), 3131–3151.

Kodaira, S., R. Mjelde, K. Gunnarsson, H. Shiobara, and H. Shimamura (1998a), Structure of the Jan Mayen microcontinent and implication for its evolution, *Geophys. J. Int.*, *132*, 383–400.

Kodaira, S., R. Mjelde, K. Gunnarsson, H. Shiobara, and H. Shimamura (1998b), Evolution of oceanic crust on the Kolbeinsey Ridge, north of Iceland, over the past 22 Myr, *Terra Nova*, *10*, 27–31.

Korenaga, J., W. S. Holbrook, G. M. Kent, P. B. Kelemen, R. S. Detrick, H. C. Larsen, J. R. Hopper, and T. Dahl-Jensen (2000), Crustal structure of the southeast Greenland margin from joint refraction and reflection seismic tomography, *J. Geophys. Res.*, *105*, 21,591–21,614.

Korenaga, J., P. B. Kelemen, and W. S. Holbrook (2002), Methods for resolving the origin of large igneous provinces from crustal seismology, *J. Geophys. Res.*, *107*(B9), 2178, doi:10.1029/2001JB001030.

Lizarralde, D., J. B. Gaherty, J. A. Collins, G. Hirth, and S. D. Kim (2004), Spreading-rate dependence of melt extraction at mid-ocean ridges from mantle seismic data, *Nature*, *432*, 744–747, doi:10.1038/nature03140.

Ljones, F., A. Kuwano, R. Mjelde, A. J. Breivik, H. Shimamura, Y. Murai, and Y. Nishimura (2004), Crustal transect from the North Atlantic Knipovich Ridge to the Svalbard margin west of Hornsund, *Tectonophyics*, *378*, 17–41.

References

Maercklin, N. (2007), Supolar and supofilt: Su programs for polarization analysis and filtering of three-component data., doi:10.13140/2.1.1697.7926.

Maus, S., T. Sazonova, K. Hemant, J. D. Fairhead, and D. Ravat (2007), National geophysical data center candidate for the world digital magnetic anomaly map, *Geochem. Geophys. Geosyst.*, *8*(6).

McKenzie, D., and M. J. Bickle (1988), The volume and composition of melt generated by extension of the lithosphere, *J. Petrol.*, *29*(3), 625–679.

Menke, W., M. West, B. Brandsdóttir, and B. Sparks (1998), Compressional and shear velocity structure of the lithosphere in northern Iceland, *Bull. Seismol. Soc. Am.*, *88*, 1561–1571.

Mertz, D. F., W. D. Sharp, and K. M. Haase (2004), Volcanism on the Eggvin Bank (Central Norwegian-Greenland Sea, latitude ∼71°N): age, source, and relationship to the Iceland and putative Jan Mayen plumes, *J. Geodyn.*, *38*, 57–83, doi:10.1016/j.jog.2004.03.003.

Mjelde, R., R. Aurvåg, S. Kodaira, H. Shimamura, K. Gunnarsson, A. Nakanishi, and H. Shiobara (2002), Vp/Vs-ratios from the central Kolbeinsey Ridge to the Jan Mayen Basin, North Atlantic; implications for lithology, porosity and present-day stress field, *Mar. Geophys. Res.*, *23*(2), 123–145.

Mjelde, R., T. Raum, P. Digranes, H. Shimamura, H. Shiobara, and S. Kodaira (2003), Vp/Vs-ratio along the Vøring margin, NE Atlantic, derived from OBS-data: implications on lithology and stress-field, *Tectonophysics*, *369*, 175–197.

Mjelde, R., I. Eckhoff, S. Solbakken, S. Kodaira, H. Shimamura, K. Gunnarsson, A. Nakanishi, and H. Shiobara (2007), Gravity and S-wave modeling across the Jan Mayen Ridge, North Atlantic; implications for crustal lithology and continental breakup processes, *Mar. Geophys. Res.*, *28*, 27–41, doi:10.1007/s11001-006-9012-3.

Morgan, W. (1983), Hotspot tracks and the early rifting of the Atlantic, *Tectonophysics*, *94*, 123–139.

Mosar, J., G. Lewis, and T. H. Torsvik (2002), North Atlantic sea-floor spreading rates: implications of the Tertiary development of inversion structures of the Norwegian-Greenland Sea, *J. Geol. Soc.*, *159*, 503–515.

National Geophysical Data Center (2006), 2-minute gridded global relief data (ETOPO2) v2. National Geophysical Data Center, NOAA, doi:10.7289/V5J1012Q.

Noble, R. H., R. M. Macintyre, and P. E. Brown (1988), Age constraints on Atlantic evolution: timing of magmatic activity along the E Greenland continental margin, *Geol. Soc. Spec. Publ.*, *39*, 201–214, doi:10.1144/GSL.SP.1988.039.01.19.

Peron-Pinvidic, G., L. Gernigon, C. Gaina, and P. Ball (2012a), Insights from the Jan Mayen system in the Norwegian-Greenland sea-I. Mapping of a microcontinent, *Geophys. J. Int.*, *191*, 385–412.

Peron-Pinvidic, G., L. Gernigon, C. Gaina, and P. Ball (2012b), Insights from the Jan Mayen system in the Norwegian-Greenland sea-II. Architecture of a microcontinent, *Geophys. J. Int.*, *191*, 413–435.

Pilidou, S., K. Priestley, E. Debayle, and O. Gudmundsson. (2005), Rayleigh wave tomography in the North Atlantic: high resolution images of the Iceland, Azores and Eifel mantle plumes, *Lithos.*, *79*, 453–474.

Poreda, R., J. G. Schilling, and H. Craig (1986), Helium and hydrogen isotopes in ocean-ridge basalts north and south of Iceland, *Earth Planet. Sci. Lett.*, *78*, 1–17.

Sallarès, V., P. Charvis, E. R. Flueh, and J. Bialas (2003), Seismic structure of Cocos and Malpelo Volcanic Ridges and implications for hot spot-ridge interaction, *J. Geophys. Res.*, *108*(B12), 2564, doi:10.1029/2003JB002431.

Sallarès, V., P. Charvis, E. R. Flueh, J. Bialas, and the SALIERI Scientific Party (2005), Seismic structure of the Carnegie ridge and the nature of the Galápagos hotspot, *Geophys. J. Int.*, *161*, 763–788, doi:10.1111/j.1365-246X.2005.02592.x.

Schilling, J., M. Zajac, R. Evans, T. Johnston, W. White, J. Devine, and R. Kingsley (1983), Petrologic and geochemical variations along the Mid-Atlantic ridge from 29°N to 73°N, *Am. J. Sci.*, *283*, 510–586.

Sørnes, A., and T. Navrestad (1975), Seismic survey about Jan Mayen, *Norsk Polarinst. Årbok*, pp. 37–52.

Talwani, M., and O. Eldholm (1977), Evolution of the Norwegian–Greenland Sea, *Geol. Soc. Am. Bull.*, *88*, 969–999.

References

Tan, P., J. Sippel, A. J. Breivik, M. Scheck-Wenderoth, and C. Meeßen (2016), Crustal and mantle structure of the greater Jan Mayen-East Greenland region (NE Atlantic) from combined 3D structural, S-wave velocity and gravity modeling, in *Eos Trans. AGU*, Fall Meet. Suppl., Abstract T43B-3034.

Thiede, J., and G. Hempel (1991), Die Expedition ARKTIS-VII/1 mit FS "Polarstern", *Rep. Polar. Res.*, pp. 1–137.

Trønnes, R. G., S. Planke, B. Sundvoll, and P. Imsland (1999), Recent volcanic rocks from Jan Mayen: Low-degree melt fractions of enriched northeast Atlantic mantle, *J. Geophys. Res.*, *104*(B4), 7153–7168.

Trønnes, R. G., V. Debaille, M. Erambert, F. M. Stuart, and T. Waight (2013), Mixing and progressive melting of deep and shallow mantle sources in the NE Atlantic and Arctic, *Mineral. Mag.*, *77*, 2357.

Vogt, P. R., G. L. Johnson, and L. Kristjansson (1980), Morphology and magnetic anomalies north of Iceland, *J. Geophys.*, *47*, 67–80.

Voss, M., and W. Jokat (2007), Continent-ocean transition and voluminous magmatic underplating derived from P-wave velocity of the East Greenland continental margin, *Geophys. J. Int.*, *170*, 580–604, doi:10.1111/j.1365-246X.2007.03438.x.

Voss, M., M. C. Schmidt-Aursch, and W. Jokat (2009), Variations in magmatic processes along the East Greenland volcanic margin, *Geophys. J. Int.*, *177*, 755–782.

Watts, A. B., and U. S. Ten Brink (1989), Crustal structure, flexure, and subsidence history of the Hawaiian Islands, *J. Geophys. Res.*, *94*, 10,473–10,500.

White, R. S. (1989), Initiation of the Iceland Plume and opening of the North Atlantic, in *Extensional tectonics and stratigraphy of the North Atlantic margins*, edited by A. J. Tankard and H. R. Balkwill, pp. 149–154, AAPG Mem., 46, Tulsa, Oklahoma.

White, R. S., D. McKenzie, and K. O'Nions (1992), Oceanic crustal thickness from seismic measurements and rare earth element inversion, *J. Geophys. Res.*, *97*(B13), 19,683–19,715.

White, R. S., L. K. Smith, A. W. Roberts, P. A. F. Christie, N. J. Kusznir, and iSIMM Team (2008), Lower-crustal intrusion on the North Atlantic continental margin, *Nature*, *452*, 460–464, doi:10.1038/nature06687.

Wilkens, R. H., G. J. Fryer, and J. Karsten (1991), Evolution of porosity and seismic structure of upper oceanic crust: Importance of aspect ratios, *J. Geophys. Res.*, *96*(B11), 17,981–17,995.

Yaxley, G. M. (2000), Experimental study of the phase and melting relations of homogeneous basalt + peridotite mixures and implications for the petrogenesis of flood basalts, *Contib. Mineral. Petr.*, *139*, 326–338.

Ye, S., J. P. Canales, R. Rihm, J. J. Danobeitia, and J. Gallart (1999), A crustal transect through the northern and northeastern part of the volcanic edifice of Gran Canaria, Canary Islands, *J. Geodyn.*, *28*, 3–26.

Yeo, I. A., N. Augustin, C. W. Devey, M. Deutschmann, L. J. Elkins, T. Laurila, K. Meisenhelder, E. Rivers, M. Rothenbeck, and F. M. van der Zwan (2012), The Northern Kolbeinsey Ridge, North Atlantic: Excess volcanism and ridge relocations close to Jan Mayen, *Eos Trans. AGU*, *1*, 1734, Fall Meet. Suppl., Abstract #OS13B-1734.

Yeo, I. A., T. P. Lebas, N. Augustin, and A. Steinführer (2016), Segment-scale volcanic episodicity: Evidence from the North Kolbeinsey Ridge, Atlantic, *Earth Planet. Sci. Lett.*, *439*, 81–87.

Zelt, C. A., and R. M. Ellis (1988), Practical and efficient ray tracing in two-dimensional media for rapid traveltime and amplitude forward modelling, *Can. J. Explor. Geophys.*, *24*, 16–31.

Zelt, C. A., and R. B. Smith (1992), Seismic traveltime inversion for 2-D crustal velocity structure, *Geophys. J. Int.*, *108*, 16–34.

Paper 3. Lithospheric control on asthenospheric flow from the Iceland plume: 3D density modeling of the Jan Mayen-East Greenland region, NE Atlantic

Lithospheric control on asthenospheric flow from the Iceland plume: 3D density modeling of the Jan Mayen-East Greenland region, NE Atlantic

Pingchuan Tan[1], Judith Sippel[2], Asbjørn Johan Breivik[1], Christian Meeßen[2], and Magdalena Scheck-Wenderoth[2,3]

[1]Centre for Earth Evolution and Dynamics, Department of Geoscience, University of Oslo, Oslo, Norway

[2]German Research Centre for Geosciences (GFZ), Potsdam, Germany

[3]Faculty of Georesources and Materials Engineering, RWTH Aachen University, Aachen, Germany

Abstract. The density structure of the oceanic lithosphere north of Iceland is key for understanding the effects of the Iceland Plume on the greater Jan Mayen-East Greenland Region. We obtain the 3D density structure of the sediments and the crust from regional reflection and refraction seismic lines. The temperature and related density structures of the mantle between 50 and 250 km are derived from a shear-wave velocity (Vs) tomography model. To assess the density between the Moho and 50 km depth, we combine forward and inverse 3D gravity modeling. Beneath the Middle Kolbeinsey Ridge (MKR) region, the deep negative density anomaly continues upwards into the uppermost mantle, where its lateral dimensions narrow considerably. This elongated anomaly does not entirely coincide with the spreading axis, and is increasingly displaced eastwards of it to the north. It crosses the West Jan Mayen Fracture Zone (WJMFZ) and becomes weaker approaching the Mohn's spreading ridge. The effect of this anomaly is consistent with significantly shallower basement on the eastern side of the MKR. We interpret this as the result of thermal erosion of the lithosphere by hot asthenospheric flow out from the Iceland Plume, possibly the main driver for several eastward jumps of the MKR during the last 5.5 Ma. The cause for the deviation of the flow may be that the WJMFZ is easier to cross in a region where the difference in lithospheric thickness is small. That implies that the bottom lithospheric topography exerts a regional but not local influence on upper-asthenospheric flow.

Key points:

• A gravity-derived 3D lithospheric density structure on the greater Jan Mayen-East Greenland Region

• A low-density anomaly deviates to the east from the Kolbeinsey Ridge across the West Jan Mayen Fracture Zone to the Mohn's Ridge

• The bottom lithospheric topography exerts a regional influence on upper-asthenospheric flow driven northwards by the Iceland plume

1 Introduction

The Iceland Plume exerts far-field effects on the thermal structure of adjacent mid-ocean ridges, both to the south (Reykjanes Ridge) (e.g. *White et al.*, 1995; *Ito*, 2001; *Parnell-Turner et al.*, 2014) and to the north of the plume (e.g. *Jones et al.*, 2002; *Pilidou et al.*, 2005; *Howell et al.*, 2014). There is debate as to what extent the spreading ridges channel the flow of plume material, or if it is more symmetrical (e.g. *Shorttle et al.*, 2010; *Ito*, 2001). Using observed seismic anisotropy patterns beneath Iceland, *Xue and Allen* (2005) suggest that there is a ridge-channelled flow of material away from Iceland towards the southern end of the Kolbeinsey Ridge. Based on a regional tomography model and observed gravity field, *Marquart et al.* (2007) pointed out that the Kolbeinsey Ridge is dominated by a divergent flow, which is explained by a combination of plume and spreading flux along the ridge. A later examination of geophysical and geochemical data along the Kolbeinsey Ridge, on the other hand, motivated *Shorttle et al.* (2010) to suggest that the Iceland Plume spreads in a radial, pancake-like fashion. Recent high-resolution 3D thermo-mechanical numerical modeling suggests that flow of the plume material along the Kolbeinsey Ridge is constrained by pre-existing lithosphere structures related to the rifting of the Jan Mayen microcontinent off East Greenland (*Koptev et al.*, 2017).

Several studies suggest that a lateral mantle flow related to the Iceland Plume extends as far north as the West Jan Mayen Fracture Zone (WJMFZ) (*Jones et al.*, 2002; *Breivik et al.*, 2008; *Howell et al.*, 2014), shown by a sub-lithospheric low-velocity layer observed under the study area (*Rickers et al.*, 2013; *Pilidou et al.*, 2005). Similarly, the refraction seismic studies of *Hooft et al.* (2006) indicate that the Kolbeinsey Ridge (Fig. 4.1) is characterized by shallow mantle melting caused by a hot and less viscous outflow of the Iceland Plume into the asthenosphere under the ridge. Both regional geochemical and seismic studies suggest a decreasing amount of thermal and geochemical plume influence

with distance from the center of the Iceland plume (e.g. *Schilling*, 1999; *Hooft et al.*, 2006; *Kodaira et al.*, 1997; *Klingelhöfer et al.*, 2000a).

The thermal structure of oceanic lithosphere is controlled by its cooling history so that temperature decreases with increasing age and distance from a mid-ocean ridge (e.g. *Stein and Stein*, 1992; *Doin and Fleitout*, 1996; *Adam and Vidal*, 2010). The question is how the Iceland Plume affects the thermal state of the greater Jan Mayen-East Greenland Region, where different segments of a number of active mid-ocean ridges meet (Fig. 4.1). *Haase et al.* (2016) published 3D forward-and inverse- gravity modeling of the NE Atlantic, where the temperature-dependent lithospheric mantle densities are derived from the age of the oceanic lithosphere following the approach of *Sandwell* (2001). We note that their model has a mass excess along the Kolbeinsey Ridge and north of the WJMFZ. This area correlates with an area of low upper mantle seismic S-wave velocities (*Rickers et al.*, 2013), which suggests that the upper mantle densities have been overestimated, and that the gravity misfit in their model could be related to mass anomalies caused by the Iceland plume.

Measured gravity anomalies are the result of the density structure from the shallowest sediments, crust, and upper mantle. Information about the upper mantle density below 50 km can be derived from mantle tomography models, while the crustal structure and sediment distribution is reasonably well known from active source seismic data. We can use variations in the observed gravity field of the greater Jan Mayen-East Greenland Region to derive the density configuration of the upper mantle above 50 km to infer first-order trends of related temperature variations. The seafloor, the top of the basement (interface between sediments and crystalline crustal rocks) and the Moho (crust-mantle boundary) represent the most important density contrasts in the lithosphere. The region is relatively well covered by geological and geophysical observations derived from reflection and refraction seismic data (e.g. *Kodaira et al.*, 1997, 1998a; *Hermann and Jokat*, 2016), teleseismics (e.g. *Rickers et al.*, 2013) and gravity data (e.g. *Gaina et al.*, 2011) (Fig. 4.1, Tab. 4.1).

The objective of our study is to develop a 3D density model of the study area that is consistent with all available geophysical observations to provide new constraints on the geometry and extent of the mantle domain that is presently most affected by the Iceland Plume.
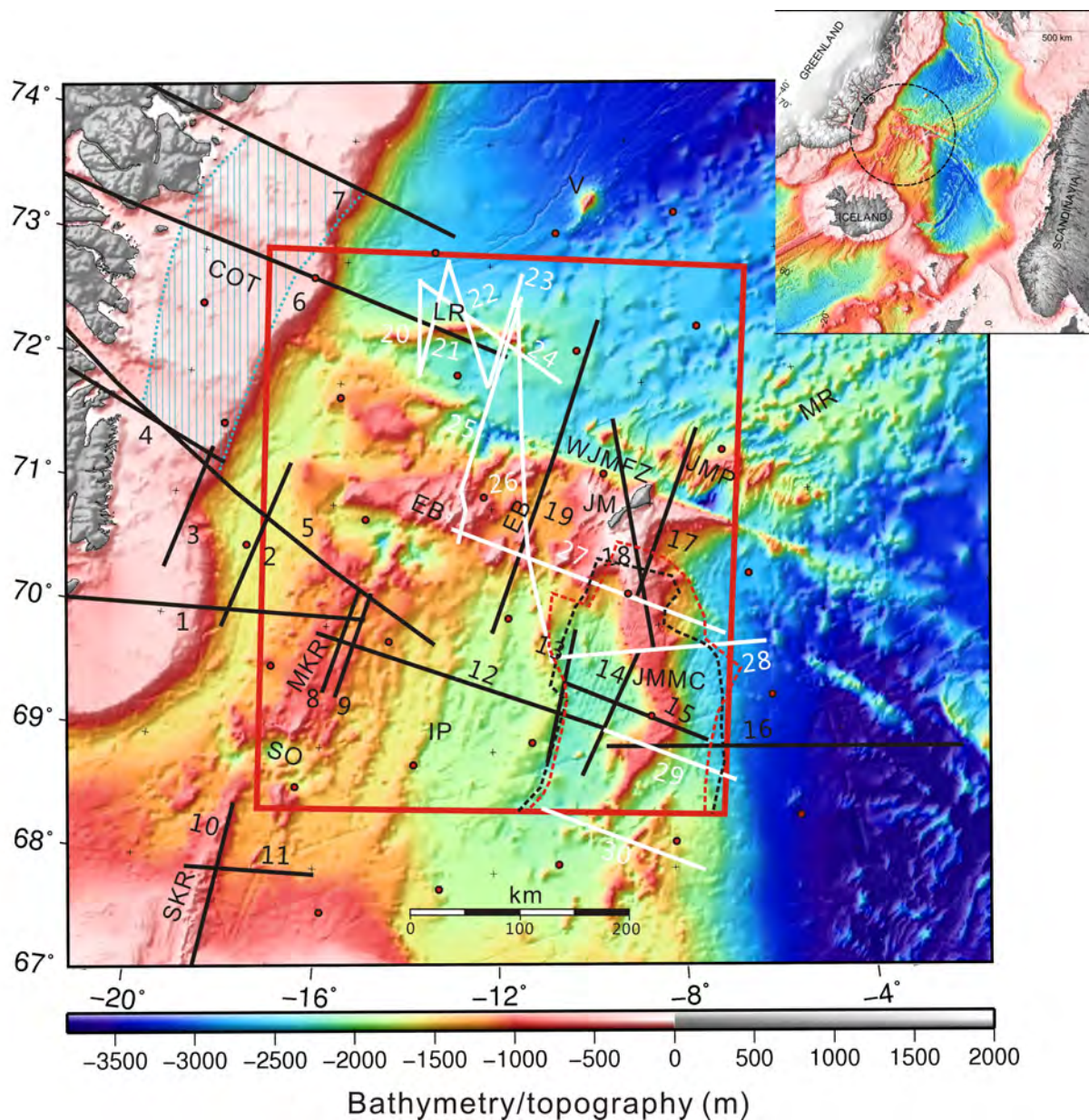
Figure 4.1: Topography and bathymetry of the study area (IBCAO-3) (*Jakobsson et al.*, 2012). Inserted map (ETOPO 2V2) (*National Geophysical Data Center*, 2006) shows the location of the study area. The black and white lines show the locations of refraction and reflection seismic lines, respectively (annotations in Table 4.1). The Continent Ocean Transition Zone (COT) is shown in blue dotted lines (*Hermann*, 2013; *Voss and Jokat*, 2007), outline of the Jan Mayen Microcontient (JMMC)(black dashed line) is derived from *Peron-Pinvidic et al.* (2012a,b), while the red dashed line represents the location of the JMMB by (*Breivik et al.*, 2012a) incorporating results from *Kandilarov et al.* (2012). The red dots represent data points sampled from tomography model with a horizontal spacing of 100 km (*Rickers et al.*, 2013). EB: Eggvin Bank, IP: Iceland Plateau, JM: Jan Mayen Island, JMP: Jan Mayen Plateau, JMMC: Jan Mayen Microcontinent, LR: Logi Ridge, MKR: Middle Kolbeinsey Ridge, MR: Mohn's Ridge, SO: Spar Offset, SKR: South Kolbeinsey Ridge, V: Vesteris Seamount.

Table 4.1: Database for the construction of a 3D structural and density model that differentiates the main sedimentary and crustal units

Label (Fig. 4.1)	Line name	Reference	Available information
		Input regional seismic reflection and refraction lines	
1-4	ARK 1988 lines 3-6	Weigel et al. (1995)	V_p model, 2D gravity
5	AWI20090100	Herrmann (2013)	V_p model, 2D gravity
6-7	AWI20030400 and AWI 20030500	Voss and Jokat (2007)	V_p model, 2D gravity
8-9	JMKR-95 lines 1-2	Kodaira et al. (1997); Mjelde et al. (2002)	V_p model, V_s model
10	KRISE line 1	Hooft et al. (2006)	V_p model, 2D grav-ity,isostasy
11	KRISE line 4	Parnall (2010)	V_p model
12	JMKR-95 lines 3	Kodaira et al. (1998b); Mjelde et al. (2002)	V_p model, V_s model
13-15	JMKR-95 lines 4-6	Kodaira et al. (1998a); Mjelde et al. (2007)	V_p model, V_s model, 2D gravity
16	OBS 2000 lines 8-00	Breivik et al. (2012a)	V_p model
17-18	OBS-JM-2006 lines 1-2	Kandilarov et al. (2012, 2015)	V_p model, V_s model, 2D gravity
19	Profile-1	Tan et al. (2017)	V_p model, V_s model
20-24	Profile2-6	Breivik et al. (2012b)	Reflection seismic
25-27	NPDJM11-004,005,006	Sandstå et al. (2012)	Reflection seismic
28-30	NPD08, Inseis 01, Inseis 06	Peron-Pinvidic et al. (2012a,b)	Reflection seismic

Name	Reference	Comments
	Additional input data	
Crustal models of the Mohn's Ridge	(Klingelhöfer et al., 2000b,a)	Constrain the Moho depth in the Mohn's Ridge for oceanic ages less than 22 Ma (Fig. 4.2c)
Moho depth of NE Atlantic	(Haase et al., 2016)	Derived from 3D gravity inversion modeling; here only used in the NKR and nearby Eggvin Bank where refraction seismics are lacking (Fig. 4.2c)
Sediment thickness of world's ocean and marginal seas	(Divins, 2004)	Grid spacing of 5 arc-minutes by 5 arc-minutes provides additional information on the depth of the basement
CRUST 1.0	(Laske et al., 2013)	1 × 1 degree grid provides additional information on the depth of Moho

2 Geological setting

The research area extends from the Jan Mayen Ridge to the east coast of Greenland, and from the South Kolbeinsey Ridge (SKR) in the south (Spar offset) to the Logi Ridge in the north (Fig. 4.1). With the very slow-spreading Kolbeinsey and Mohn's ridges (full spreading rate less than 20 mm/yr) (*Gaina et al.*, 2009), the anomalously shallow Eggvin Bank, the Jan Mayen Microcontinent (JMMC), and the tectonically active WJMFZ, the region represents one of the most complex areas of the NE Atlantic region.

The rifting of the JMMC off the East Greenland margin occurred around 24-25 Ma due to the spreading axis jump from the Aegir Ridge to the Kolbeinsey Ridge (e.g. *Nunns*, 1982). The spreading along the Kolbeinsey Ridge is slow (full rate: 16-18 mm/yr) and nearly orthogonal (*Appelgate*, 1997). It underwent several minor eastwards jumps of the spreading axis (e.g. *Appelgate*, 1997). The Kolbeinsey Ridge is divided into three different sections (southern, middle and northern part), of which the study area only covers the middle and northern parts. The Middle Kolbeinsey Ridge (MKR) and surrounding Iceland Plateau show abnormally thick oceanic crust (average 9 km) and shallow bathymetry (*Kodaira et al.*, 1997, 1998b), which is attributed to the thermal influence of the Iceland Plume (*Kodaira et al.*, 1997, 1998a,b; *Elkins et al.*, 2011). The MKR basalts are related to a homogeneously depleted mantle source (e.g. *Elkins et al.*, 2011). In contrast, the basalts from the North Kolbeinsey Ridge (NKR) and nearby Eggvin Bank are enriched in incompatible elements and radiogenic isotopic composition (e.g. *Haase et al.*, 2003; *Elkins et al.*, 2016). A seismic refraction line across the Eggvin Bank approximately 70 km east of the NKR shows large variations in crustal thickness (from 8 to 13 km) (*Tan et al.*, 2017). The seismic velocities indicate that there could be some thermal Iceland plume influence under the northern Eggvin Bank, while the elevated magmatism in the southern Eggvin Bank may be mostly affected by an enriched mantle source (*Tan et al.*, 2017).

The WJMFZ offsets the spreading right-laterally by around 200 km. North of the fracture zone, opposite of the Jan Mayen Island (Fig. 4.1), spreading takes place on the Mohn's Ridge. The formation of the Mohn's Ridge dates back to the continental breakup between Greenland and Norway in the Early Eocene (54-55 Ma). The spreading is symmetrical but moderately oblique at a full rate of 16 mm/yr, mostly producing a thin oceanic crust (4 ±0.5 km) (*Kandilarov et al.*, 2012; *Klingelhöfer et al.*, 2000a,b). The thick oceanic crust observed along the East Greenland and conjugate Norwegian margins show that the commencement of the Mohn's Ridge was influenced by the Iceland Plume through active upwelling or an enriched component could be superimposed to

increase magma productivity during the earliest spreading phase (e.g. *Voss and Jokat*, 2007; *Breivik et al.*, 2009, 2014).

The JMMC has large crustal thickness variations. The maximum thickness is observed at the northern boundary of the JMMC (25 km), while the minimum could be as low as 3 km (*Kandilarov et al.*, 2012; *Kodaira et al.*, 1998a). In addition, the eastern and western sides of JMMC are interpreted as volcanic and non-volcanic rifted margins, respectively (e.g. *Kodaira et al.*, 1998a; *Breivik et al.*, 2012a).

3 3D gravity modeling

3.1 Modeling strategy

Aside from one refraction seismic profile (*Hermann and Jokat*, 2016), there is a lack of seismic constraints on mantle densities between 50 km (b.s.l.) and the Moho. Hence, the main purpose of performing 3D gravity modelling is to close this observation gap between the crust and mantle densities that can be obtained from mantle tomography. Therefore, we integrate the data-derived densities for the sediments, crust and deeper mantle into an initial 3D density model and adjust the 3D density configuration of the shallowest mantle until the gravity response of the entire 3D model is consistent with the observed gravity anomalies.

First, we calculate the gravity response of an initial 3D density model that includes the data-constrained densities of the sediments, crust and deeper mantle, while including a constant density of 3300 kg/m^3 for the shallowest unconstrained mantle (forward gravity modelling). As a result of this step, we obtain the difference between the observed and the modelled gravity anomalies, i.e. the residual of this initial 3D density model. In a second step, we use these residual gravity anomalies to invert for the density configuration of the shallowest mantle above 50 km depth (inverse gravity modelling).

For the forward calculations, we use the Interactive Gravity and Magnetic Application System IGMAS+ (*Götze and Lahmeyer*, 1988; *Schmidt and Götze*, 1998; *Schmidt et al.*, 2011). IGMAS+ calculates the total gravity response of a predefined 3D density model by combining triangulated model geometries (polyhedrons that geometrically define geological units) with density information attached to voxel cubes. For the inverse gravity modelling step, we make use of a modified version (*Meeßen et al.*, 2018) of the Harvester module (*Uieda and Barbosa*, 2011), which is part of the open-source code library *fatiando a terra* (for Python 2.7; (*Uieda et al.*, 2013)).

3.2 Modeling the structure and density of the sediments and cystalline crust

Previous studies, including (i) the interpretation of reflection seismic data (*Blischke et al.*, 2016; *Peron-Pinvidic et al.*, 2012a,b) , (ii) wide-angle refraction seismic data (*Klingelhöfer et al.*, 2000a,b; *Voss and Jokat*, 2007; *Breivik et al.*, 2012a; *Kodaira et al.*, 1997, 1998b; *Tan et al.*, 2017; *Hermann and Jokat*, 2016; *Kandilarov et al.*, 2012, 2015; *Weigel et al.*, 1995), and (iii) studies of dredged samples (e.g. *Haase et al.*, 2003; *Elkins et al.*, 2011, 2016; *Mertz et al.*, 2004; *Klingelhöfer et al.*, 2000a; *Schilling*, 1999), show that the study area is characterized by large variations in terms of crustal structure as well as mantle composition, and mantle melting degree. Table 4.1 and Figure 4.1 provide an overview of the data types and sources used to develop a 3D structural and density model for the crystalline crust and sedimentary cover. Based on the published interpretations, we find that 10 sedimentary and crustal units can be traced regionally (left column of Tab. 4.2) and thus be used to construct the elements for the 3D density model.

The Cenozoic sediments are dominated by muds and silts with some additional ice-rafted material from the recent glacial periods (e.g. *Haase et al.*, 2003; *Thiede and Hempel*, 1991; *Blischke et al.*, 2016). At depths down to 1 km they are estimated to have low densities (2100 kg/m^3); higher densities (2400 kg/m^3) were assigned to deeper Cenozoic sediments (burial greater than 1 km). The pre-Cenozoic sediment layers, which are only observed in the JMMC, are characterized by relatively high velocities (4.5-5.6 km/s), and thus are modeled with the highest sedimentary densities (2650 kg/m^3).

The oceanic crust is divided into two layers, a lower-velocity upper crust (V_p: 2.5-6.6 km/s) and a high-velocity lower crust (V_p: 6.6-7.6 km/s). The upper oceanic crust corresponds to pillow lavas and sheeted dikes (*Detrick et al.*, 1994; *Dilek*, 1998). It is strongly influenced by fissures and cracks causing higher porosity (*Jacobson*, 1992), thus it was assigned lower densities (2700 kg/m^3). The lower crust is characterized by gabbroic rocks of low porosity and higher density (3000 kg/m^3). Dense intruded bodies (3160 kg/m^3) are indicated by regional refraction studies in the area of the Greenland continental-ocean transition (COT) (Fig. 4.1) (*Hermann*, 2013; *Voss and Jokat*, 2007).

The continental crust of the JMMC is divided into an upper layer of lower V_p (4.5-6.5 km/s) and modeled density (2700 kg/m^3) and a lower layer of higher V_p (6.5-6.85 km/s) and density (2950 kg/m^3). A relatively dense upper (2900 kg/m^3) and lower crust (3050 kg/m^3) is restricted around the northern boundary of the JMMC where the Moho depth is greatest (*Kandilarov et al.*, 2012, 2015).

Table 4.2: Densities of geological units from publications used to setup the initial 3D density model (last column).

	Density (kg/m³) published for the surrounding area								Modeled Density (kg/m³)
	Voss and Jokat (2007)	Weigel et al. (1995)	Peron-Pinvidic et al. (2012a,b)	Mjelde et al. (2007)	Kandilarov et al. (2012)	Hooft et al. (2006)	Hermann et al. (2013)	Haase et al. (2016)	
	East Greenland (Logi Ridge)	East Greenland (MKR)	JMMC	JMMC, Iceland Plateau	JMMC, Jan Mayen	SKR	NE Atlantic (3D modeling)	NE Atlantic (3D modeling)	
Water	1030	1030	1030	1030	1030	1030	1030	1030	1030
Cenozoic upper	2000-2400	2100	2100	2000	2200		1900-2100	2200	2100
Cenozoic lower	2330-2520		2100	2300	2400		2400	2200-2700	2400
Precenozoic	2560-2650	2300-2600	2560	2520-2730	2400		2200-2700	2650	2650
Upper oceanic crust	2600	2800-2900	2750	2840		2850	2900	2850	2700
Lower oceanic crust	2900	3000-3100	3000	3000		2850	2900	2850	3000
Upper continental crust	2720		2740	2700-2820	2750-2950		2700	2750	2700
Lower continental crust	2830-2900		2950	2830-2960	3050		2950	2950	2950
Lower-crustal intrusions	3160						3180		3160
Upper crust (JMMC)					2900			2950	2900
Lower crust (JMMC)					3050			2950	2900
Upper mantle	3240-3310	3200-3300	3300		3200-3400	3240	3220-3310	3200-3300	3050

The modeled crustal densities are consistent with empirical velocity-density relationships (*Barton*, 1986) and are within the range of densities from previous studies (Tab. 4.2). The Moho depth is mainly constrained by seismic lines revealing mantle refractions (P_n) and Moho reflections (P_mP). It represents an intra-lithospheric boundary with a large density contrast, which is characterized by an increase in P-wave velocity to values greater than 7.6 km/s.

We used QGIS (*QGIS Devlopment Team*, 2009) to georeference all the seismic data into a consistent coordinate system (UTM 28N). Since seismic profiles do not cover the entire area, we have implemented additional datasets (Tab. 4.1). These are (i) a crustal model of the Mohn's Ridge (Greenland Basin) covering the region of oceanic ages of less than 22 Ma (*Klingelhöfer et al.*, 2000a); (ii) Moho depths of the NE Atlantic as derived by 3D gravity inversion (*Haase et al.*, 2016), that were only used in the NKR and nearby Eggvin Bank where refraction seismic data are lacking; (iii) a global model of oceanic sediment thickness (*Divins*, 2004) and (iv) crustal thickness (CRUST 1.0) (*Laske et al.*, 2013) (Tab. 4.1, Fig. 4.2c). These models provide additional information on the depth of basement and the Moho, which we use to fill the gaps between the preferred original seismic data.

The data from inside and outside the study region (red frame in Fig. 4.1) were jointly interpolated with Petrel (by Schlumberger 1998-2013) using the Minimum Tension Gridding algorithm to create regular grids of interfaces. In case of the WJMFZ, due to the sharp changes across the fracture zone, we first interpolate between seismic lines north of the WJMFZ to create regular grids, then we interpolate between seismic lines south of the WJMFZ, and finally we combine these two grids together. The dimensions of the final modeling area are 420 km in north-south direction and 500 km in east-west direction. The model has a horizontal node spacing of 10 km in both northing and easting directions. The vertical spacing (down to Moho depth) corresponds to the thickness of the different geological units. The chosen model node spacing preserves the main structural trends derived from the seismic refraction and reflection lines.

Figure 4.2 shows the two key horizons (top basement and Moho), as well as sediment and crustal thickness. The basement depth in the oceanic domain increases with increasing distance from the spreading centers (Fig. 2a). In addition, wide parts of the Kolbeinsey Ridge, Iceland Plateau and Eggvin Bank are high standing areas. Here, the depth of the basement is almost equal to the seafloor bathymetry, while a thin layer of sediments ($<$ 2 km) is observed in the western domain of the MKR. In the Greenland Basin (north of the WJMFZ), the sediments are only Cenozoic with a thickness of less than 500 m around
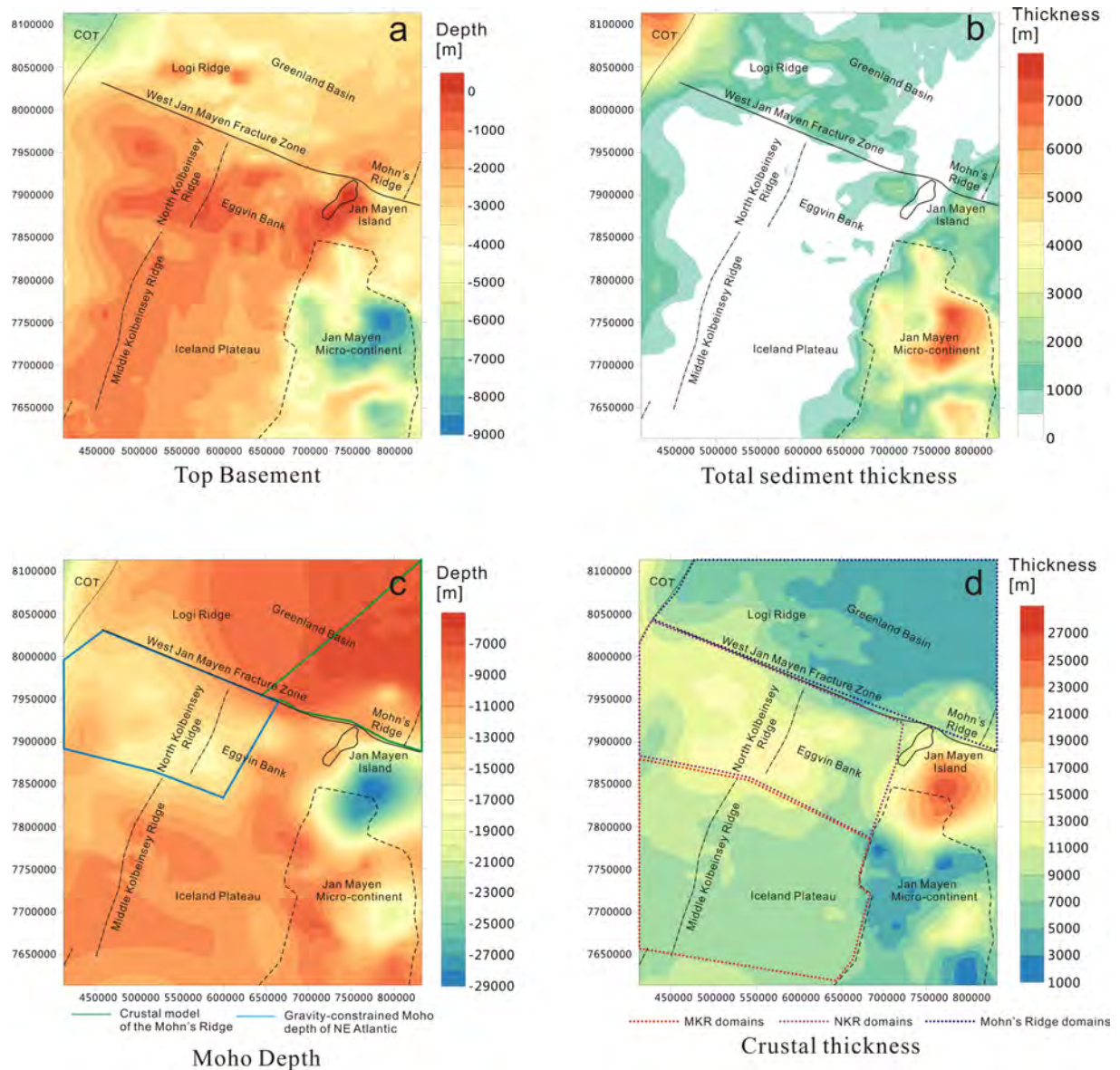
Figure 4.2: Major structural elements of the crust. Locations of three present day spreading axis are derived from regional magnetic anomaly data (*Olesen et al.*, 2007). a: Depth to the top of the crystalline crust (basement), b: Total sediment thickness, c: Depth to the crust-mantle boundary (Moho) as mostly constrained by seismic data (Fig. 4.1), the area constrained by the crustal model of the Mohn's Ridge (*Klingelhöfer et al.*, 2000b) and gravity-constrained Moho depth of the NE Atlantic (*Haase et al.*, 2016) are presented by green and blue lines, respectively. d: Thickness of the crystalline crust; the color-coded dotted lines outline three different domains (MKR, NKR, and Mohn's Ridge) used for further analysis (see main text).

the Mohn's spreading ridge, increasing to 7000 m towards the continent-ocean boundary off Greenland (Fig. 4.2b). The JMMC is covered by sediments varying in thickness from 0 to 7000 m (Fig. 4.2b). The sedimentary section is thickest along the eastern margin of the JMMC (Fig. 4.2b).

In the Greenland Basin, the Mohn's Ridge shows a shallow Moho depth of approx. 7 km, while the Moho depth increases to 19 km towards the continent-ocean boundary off Greenland (Fig. 4.2c). The average crystalline crustal thickness is around 8.5 km along the MKR and adjacent Iceland Plateau, and increases to around 12-15 km over the NKR and Eggvin Bank (Fig. 4.2d). In the JMMC, the Moho depth varies strongly with the shallowest depths beneath the western edge of the JMMC (Jan Mayen Basin) (8.5 km), moderate depths beneath the eastern edge of the JMMC (Jan Mayen Ridge) (18 km), and largest depths around the northern part of the JMMC (27 km) (Fig. 4.2d). The western margin of the JMMC shows an abrupt transition from thin continental crust (5 km) to a thick oceanic crust (9 km) in the Iceland Plateau (Fig. 4.2d).

3.3 Density configuration of the mantle at depths below 50 km (b.s.l.)

The seismic wave velocity configuration of the mantle provides constraints on its thermal and hence density structure, although the proposed methods of wave velocity conversion differ significantly (*Cammarano and Guerri*, 2017). For the greater Jan Mayen-East Greenland Region, the velocity of horizontally polarized shear waves (V_{SH}) in the mantle can be derived from a tomographic model of the North Atlantic region (*Rickers et al.*, 2013). It is based on non-linear full-waveform inversion techniques and measurements of the instantaneous phase misfit. Compared to the global S-wave model S20RTS (*Ritsema et al.*, 1999) and European full-waveform model (EU-TF) (*Fichtner and Trampert*, 2011), the V_{SH} model (NA-IP) (*Rickers et al.*, 2013) is characterized by a significantly improved resolution for both the upper and lower mantle; therefore, it images small-scale anomalies, such as spreading ridges and plume distribution under the NE Atlantic Region. The V_{SH} model comes with a horizontal grid spacing of 100 km and a depth-dependent vertical spacing of 10 km in the uppermost 350 km, 20 km between 350 and 700 km, and 50 km between 700 and 1300 km depth. Given the vertical grid size of the V_{SH} tomography (10 km) at shallow depths and the maximum Moho depth (> 28 km) (Fig. 4.2c), we suggest that the values of V_{SH} shallower than 50 km are likely to be artificially affected by the crustal velocities. In addition, compared to the V_{SH} data at greater depth (e.g. 100

km), the mantle between the Moho and 50 km is more likely represented by lithospheric mantle compared to asthenospheric mantle. Therefore, we restrict the usage of V_{SH} data to depths >50 km for 3D gravity modeling. First we convert the regional V_{SH} tomography model into mantle temperature. Then, the mantle density can be estimated as a function of pressure and temperature.

Conversion of shear-wave velocity to temperature

Based on an averaged shear wave velocity model and a generic thermal model for the Pacific oceanic lithosphere, *Priestley and McKenzie* (2006) proposed a set of empirical equations and constants to convert mantle shear wave velocity to temperature (T). The conversion method is based on the assumption that the shear-velocity structure of the oceanic upper mantle can be largely explained by its temperature, pressure, and some activation processes that are related to an elastic behavior close to melting temperatures. Retained melt present at low concentration is expected to have a minor impact. Hence, this non-linear V_s-T-relationship is assumed to be valid for any mantle composition, while being most accurate for temperatures that exceed 1100°C.

For the V_s-T-conversion, the original S wave model has been extracted for the depth range of 50-250 km. The V_s model has been rescaled by applying the Triangulation Method of the software OpendTect (*Huck*, 2012) to create a regular grid with 10x10 km horizontal and 10 km vertical dimension. This node spacing is consistent with the upper crustal and sedimentary model. One variable to be predefined for the empirical equations to be solved is pressure (*Priestley and McKenzie*, 2006). In this study, we use sedimentary and crustal density structures (Tab. 4.2) and an assumed constant mantle density (3300 kg/m³) to estimate the corresponding pressure variations. Figure 4.3a shows the temperature configuration derived from the entire tomographic model in the parameter space of V_{SH}, depth and pressure. In general, the converted temperature is increasing as the depth increases and velocity decreases, but lateral temperature differences are much larger at shallow depths.

The V_s-to-T conversion is a strongly nonlinear function of temperature and the uncertainties of the temperature estimates decrease with increasing temperature (*Priestley and McKenzie*, 2006, 2013). As proposed by *Priestley and McKenzie* (2013), V_s derived temperatures below 900°C are associated with large uncertainties, where a change in V_s of 0.04 km/s would result in a 250°C difference. The same V_s change at 1200°C would correspond to 100°C and at 1350°C, it would only be 30°C (Fig. 4.3a).

Conversion of temperature to density

The density of the mantle is controlled by its composition and the *in situ* pressure and temperature conditions. Throughout this modeling study, we assume that the mantle of the greater Jan Mayen-East Greenland Region is compositionally homogeneous. *Bai et al.* (2014) have proposed a set of equations to calculate the density of mantle rock at given pressure and temperature. Thereby, both the thermal expansion coefficient (α_T) and the bulk modulus (K_T) are considered as temperature dependent, while the authors derive their formulation from laboratory measurements on olivine samples as described by *Kroll et al.* (2012). The latter, in turn, is based on a large number of thermal expansivity measurements and an up-to-date summary of bulk modulus data. The mantle density affected by thermal expansion at temperature T is:

$$\rho_T = \rho_0[1 - \alpha_T(T - T_0)] \tag{3.1}$$

where T_0 is equal to 273 K, while ρ_0 is the mantle reference density (3300 kg/m^3) at temperature T_0. The relationship between α and T is estimated by *Bai et al.* (2014) with a nonlinear function of temperature:

$$\alpha_T = (6 \times 10^{-10}T^3 - 2 \times 10^{-6}T^2 + 0.0039T + 1.727) \times 10^{-5} \tag{3.2}$$

The bulk modulus K represents the pressure change required for a given volume change. The bulk modulus can be calculated as a function of temperature (*Kroll et al.*, 2012):

$$K_T = 127.97 - 0.0232(T - 300) \tag{3.3}$$

where the units for K_T and T is GPa and K, respectively.

The density changes related to the *in situ* pressure ($\Delta\rho_p$) at a specific pressure (P) and bulk modulus (K) can be calculated using the following function (*Bai et al.*, 2014):

$$\Delta\rho_p = \rho_0[P - P_0]/K_T \tag{3.4}$$

where P_0 is the standard atmospheric pressure and the unit for P is GPa.

Finally, the mantle density for a specific temperature and pressure is calculated:

$$\rho = \rho_T + \Delta\rho_p \tag{3.5}$$

Figure 4.3b shows the density variation for pressure and temperature ranges of 1 to 8 Gpa and 600 to 1600°C, respectively. At a given depth, high mantle temperature corresponds to lower mantle density, while at a given temperature, the larger the pressure (greater depth) the higher the corresponding mantle density. Under a specific temperature and pressure, the modeled mantle density reveals similar results compared to mantle densities based on *Grose and Afonso* (2013) and *Schutt and Lesher* (2006) using the same reference mantle density (3300 kg/m^3).

Results

Figure 4.3c shows the calculated mantle density variation as a function of the pressure and V_s variations. For most of the parameter field, density increases with depth. At depths shallower than 90 km, the mantle densities reveal large lateral variations due to large variations in mantle temperature (Fig. 4.3a). The calculated mantle density range at 50 km depth is 151 kg/m^3 (3127-3278 kg/m^3), decreasing to 10 kg/m^3 (3145-3155 kg/m^3) at 90 km depth. The mantle densities at depths greater than 90 km have a range of less than 10 kg/m^3 (Fig. 4.3b).

The MKR, NKR, and Mohn's Ridge show significantly different V_s, mantle temperature and density configurations (Fig. 4.3), in particular at depths shallower than 90 km. At a given depth, MKR has the lowest V_s, correspondingly highest mantle temperature and lowest mantle density. In contrast, the Mohn's Ridge shows the highest V_s, lowest mantle temperature and largest mantle density.

Figure 4.3a shows that under the MKR domain, the thermal gradient is decreasing with increasing depth. At shallower depth (<90 km), the average thermal gradient is 2.5 K/km. At depths >90 km, thermal gradients decrease to an almost constant value around 0.8 K/km. The mantle densities at MKR are characterized by small changes (3130 to 3140 kg/m^3) at depth shallower than 90 km, which indicates that the temperature and pressure effects nearly compensate each other. At depths >90 km, the mantle density is mainly influenced by the pressure as it is gradually increasing with a constant density gradient of around 1 kg/m^3/km.

The mantle temperature below Mohn's Ridge is characterized by a significantly higher thermal gradient (>20 K/km) at depths between 50 and 70 km. However, where depths exceed 70 km, the thermal gradient is similar to the MKR. Under the Mohn's Ridge, the average mantle density is decreasing from 3230 kg/m^3 (50 km depth) to 3150 kg/m^3 (70 km depth) (Fig. 4.4b). At depths larger than 70 km, the mantle density is gradually increasing (1 kg/m^3/km) as the pressure plays a more significant role to determine the
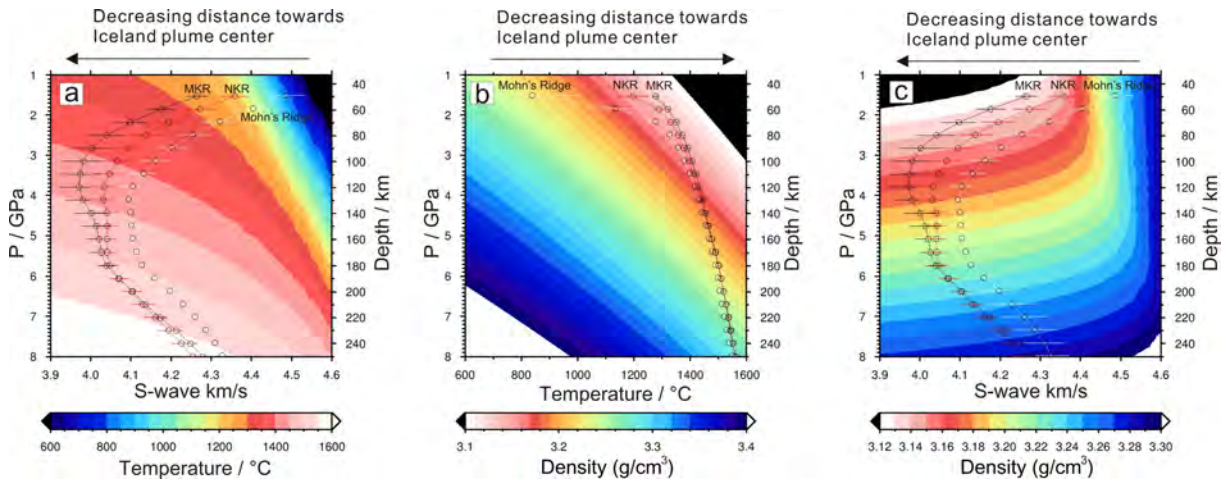
Figure 4.3: a: Temperature field calculated by using the conversion of *Priestley and McKenzie* (2006). b: Results of density calculation (Eq. 3.1–3.5) applied to pressure and temperature ranges of 1 to 8 GPa and 600 to 1600 °C. c: Calculated density as a function of the pressure and S wave velocity variations. Superimposed circles and bars represent the parameter variation obtained from sub-domains of the study area; the horizontal bars indicate the standard deviation of V_s (Fig. 4.3a,c) and temperature (Fig. 4.3b), while the mean is indicated by the circles. The black, red, and white lines show the data derived from MKR, NKR, and Mohn's Ridge domains (Fig. 4.2d) respectively.

mantle density. At a given depth, the average mantle temperature and density of the NKR domain are between those of the MKR and Mohn's Ridge.

As the largest lateral temperature and density variations are observed for depths between 50 and 90 km, we plot the average mantle temperature (T_{50-90}) and density (ρ_{50-90}) for this depth interval (Fig. 4.4c-d). In general, this interval shows trends of decreasing T_{50-90} (increasing ρ_{50-90}) from MKR to NKR and to Mohn's Ridge, and each ridge also shows similar trends of decreasing temperature (increasing density) with increasing age of the oceanic crust. For example, under the MKR domain, T_{50-90} is 1350°C under the ridge axis and gradually decreases to 1310°C at locations where the oceanic crust is as old as 22 Ma. Under the Mohn's Ridge, the mantle temperature at the spreading center is 1270°C, while it decreases to 1050°C at around 45 Ma. In contrast to the MKR and Mohn's Ridge, the mantle temperature and density under the NKR domains have large variations, where the mantle temperature decreases (density increases) northward.
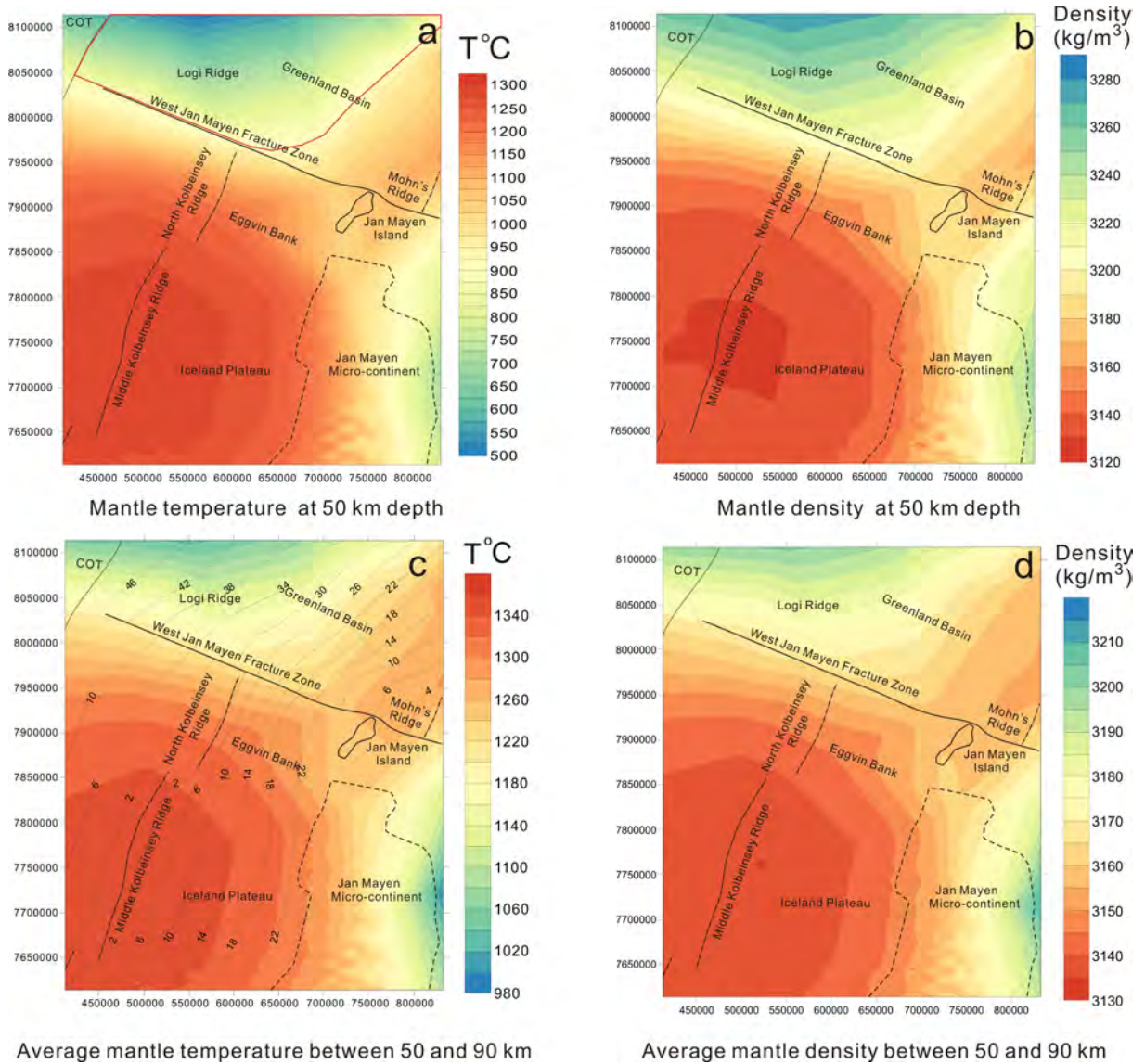
Figure 4.4:   a: Converted temperature variations at a depth of 50 km. The red solid line delineates an area within the Greenland basin with temperatures of less than 900 $°C$. b: Corresponding density variations at a depth of 50 km. c: Average mantle temperature between 50 and 90 km (T_{50-90}). The solid grey lines with numbers show the oceanic seafloor ages (*Müller et al.*, 2008). d: Average mantle density between 50 and 90 km (ρ_{50-90}).

3.4 Gravity response of the initial 3D density model

In order to avoid edge effects during the gravity modeling, we have extended the model horizontally by 300 km in all directions. The extended area is mainly constrained by regional seismic refraction studies (*Weigel et al.*, 1995; *Hermann*, 2013; *Voss and Jokat*, 2007; *Hooft et al.*, 2006; *Furmall*, 2010; *Brandsdóttir et al.*, 2015; *Klingelhöfer et al.*, 2000a) (Fig. 4.1), the global map of oceanic sediment thickness (*Divins*, 2004), and the model CRUST 1.0 (*Laske et al.*, 2013).

We performed the gravity modeling covering an area of 1020 × 1100 km (extended region) for the density configurations of the sediments, crust, and mantle above 250 km (regular 10km × 10km grids). The 3D density model in IGMAS+ is built upon a series of parallel vertical 2D planes, where the 3D structure is obtained by triangulating polyhedrons between planes. In this study, the gravity model contains 56 parallel working planes running in east-west direction at 20 km intervals. Thus, the 2D planes are approximately perpendicular to the mainly N-S directed major structural elements, crossing the most important gravity lows and highs (Fig. 4.5a).

To each sedimentary and crustal model unit, a homogeneous density is assigned (Tab. 4.2). The mantle density is constant (3300 kg/m³) between the Moho and 50 km, while the S wave-derived density configuration of the mantle between 50 and 250 km depth is modeled by a voxel grid with a regular spacing of 10 km in both horizontal and vertical directions.

The gravity field data that we have chosen to use is CAMP-G, a recently published satellite derived Arctic gravity field model (10×10 km grid resolution) containing free-air gravity anomalies offshore and bouguer anomalies onshore (Jan Mayen Island) (*Gaina et al.*, 2011) (Fig. 4.5a). Compared to other gravity field data (*Andersen et al.*, 2010; *Sandwell et al.*, 2014), this satellite derived gravity field shows relatively larger wavelength of the gravity anomalies, which is expected to be sufficiently sensitive to density anomalies at larger depth. There is a gravity low over the eastern margin of the JMMC and Jan Mayen Basin. The gravity field over the Eggvin Bank, Jan Mayen Island, and Jan Mayen Ridge show pronounced high gravity. In addition, the WJMFZ is characterized by a narrow gravity low bounded by positive gravity anomalies on both sides. The gravity over most parts of the Mohn's Ridge and the MKR reveal moderately positive anomalies, ranging from 20 to 40 mGal.

Figure 4.5c shows the residual gravity field (Root Mean Square (RMS): 34.24 mGal) calculated as the difference between the gravity response of the initial density model (Fig. 4.5b) and the observed gravity (Fig. 4.5a). Any negative gravity residual implies
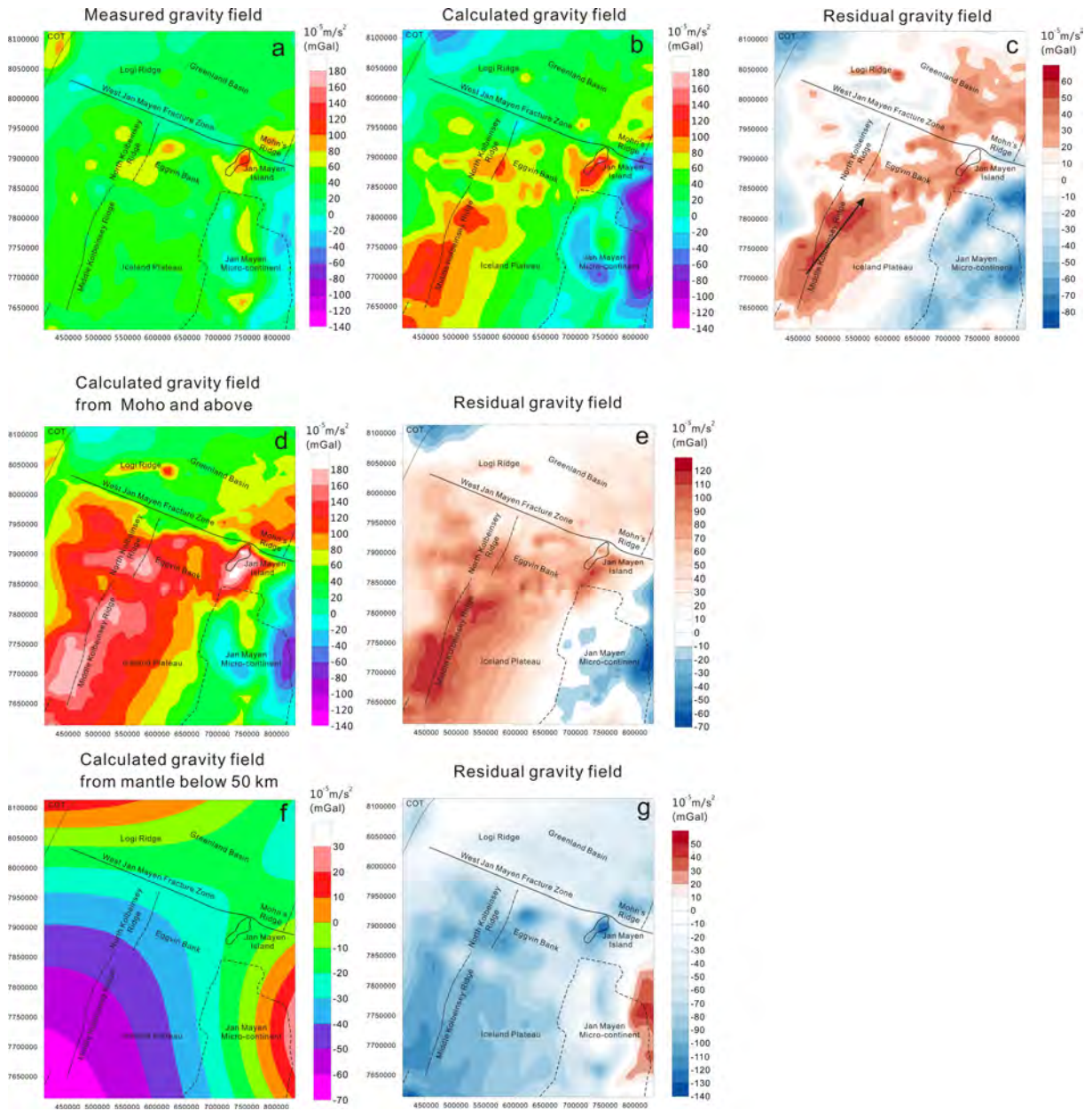
Figure 4.5: a: Observed gravity field; free air gravity anomaly offshore and the Bouguer anomaly for the Jan Mayen Island (*Gaina et al.*, 2011). b: Gravity field calculated for the initial 3D density model with homogeneous mantle density (3300 kg/m^3) between Moho and 50 km. c: The residual gravity field is the calculated filed subtracted the observed field. Blue colors indicate a mass deficit in the model, while the red areas show mass excess. The black arrow indicates the NE-SW axis of maximum positive gravity anomalies. d, e: The calculated gravity response induced only by masses located above the Moho, and the residual gravity field made by subtracting the observed field from it. f,g: The calculated gravity field from the mantle below 50 km, and the residual gravity field made by subtracting the observed field from it.

a mass deficit in that particular area of the model. The initial residual gravity field is characterized by a NE-SW striking, positve (up to 60 mGal) residual gravity anomaly trending from MKR to the Mohn's Ridge. At MKR, this anomaly runs slightly east from the spreading axis, where the gravity misfits are gradually decreasing away from this trend. The JMMC is dominated by short-wavelength negative residuals, while short-wavelength positive residual anomalies are observed at the Eggvin Bank. In addition, we calculated gravity response induced by masses located above the Moho (Fig. 4.5d) and mantle below 50 km (Fig. 4.5f), and their corresponding residual gravity anomaly fields (Fig. 4.5e,g), in order to understand how they contributed to the gravity modeling.

3.5 Gravity inversion: 3D mantle density shallower than 50 km

The residual gravity anomaly calculated for the initial 3D density model (Fig. 4.5c) provides the boundary condition for the inversion step: the Harvester algorithm (*Uieda and Barbosa*, 2011; *Uieda et al.*, 2013) iteratively approximates the inverse of the positive and negative anomalies of this residual by stepwise modifying the density distribution of the mantle at depths <50 km. This algorithm propagates initial density perturbations -the "seeds"- through a mesh of rectangular prisms with a defined reference density -the "medium"- until the corresponding forward gravity field reaches the prescribed boundary condition. In the present study, the "seeds" initially form a 1 km thick layer of which (i) the base is situated at a depth of 50 km and (ii) the density distribution is equal to the one at 50 km depth as derived from the V_{SH} data (Fig. 4.4b). The modified Harvester algorithm (*Meeßen et al.*, 2018) stepwise lets these "seeds" grow upwards, while the minimum top depth is constrained by the Moho. The "seeds" replace the "medium" in the upward direction, where the "medium" is (i) situated above the "seeds" and (ii) is assigned a constant density of 3300 kg/m^3 (a mantle density value typical at the depth of the Moho). The final thicknesses of the "seeds" and the "medium" (obtained when the residual gravity is minimized) define the average bulk density of the shallowest mantle. Hence, we have calculated the vertically averaged density of the mantle at depth of <50 km, by weighting the density of a "seed" and its overlying "medium" by their relative thicknesses for each column:

$$\rho_{average} = (t_m \cdot 3300 kg/m^3 + t_s \cdot \rho_s)/(t_m + t_s) \tag{3.6}$$

where $\rho_{average}$ and ρ_s represent the average mantle density at depths shallower than 50 km and the density of "seeds", while the t_m and t_s corresponds to the thickness of "medium" and "seeds", respectively.

Figure 4.6a presents the resulting average mantle density for depths shallower than 50 km. This configuration shows lower densities of <3220 kg/m^3 under the MKR and in an area close to Mohn's Ridge spreading axis, but significantly higher density (3250-3270 kg/m^3) in the middle northern part of the study area (red line in Fig. 4.6a). Then, we modified the initial 3D density model by substituting the homogeneous density of the shallowest mantle by the inverted average densities (Fig. 4.6a) and recalculated the gravity response of the entire model (using IGMAS+). This calculation results in the new residual gravity field shown by Figure 4.6b.

The residual gravity field (Fig. 4.6b; RMS: 20.37 mGal) shows that the middle northern parts of the study area are characterized by a large positive gravity residual anomaly (up to 70 mGal), which indicates mass excess in this domain. Because the density reduction of the upper 50 km of the mantle is restricted by the density of the seed, this prevents the uppermost mantle to obtain arbitrarily low densities, and thus there can still be residual anomalies after this first inversion step. This area of modeled mass excess is observed within the area of temperatures lower than 900°C (outlined by the red line in Fig. 4.6b), where the conversion to temperature and density has the largest uncertainties (*Priestley and McKenzie*, 2013). These uncertainties allow for changing the starting conditions for a second inversion run. In order to reduce the mass excess, the seed density was lowered from the 3210-3280 kg/m^3 range to a uniform 3210 kg/m^3 for this region, corresponding to 900°C at 50 km depth.

The average mantle density distribution from the second inversion run is shown in Figure 4.6c, and the corresponding residual in Figure 4.6d. As reflected in the initial residual gravity field (Fig. 4.5c), the mantle density below the MKR is characterized by a NE-SW trending anomaly of low density (3180-3200 kg/m^3) with densities gradually increasing perpendicular to this virtual axis. Interestingly, the NE-SW elongated mantle anomaly does not, however, coincide entirely with the NNE-SSW striking ridge axis. The NKR and nearby Eggvin Bank are characterized by intermediate mantle densities (3200-3240 kg/m^3). In the region of the Greenland basin, close to the Mohn's Ridge spreading axis, the average mantle density is around 3220 kg/m^3, slightly increasing to 3240 kg/m^3 away from the spreading axis, with a sharp increase to 3280 kg/m^3 at the COT. In addition, some relatively high mantle densities (3250 kg/m^3) are observed around the WJMFZ.
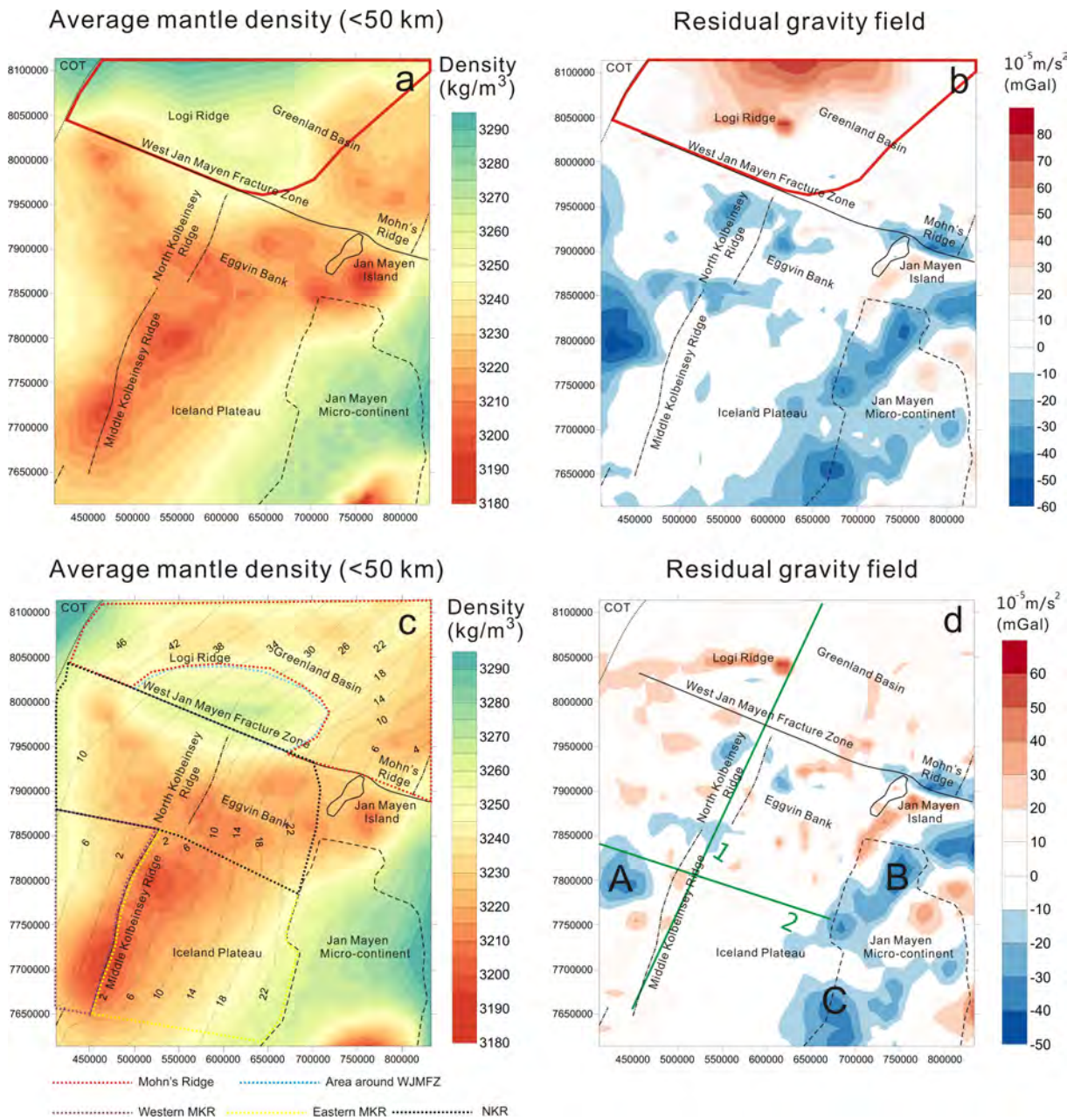
Figure 4.6: a, b: Results of first gravity inversion run. Average mantle density between the Moho and 50 km depth (a), and residual gravity field (b). For this inversion run, the density configuration of the "seeds" layer has been set equal to the V_s derived densities at 50 km depth (Fig. 4.4b). The red line delineates the area for which the estimated mantle temperature at 50 km depth is less than 900 °C (Fig. 4.4a). c, d: Results of second gravity inversion run. Average mantle density between Moho and 50 km depth (c), and residual gravity field (d). For the second inversion run, the maximum density of the "seed" layer has been set to 3210 kg/m^3 wich leads to a modification of the density model in the northern parts of the study area (red line in Fig. 4.6a). The solid gray lines with numbers show the oceanic seafloor ages (*Müller et al.*, 2008). Five different domains (Mohn's Ridge, area around WJMFZ, western MKR, eastern MKR, and NKR) are shown by color coded dotted lines. Two green lines show positions of the sections of Figs. 4.9-4.10. Points A-C represent the main residual anomalies.

141

The obtained gravity response of the density model shows a good fit with measured gravity (RMS: 15.34 mGal) (Fig. 4.6d). In the oceanic crustal domains, the long-wavelength NE-SW residual gravity anomaly (Fig. 4.5c) as well as the large positive gravity residual anomaly in the north (Fig. 4.6b) have been removed, and the majority of the final gravity residuals range between $\pm$ 10 mGal (Fig. 4.6d). However, some short-wavelength negative residuals (up to 30 mGal) are found in the northwestern parts of the MKR (Fig. 4.6d, point A). In addition, the northern (Fig. 4.6d, point B) and southwestern margins of the JMMC (Fig. 4.6d, point C) have negative residual anomalies with amplitudes up to 40 mGal.

3.6 Sensitivity analysis

For the sedimentary and crustal layers, the resolution of the model is controlled by the data coverage available for the regionally traceable interfaces. Areas where the initial sedimentary and crustal model derived its structure from interpolation across large distances have the greatest uncertainties. Thus, the most uncertain areas are most of the Eggvin Bank and western part of the NKR domain, while the MKR domain and Mohn's Ridge are better constrained. Compared to previous 3D gravity/seismic studies (*Hermann*, 2013; *Funck et al.*, 2016; *Haase et al.*, 2016), recently published seismic refraction and available reflection data allowed for some improvements with regard to the distribution of sediment (*Breivik et al.*, 2012b) around the Logi Ridge and the deep structure of the crystalline crust over the eastern part of the Eggvin Bank (*Tan et al.*, 2017).

We tested the sensitivity of the gravity response of the entire model with regard to both density and layer thickness variations. Our analyses focus on the differences between the three domains: MKR, NKR, and Mohn's Ridge (Fig. 4.6c). Table 4.3 gives an overview of the models tested and respective parameters changed. Concerning the depth of the oceanic basement (which is relatively well constrained due to the small amounts of sediments and good seismic coverage), we have tested the effects of (i) setting it equal to the bathymetry and (ii) shifting it downwards by 1.5 km. With the value chosen, we are testing an extreme scenario given that the uncertainty of this parameter typically is much smaller. For the top of the lower crust and the depth of the Moho, the Moho depth uncertainty of the the Eggvin Bank and western part of the NKR domain (less well covered by seismic data) is given as $\pm$3.0 km, while for the remaining parts it is $\pm$1.5 km (*Haase et al.*, 2016). We have assumed the same uncertainty values for the top of the lower crust. Concerning the density of sediments, we have tested an unrealistic endmember scenario by assuming a largely compacted sediment sequence with a density of 2650 kg/m^3. For

Table 4.3: Sensitivity analysis of various parameters of the sedimentary and crustal model on the gravity response and induced variation of the uppermost mantle density

Parameter		Imposed variations	Gravity response differences (mGal)			Uppermost mantle density variations (kg/m^3)		
			MKR	NKR	Mohn's	MKR	NKR	Mohn's
Z	Basement	Equal to bathymetry	2	2	10	<10	<10	<10
	Basement	+1.5 km	2	2	3	<10	<10	<10
	Top of lower oceanic crust	±1.5 km	∓20	∓20	∓20	<±10	<±10	<±10
	Top of lower oceanic crust*	±3 km		∓30			±20	
	Moho	±1.5 km	∓15	∓12	∓15	±10	±10	<±10
	Moho*	±3.0 km		∓20			±15	
ρ	Sediment	Assigned 2650kg/m^3	1	2	10	<10	<10	<10
	Upper oceanic crust	+20kg/m^3	20	20	15	10	10	<10
	Upper oceanic crust	-10kg/m^3	-10	-10	-8	<10	<10	<10
	Lower oceanic crust	±10kg/m^3	±25	±35	± 12	∓15	∓25	<∓10

* These parameters have been tested for two different values, respectively, to reflect the larger depth uncertainty in the less-constrained Eggvin Bank and western part of the NKR.

the sub-sedimentary crustal units, we have tested extreme density values as derived from literature values (Tab. 4.2).

For each of the models tested, we have calculated the gravity response and the difference with respect to our preferred model. These "gravity response differences" are represented by their average values in Table 4.3. Although we have tested extreme values for the different parameters, the overall range of response differences obtained is significantly smaller compared to the residual gravity distribution calculated for a homogeneous mantle at depths <50 km (Fig. 4.5c). In addition, changing the input parameters would result in the inverted upper-mantle densities to be changed by generally less than 10 kg/m^3 (except of the Eggvin Bank, where the crust is very thick and thus changes in lower crustal density might result in mantle density changes of up to 25 kg/m^3). Hence, we regard the pattern of heterogeneities in obtained uppermost mantle densities as robust.

In the MKR domain, the modeled uppermost mantle density anomaly increasingly deviates to the east of the spreading axis northwards (Fig. 4.6c). Checkerboard tests (Appendix A, Fig. 4.12) show that the anomalously low density is reasonably well resolved down to the dimensions we observe. These tests suggest that the density anomalies may be underestimated as the dimensions become smaller, but there is no lateral displacement involved in the inversion process. In addition, the initial residual gravity field (Fig. 4.5c), shows that the maximum gravity anomaly runs slightly east from the spreading axis, indicating lower density there. A forward gravity modeling shows that if we shift the low density zone in the preferred model back underneath the spreading axis, it will result in

~30 mGal residual gravity anomalies. Thus, we believe that the anomalously low density in the uppermost mantle is not an artifact of the gravity inversion process.

Figure. 4.5f shows that mantle density variations at depth of > 50 km mainly result in a long-wavelength gravity response, so that the change of the deeper mantle density would not remove the smaller scale anomalies in the upper 50 km. Also, the initial residual anomalies (Fig. 4.5c) do not spatially correlate with any of the subdomains (Fig. 4.2d). Therefore, treating the subdomains differently in terms of composition or temperature-density relation would not improve the overall fit.

4 Discussion

4.1 Model assessment

Density configuration of the sediments and crust

Compared to the final density configuration of the shallowest mantle (Fig. 4.6c), the residual gravity anomalies are of shorter wavelengths (Fig. 4.6d), which point to heterogeneities within the crust that are not resolved by the model. It is below the resolution of the data distribution (Table. 4.2). A short-wavelength residual gravity low (up to 40 mGal) is observed in the northwestern part of the MKR (point A; Fig. 4.6d). This is consistent with observed high-velocity lower crust (with densities of 3050-3100 kg/m^3) underlying this area (*Weigel et al.*, 1995; *Hermann and Jokat*, 2016). However, since the spatial constraints of this high density layer are limited, it cannot be adequately traced, and is not incorporated into the model.

In addition, some negative short-wavelength gravity residual anomalies (point B; Fig. 4.6d) could potentially be explained by mafic intrusions into the JMMC, also not in the model (e.g. *Peron-Pinvidic et al.*, 2012a,b; *Kodaira et al.*, 1998a; *Kandilarov et al.*, 2012; *Blischke et al.*, 2016). Another negative residual anomaly is restricted to the southwestern boundary of the JMMC, where there are no seismic refraction constraints (point C; Fig. 4.6d). Pre-breakup formation of the MKR is characterized by a long rifting period with significant conductive heat loss and accordingly not much magmatism generated (*Kodaira et al.*, 1998b; *Mjelde et al.*, 2008). The strong extension along the western boundary of the JMMC might have resulted in shallower Moho depths than used in the crustal model (Fig. 4.2d), which if implemented would improve the gravity fit there.

Gravity constrained mantle density between Moho and 50 km depth

There are some published 2D gravity models in the area based on seismic crustal con-straints, and a few also have additional velocity measurements of the uppermost mantle (*Voss and Jokat*, 2007; *Kandilarov et al.*, 2012, 2015; *Weigel et al.*, 1995; *Peron-Pinvidic et al.*, 2012a,b; *Hermann and Jokat*, 2016). However, none of these studies constrain the deeper velocity and hence the density of the mantle lithosphere, and thus cannot be di-rectly compared to our modeling results. The 3D model by *Haase et al.* (2016) solved the density structure of the lithosphere by forward temperature models based on lithsopheric age, and miss some of the plume-induced temperature variations that are clearly present.

In this study, the mantle density at depths <50 km is a result of gravity inversion, while mantle density at depths >50 km is derived from S-wave velocities. Despite the different types of constraints on density, there should be a reasonable continuity between the two. We have plotted average mantle density between 50 and 90 km (ρ_{50-90}) against the gravity-constrained density of the shallowest mantle for the entire oceanic domain (Fig. 4.7a). As being averages of large areas and variable depth ranges, there will not be a direct continuity of numerical values between the upper and lower part. The results from different domains should fall along trends, but the trends may differ between sub-regions. MKR domain has significantly lower ρ_{50-90} compared to the Mohn's Ridge, indicating the Iceland plume influence there. Despite the independence of constraints (S-wave velocity, respectively gravity) and the artificial, methodologically imposed separation of two mantle domains, there is a reasonable consistency of density anomaly trends between the two. However, for the Mohn's Ridge subregion where derived mantle temperatures at 50 km depth are <900°C and the accuracy of the V_s-to-T conversion is reduced (*Priestley and McKenzie*, 2006, 2013), there is a low correlation between the shallowest mantle density and the density at larger depths (ρ_{50-90}). Accordingly, the gravity-inverted densities are associated with larger uncertainties in this region.

In terms of density and temperature, the NKR takes an intermediate position between the MKR and the Mohn's Ridge, but the linear correlation between the shallow and deep mantle densities is much less pronounced. Therefore, factors other than temperature might control density variations in the NKR. A recent seismic study shows that the anomalously shallow NKR domain relates to thick crust (*Tan et al.*, 2017). Apart from this study, the crustal model in the Eggvin Bank and western part of the NKR domain are not well constrained, as it is derived from previous gravity inversion (*Haase et al.*, 2016). Therefore, both the less-constrained crustal model and a heterogeneous mantle
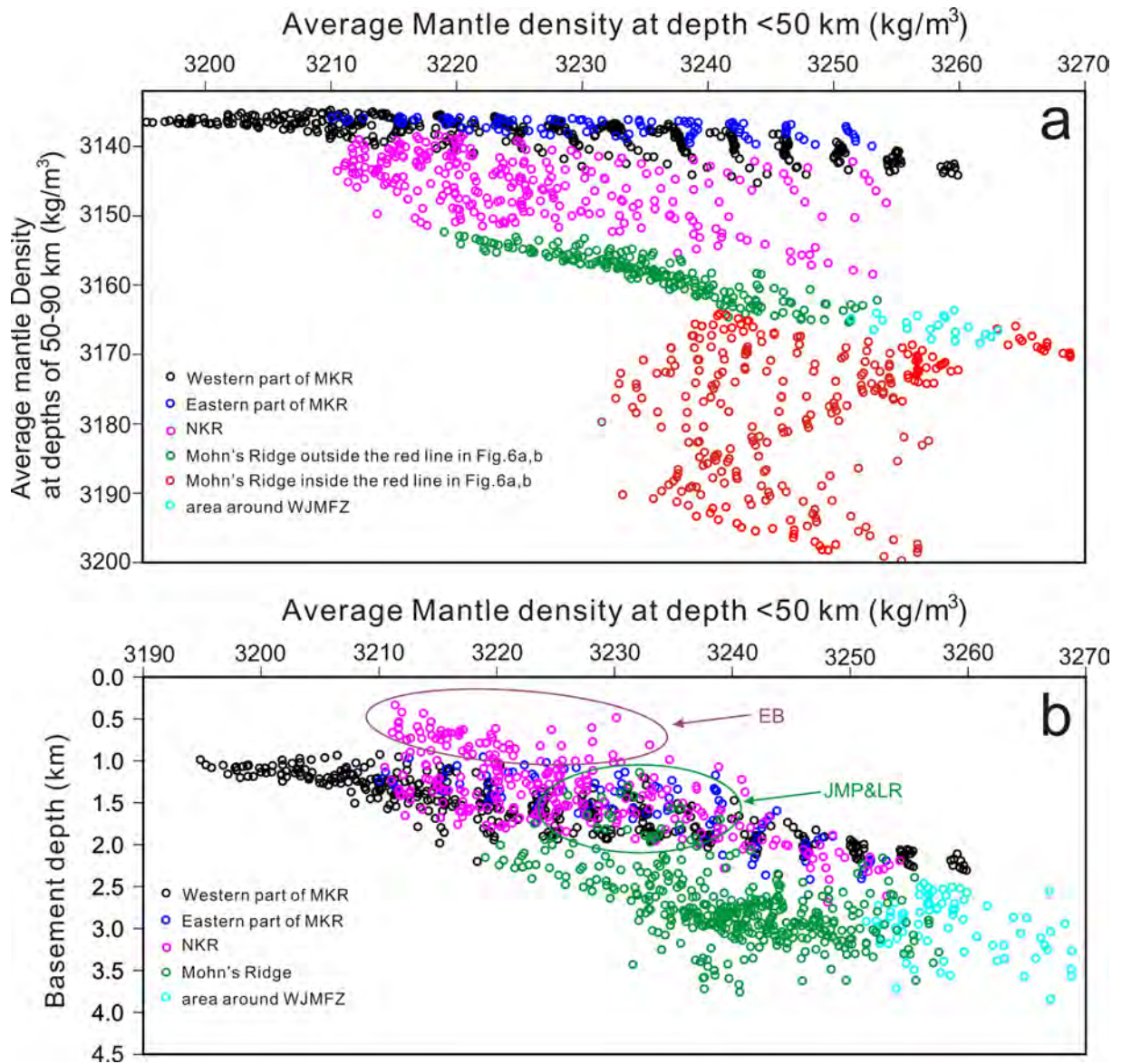
Figure 4.7:   a: Comparison of mantle density derived for different depths levels (<50 km and 50-90 km (ρ_{50-90}), respectively) with colours showing different sub-domains of the study area. Under the Mohn's Ridge, red dots represent ρ_{50-90} within the area of less than $900°C$ at 50 km depth (red line in Fig. 4.6a, b), while green dots indicate the ρ_{50-90} outside this sub-domain. b: Comparison of gravity-constrained mantle density (<50 km) and basement depth (corrected for sediments loading). Arrows indicate local geological features departing from the expected trends: Eggvin Bank (EB), Jan Mayen Plateau (JMP) and Logi Ridge(LR) (Fig. 4.1).

source under the NKR domain (e.g. *Haase et al.*, 2003) could contribute to the poorer correlation between ρ_{50-90} and average mantle density (<50 km) at the NKR domain.

Basement depth and topography/bathymetry are isostatically controlled by variations in the crustal thickness, upper mantle densities and sediment load (*Stein and Stein*, 1992). To calculate basement depth corrected for sediment loading (B_s), a standard Airy isostatic correction (*Le Douaran and Parsons*, 1982) was applied:

$$B_s = B + (\frac{\rho_w - \overline{\rho_s}}{\rho_a - \rho_w})Z_s \tag{4.1}$$

where B is the depth to the top basement (Fig. 4.2a), ρ_a is the density of asthenospheric mantle (3200 kg/m^3), ρ_w is the density of water (1030 kg/m^3), and Z_s is the thickness of the sediment units (Fig. 4.2b). The average density of the sedimentary column ($\overline{\rho_s}$) is calculated based on our crustal density model (Table 4.2).

Except for some oceanic islands and plateaus (e.g. Eggvin Bank, Logi Ridge), crustal thickness is relatively uniform within each of the three different domains (MKR: 8-9.5 km, NKR: 10-11 km, Mohn's Ridge: 3-5 km) (Fig. 4.2). Thus, we can discuss basement depths as being mostly controlled by mantle density variations within each domain. We have plotted corrected basement depth against gravity-constrained average mantle density at depths <50 km (Fig. 4.7b). Not surprisingly, the oceanic domain overall shows a positive correlation indicating that the study area is locally in isostatic equilibrium. Some deviations from the main trends (marked in the Fig. 4.7b) indicate local geological features with shallower bathymetry and thicker crust.

Basement depth of the oceanic plate corrected for sediment loading has a linear relation with the square root of the sea-floor age (Myr$^{1/2}$) if subsidence is controlled by passive thermal cooling only (e.g. *Stein and Stein*, 1992; *Adam and Vidal*, 2010). Linear regression shows a trend at the Mohn's Ridge of 300 m/Myr$^{1/2}$ (Fig. 4.8a), which is comparable to normal seafloor subsidence rate at 320 m/Myr$^{1/2}$ (*Korenaga*, 2008). However, the eastern MKR younger than 10 Ma shows a subsidence rate of about 230 m/Myr$^{1/2}$, while the subsidence rate for oceanic ages older than 10 Ma increases to around 390 m/Myr$^{1/2}$. The youngest western MKR has a subsidence rate of about 200 m/Myr$^{1/2}$, but increases to 490 m/Myr$^{1/2}$ for oceanic ages older than 4 Ma (Fig. 4.8a). Thus, the observed trends show a substantial deviation in mantle thermal structure compared to the theoretical half-space cooling model. The poor correlation between the basement depth and oceanic ages observed under the NKR domain is on the other hand, most likely related to large crustal thickness variations as mapped in the eastern NKR by *Tan et al.* (2017).
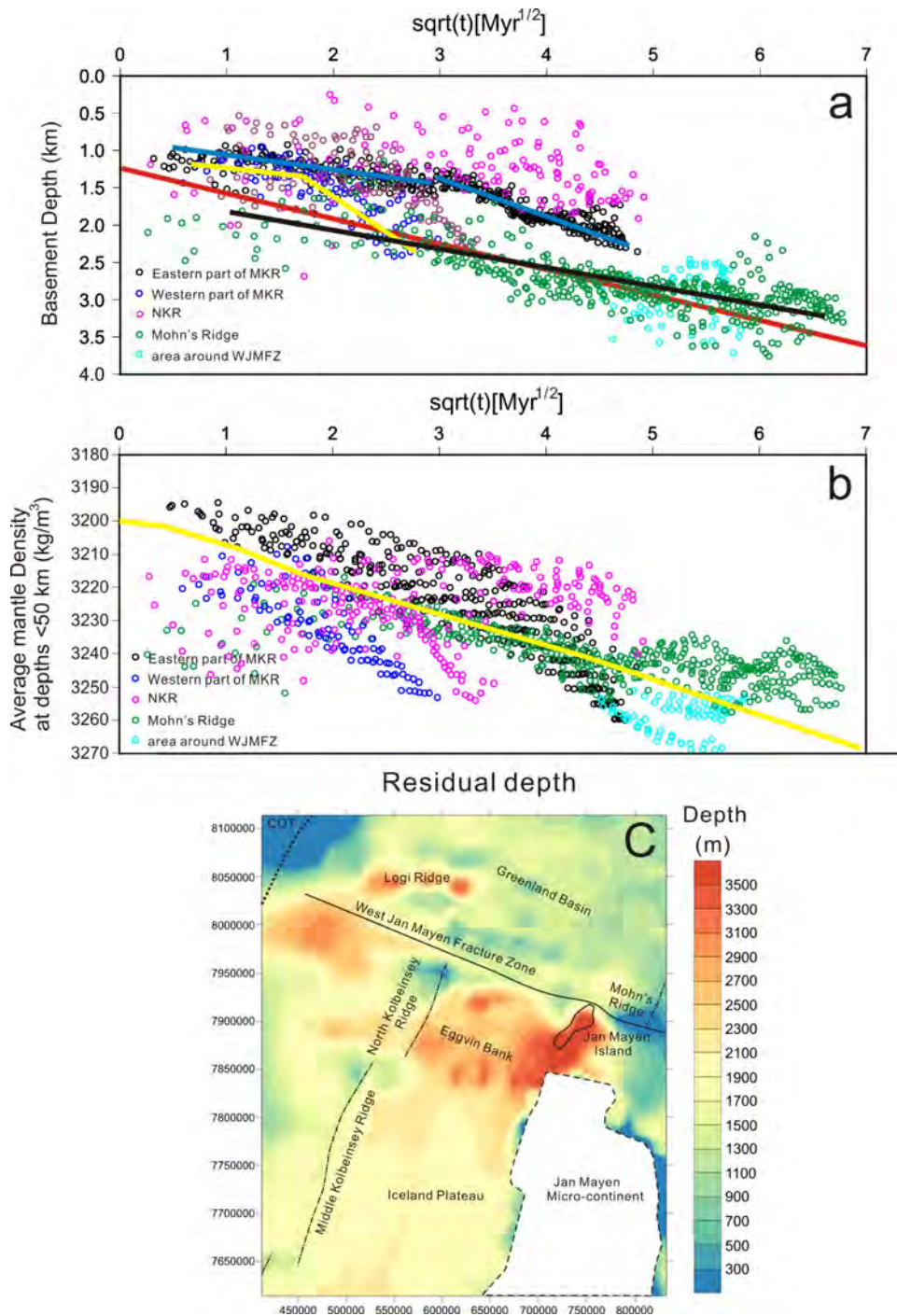
Figure 4.8: a: Observed basement depth (corrected for sediment load) against the square root of sea-floor age (*Müller et al.*, 2008)) for different sub-domains of the study area. Red solid line: a normal seafloor subsidence rate of 320 m/Myr$^{1/2}$ (*Korenaga*, 2008), blue line: eastern MKR, yellow line: western MKR, black line: Mohn's Ridge. b: Mantle density at depths <50 km against the square root of sea-floor age for different sub-domains of the study area. The yellow line illustrates the age-dependent average mantle density (<50 km) based on *Sandwell* (2001). c: Residual basement depth is corrected for sediment loading and subsidence with seafloor age using a seafloor subsidence rate at 320 m/Myr$^{1/2}$ and a spreading axis depth at 2600 m (*Stein and Stein*, 1992).

Similarly, the average mantle density <50 km depth derived from the half-space cooling model shows a positive trend with the square root of the sea-floor age (Myr$^{1/2}$) (Fig. 4.8b) (*Sandwell*, 2001). However, under the MKR domain the density distribution of the upper mantle (<50 km) differs somewhat from that, and is asymmetric with lower density east of the spreading axis (Figs. 4.8b,4.10). Consistent with the thermal subsidence deviation, the mantle density at eastern MKR domain for seafloor ages less than 10 Ma is slightly lower than expected from the half-space cooling model (yellow line in Fig. 4.8b). The yellow line shows the age-dependent average mantle density (<50 km) based on lithospheric thermal structure from *Sandwell* (2001) and conversion of these temperatures to density following the method in section 3.3.2. A sharp increase in mantle density is observed for seafloor ages older than 10 Ma (Fig. 4.8b). On the other hand, the density distribution of the Mohn's Ridge is similar to the half-space cooling model, which is consistent with little impact from the Iceland plume. The mantle density under the NKR domain has large variations and there is no correlation between the density and oceanic age (Fig. 4.8b). The lack of correlation is most likely related to a complex development where off-axis magmatic intrusions affect seafloor depth, and crustal thickness (*Tan et al.*, 2017).

To compare the uppermost mantle density to the basement variations, we show a map of basement depth corrected for sediment loading and age-controlled subsidence (assuming subsidence rate at 320 m/Myr$^{1/2}$ and depth of the spreading axis at 2600 m (*Stein and Stein*, 1992)) (Fig. 4.8c). The result shows that the residual basement of Mohn's Ridge has almost no variations, while in the northern parts of the MKR, the residual basement of the eastern part of the spreading ridge is about 300 m shallower than the remaining MKR domain, consistent with Figure 4.8b. Similarly, the eastern NKR is 600 m shallower than western part. The regions of shallow depths (> 2000 m) do largely correlate with regions of calculated average mantle density < 3250 kg/m^3 at depths less than 50 km (Fig. 4.6c).

An anomalously deeper residual basement of the western NKR allows for a colder mantle or a thinner crust. Isostatic analysis shows that 600 m deeper basement can be balanced by an increase of uppermost mantle density by 25 kg/m^3. This is consisted with our gravity-derived uppermost mantle density, where the difference between the average uppermost mantle density between the eastern (3220 kg/m^3) and western NKR (3240 kg/m^3) is 20 kg/m^3. Alternatively, the deeper residual basement could be caused by crustal thickness variations, where a 600 m deeper basement of the western NKR can be balanced by a decrease of Moho depth of about 1 km. However, a decrease of Moho depth of 1 km gives a decrease of uppermost mantle density < 10 kg/m^3 (Tab. 4.3). In this case,

the eastern NKR still needs less dense mantle compared to western part, indicating that this difference is a robust result.

Density configuration of the deeper mantle (>50 km)

The mantle temperature estimated from V_s has uncertainties, since the empirical relationship was derived from observations in the Pacific Ocean (*Priestley and McKenzie*, 2006). However, this relationship is comparable to that of a recent study of *Schoonman et al.* (2017), who postulate an empirical relationship between observed surface residual elevation, temperature and shear wave velocity for the mantle of northern Britain and western Norway. In addition, the V_s-derived temperature configuration (T_{50-90}; Fig. 4.4c) is indirectly validated by the observed crustal thickness (Fig. 4.2d). Accordingly, the crustal thickness difference between the present-day spreading axis of the MKR and Mohn's Ridge (4-4.5 km) (Fig. 4.2d) indicates that the mantle potential temperature under the MKR is elevated by about 75°C (*Ito and Lin*, 1995). This is consistent with the difference in the T_{50-90} around the present-day spreading axis of MKR (1350°C) and Mohn's Ridge (1270°C) which is 80°C (Fig. 4.4c).

Our Vs-temperature-density calculations are based on the assumption that the mantle composition is homogeneous. There appears to be a homogeneous, depleted mantle source under the MKR (e.g. *Elkins et al.*, 2011) and Mohn's Ridge (e.g. *Klingelhöfer et al.*, 2000a) but a heterogeneous enriched mantle under the NKR (e.g. *Haase et al.*, 2003). A variation of the mantle composition below the melt zone could affect V_s, producing discrepancies in derived mantle temperature, and accordingly mantle density estimates (*Goes and Van der Lee*, 2002). Several studies (*Priestley and McKenzie*, 2006, 2013; *Schutt and Lesher*, 2006), however, suggest that the mantle composition variations are difficult to resolve from seismic tomography. Moreover, the velocity anomalies caused by compositional changes are unlikely to exceed 1% (*Priestley and McKenzie*, 2006; *Schutt and Lesher*, 2006). A change in V_s of 0.04 km/s would result in a 40°C and 6 kg/m^3 difference at a temperature of 1300°C (Fig. 4.3). Sensitivity tests performed for the 3D density model presented here shows that a decrease of the mantle density at depth between 50 and 90 km by 1% under the MKR domain results in a gravity response with average 14 mGal difference. This indicates that the derived density heterogeneities at greater mantle depths (>50 km) exert minor control on the gravity field compared to shallower mantle and crustal structure.

The upper oceanic mantle density is also affected by melt extraction from the mantle beneath spreading ridges, causing chemical depletion of the residual solid (e.g. *Jha et al.*,

1994; *Oxburgh*, 1977; *Scott and Stevenson*, 1989; *Schutt and Lesher*, 2006). However, the part of the mantle that has undergone the highest melt degree by ascent through the whole melt zone is located in the shallowest part, and will mostly fall within the region where we invert for density, and the effect should therefore be incorporated in the modeling results.

Another uncertainty is the potential presence of a melt fraction within the mantle. *Priestley and McKenzie* (2006) argue that the fraction is generally small ($< 0.1\%$) and has little effect on the V_s to temperature conversion. While some authors argue that the low seismic velocities observed in the upper asthenosphere can be adequately explained without much melt (e.g. *Stixrude and Lithgow-Bertelloni*, 2005), other observations indicate that some unmobilized melt up to a few percent could be present locally (*Rychert and Shearer*, 2009; *Naif et al.*, 2013). The V_s model has low resolution, was sampled at a 100 km grid, and will not delineate the spreading ridges well. However, we note that the V_s distribution is reasonably well centered on the spreading ridges (Fig. 4.4a,c), which may be a combined effect of melt and elevated temperature. However, it is not obvious that a small melt fraction should affect the V_s significantly. The formation of melt would extract water from the mantle, which will increase the velocity of the solid. With fractional melting, the net effect could be a slight velocity increase in total (e.g. *Karato and Jung*, 1998). That the modeled low-density anomaly shows an increasing discrepancy from the spreading ridge position to the north, and correlates well with anomalously low seafloor subsidence (Fig. 4.8), suggests that it is not an artifact of the V_s to temperature conversion assumptions. The V_s-derived mantle density gives a long-wavelength density distribution (Fig. 4.5f) that cannot be predicted from the age of the oceanic lithosphere alone, and should improve the inversion results considerably. Absolute densities may be affected near the spreading ridges if retained melt changes the V_s-temperature relationship, but the trend of the uppermost mantle low density anomaly that we find should be robust.

4.2 Plume-lithosphere interaction

The WJMFZ represents a main mantle temperature contrast (Fig. 4.4c). North of the WJMFZ, the Greenland Basin is characterized by thinner crust, larger basement depth, higher mantle density, and lower mantle temperature compared to the NKR domain (Fig. 4.9). This is illustrated by calculating lithospheric thickness from the age-grid of *Müller et al.* (2008) using the approach of *Zhang and Lay* (1999) (Fig. 4.11). There is a significant thickness increase from the NKR to the Greenland Basin to the north. Approximately midway between the northern tip of the Kolbeisney Ridge and Jan Mayen,

the lithospheric thickness is predicted to be similar on both sides of the WJMFZ. Farther to the east, the lithoshere should be thinnest north of the WJMFZ, close to the Mohn's Ridge. Such steps in the lithosphere-asthenosphere boundary have been postulated to control the emplacement of plume material ("plume ponding", (*Sleep*, 1997)), and could potentially accumulate plume material from a northwards flow out from the Iceland plume under the Eggvin Bank, if the flow was strongly directed by the spreading ridge.

E.g. *Elkins et al.* (2016) and *Schilling* (1999) argue that excess magmatism in the NKR domain is caused by a putative Jan Mayen plume. However, *Mertz et al.* (2004) argue that the plume does not follow a simple time-transgressive track and cannot explain the radiogenic Nd-Pb isotope compositions of basalts from the NKR. The Eggvin Bank excess magmatism appears not to be governed by elevated temperature (*Haase et al.*, 2003), but by an enriched mantle component, probably over some time (*Tan et al.*, 2017), and at least does not require a thermal mantle plume. *Jones et al.* (2002) document V-shaped ridges along the Kolbeinsey Ridge up to the end of the middle segment, taken to indicate transport of mantle zones with variable temperature from the Iceland plume. It shows an apparent propagation speed that is still quite high in the northernmost part (100-150 mm/Ma) and a counter flow from a potential Jan Mayen plume is therefore not expected there.

South of the WJMFZ, the low-density anomaly of the Kolbeinsey Ridge is broad at depths between 50 and 90 km (ρ_{50-90}; Fig. 4.4c), while the shallow mantle density anomaly at depths of < 50 km is much narrower (Fig. 4.6c). In the south, it lies underneath the spreading ridge, and should reflect the cooling of the lithosphere as it moves away from the ridge. Judging from the 9-11 km oceanic crustal thickness south of our study area, it is also affected by hot plume material in the axial zone (*Hooft et al.*, 2006). However, the center of the low-density anomaly increasingly deviates to the east of the spreading ridge northwards. We interpret this deviation to be the effect of lithospheric heating from plume flow in the upper asthenosphere below (not resolved by the tomography model). In this sense, it represents thermal erosion of the lithosphere that will make the temperature structure and thickness deviate from what is expected from a passive cooling model based on age, as shown in Fig. 4.8. The obtained density model for the mantle shallower than 50 km will mostly encompass the lithosphere, and show this thermal influence. The lowest mantle densities from the model are contoured on top of the age-based lithospheric thickness grid in Fig. 4.11. The zone of lowest density passes under Jan Mayen towards the southern tip of the Mohn's Ridge. Thus, judging from the distribution of the lowest upper-mantle density, the asthenospheric flow below appears to avoid the lithospheric
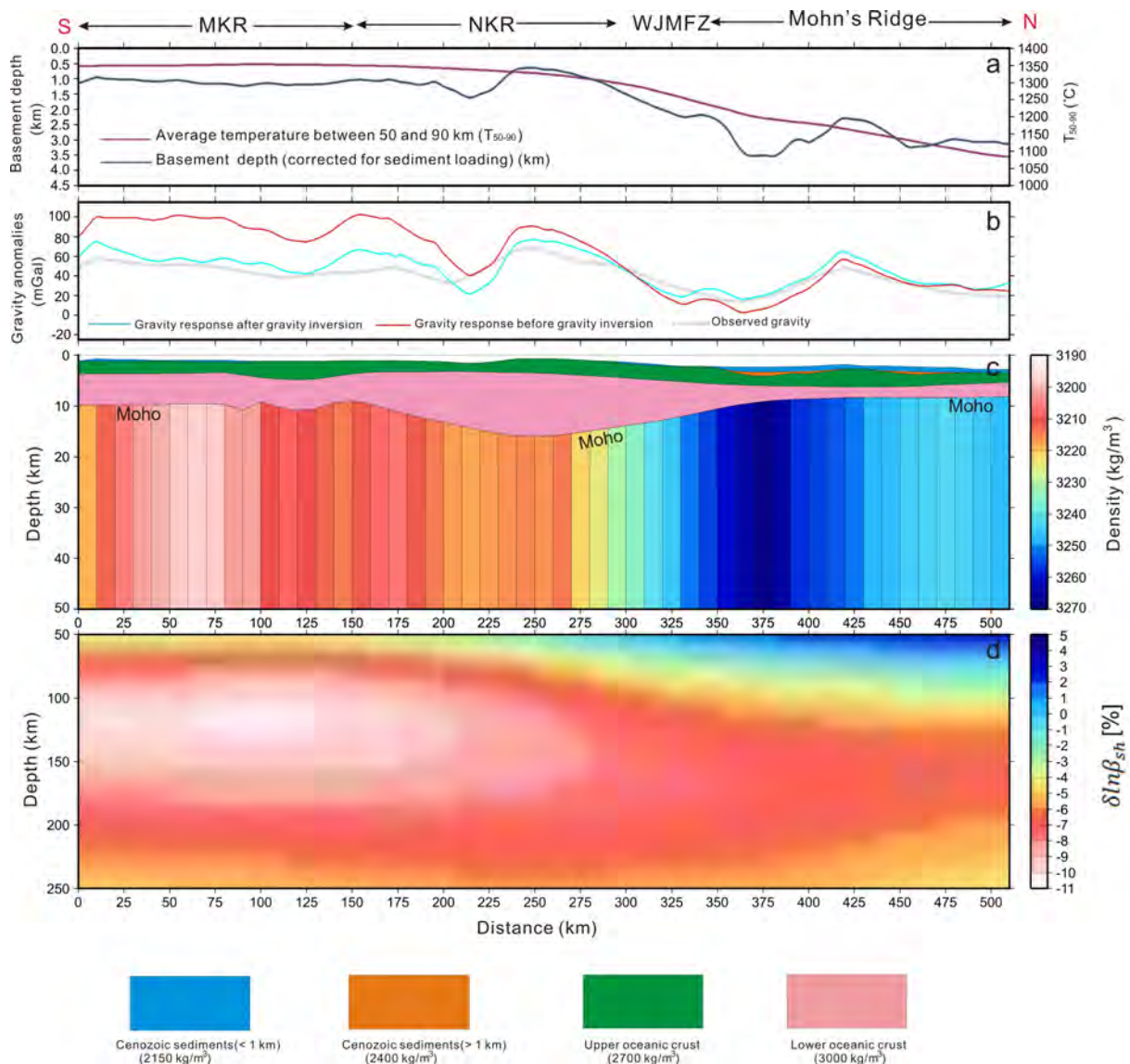
Figure 4.9: Results of the 3D gravity modeling along a N-S directed section through the study area (green line 1 in Fig. 4.6d). a: Basement depth and average mantle temperature (T_{50-90}) between 50 and 90 km depth (Fig. 4.4c). b: The corresponding observed and calculated gravity before and after gravity inversion. c: Vertical section through the 3D model with vertical average mantle density configuration between the Moho and 50 km depth (Fig. 4.4d). d: S-wave relative velocity perturbations ($\delta ln\beta_{sh}$ (%)) in the deeper mantle from *Rickers et al.* (2013). MKR: Middle Kolbeinsey Ridge, NKR: North Kolbeinsey Ridge, WJMFZ: Western Jan Mayen Fracture Zone.
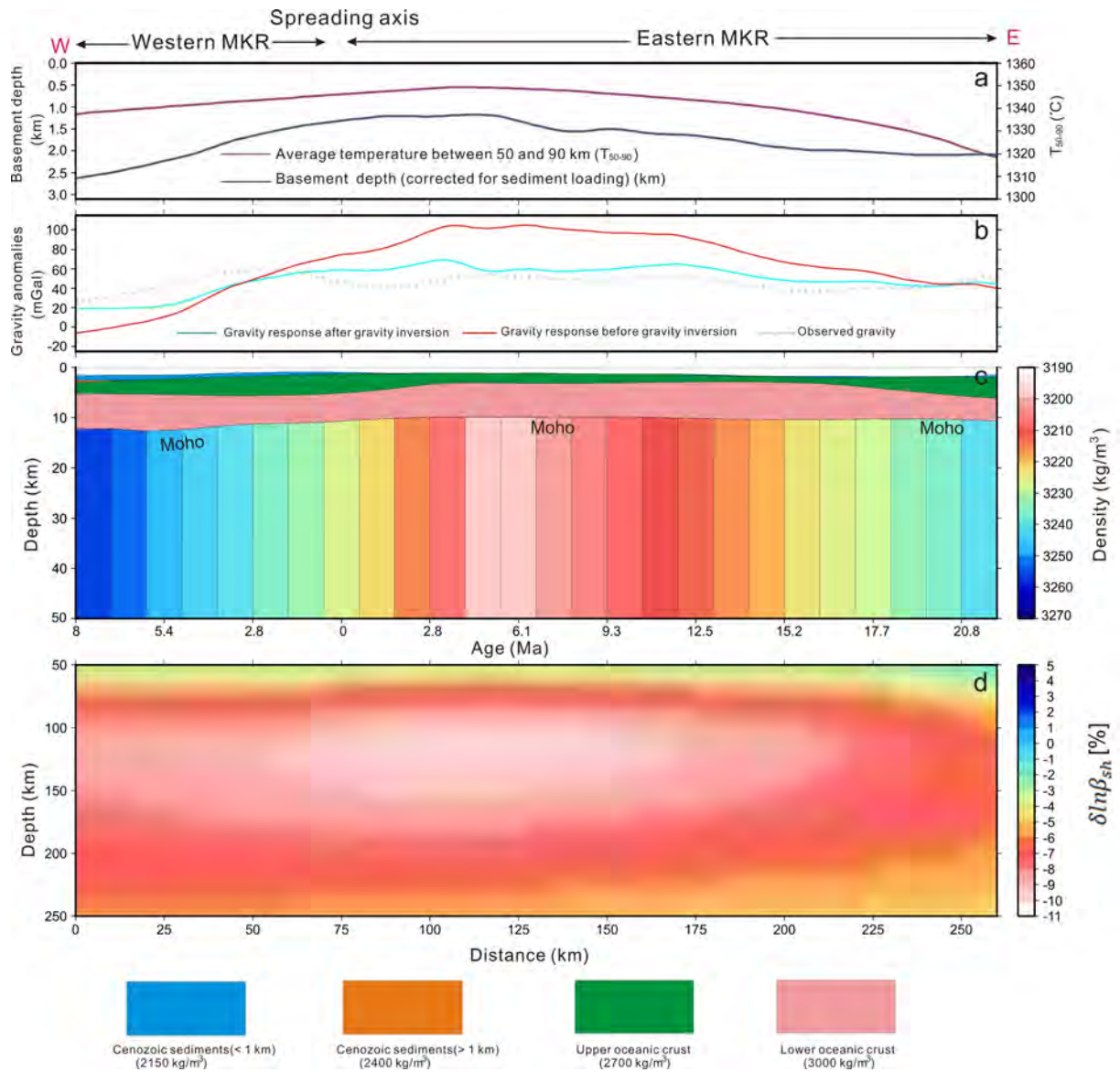
Figure 4.10: Results of the 3D gravity modeling along a W-E directed section through the study area (green line 2 in Fig. 4.6d). a: Basement depth and average mantle temperature (T_{50-90}) between 50 and 90 km depth (Fig. 4.4c). b: The corresponding observed and calculated gravity before and after gravity inversion. c: Vertical section through the 3D model with vertical average mantle density configuration between the Moho and 50 km depth (Fig. 4.4d). d: S-wave relative velocity perturbations ($\delta ln\beta_{sh}$ (%)) in the deeper mantle from *Rickers et al.* (2013). MKR: Middle Kolbeinsey Ridge.
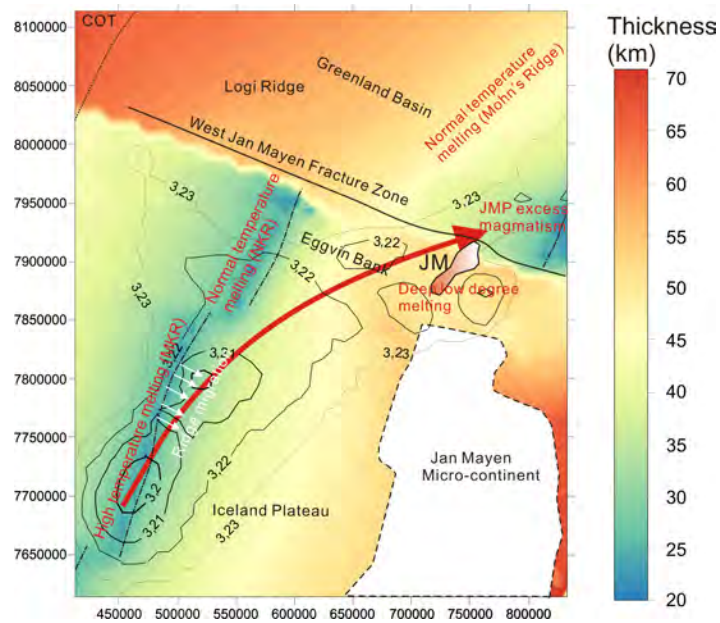
Figure 4.11: Estimated oceanic lithosphere thickness for the study area based on the crustal age model of *Müller et al.* (2008) using the approach of *Zhang and Lay* (1999). The solid black lines with numbers show contours of the uppermost mantle densities less than 3.23 g/cm^3, where thicker lines correspond to lower densities (Fig. 4.6c). JM: Jan Mayen, JMP: Jan Mayen Plateau.

thickness increase north of the Kolbeinsey Ridge, and is instead redirected farther east towards the region where there is no obstacle in lithospheric thickness, as indicated by the red arrow in Fig. 4.11. The eastward deviation of the uppermost asthenospheric flow may have existed for some time, as it correlates with other geological observations. In the south, the MKR axis underwent eastward ridge migration since approximately 5.5 Ma (*Appelgate*, 1997), following this deviation. Thus, the thermal erosion of the lithosphere on the east side of the MKR could be the driving force behind the eastwards axial relocations (Fig. 4.11). This redirection of the plume flow could also help to explain why the present spreading at the NKR does not appear to be influenced by elevated mantle temperature. Rather, it is known to be sourced from an enriched mantle component different from the MKR (e.g. *Haase et al.*, 2003; *Elkins et al.*, 2011, 2016). Thus, neither geochemical data, nor our results can confirm a model where ponding of northwards plume flow occurs against a lithospheric thickness increase at the northern end of the Kolbeinsey Ridge. While the upper asthenospheric plume flow appears to be influenced by spreading ridge location to some degree, it responds on a slightly larger, more regional scale, where it is determined by the change of lithospheric thickness north of the WJMFZ. Finally, we note that the flow passes underneath the presently volcanically active Jan Mayen island,

probably supplying the extra heat for a small degree of deep mantle melting to occur (*Trønnes et al.*, 1999) (Fig. 4.11). Also the oceanic crust around the southern tip of the Mohn's Ridge across the WJMFZ is thicker than normal, adjacent to the island on the same trend (*Kandilarov et al.*, 2012) (Figs. 4.1,4.11).

5 Summary and Conclusions

A three-dimensional structural and density model of the crust and upper mantle is developed for the greater Jan Mayen-East Greenland region, in order to determine the influence of the Iceland mantle plume on the area. We obtain the 3D density structure of the sedimentary cover and the crust down to the Moho mainly from regional reflection and refraction seismic lines. The mantle temperature and density structure (>50 km) is derived from an S-wave mantle tomography model (*Rickers et al.*, 2013), while the shallower mantle density (<50 km) is determined by 3D gravity inversion. The V_s derived mantle temperature and density show large variations at depths between 50 and 90 km. Based on present day spreading axis segmentation, we divided the study area into Middle Kolbeinsey Ridge (MKR), North Kolbeinsey Ridge (NKR), and Mohn's Ridge regions (Fig. 4.2d). In general, the model shows trends of decreasing T_{50-90} (increasing ρ_{50-90}) from MKR to NKR and to the Mohn's Ridge in the direction away from the plume.

The shallow mantle density trend (< 50 km depth) shows good correlation with the V_s constrained mantle density trends between 50 and 90 km (ρ_{50-90}) for most of the area. Compared to the MKR domain, the greater basement depth, denser shallowest mantle, and cooler mantle temperature (T_{50-90}) under the Mohn's Ridge, show much reduced plume influence here. The NKR, including the shallow Eggvin Bank, is bounded by two ridge offsets, where the WJMFZ has a long offset of 200 km, and represent a major lithospheric thickness contrast. Beneath the Kolbeinsey region, the low-density anomaly at depths of >50 km continues upwards into the uppermost mantle, where its lateral dimensions narrow considerably. In the south, it coincides well with the spreading ridge, but rotates clockwise away from the northern MKR and the NKR, towards the Mohn's Ridge when approaching the WJMFZ. This anomaly is interpreted to be the result of the Iceland plume flow to a large degree interacting with the base lithosphere topography on a regional scale. To some extent, the flow follows the spreading aixs, but the large offset of the WJMFZ appears to form an obstacle since the lithospheric thickness increases to the north of the tip of the Kolbeinsey Ridge. Instead, the flow is deviated eastwards toward the Mohn's Ridge, where the lithospheric thickness is similar or less

to the north of the WJMFZ. This results in a marked east-west asymmetry across the northern MKR, where the western domain is marked by higher mantle densities (<50 km) and a deeper top basement, which indicates lower lithospheric mantle temperature there. Under the eastern MKR domain, the low mantle density anomaly lies east of the present day ridge axis. This results in a significant departure from the half-space cooling model, and the plume-flow induced thermal erosion on the east side of the ridge may be the cause for several eastwards ridge relocations in the past 5.5 Ma (*Appelgate*, 1997). Also, the plume flow appears to deviate eastwards of the NKR, consistent with the present lack of elevated mantle temperature in the melt zone underneath the ridge (e.g. *Haase et al.*, 2003). Furthermore, it passes under the volcanically active Jan Mayen island, across the WJMFZ and towards the thick oceanic crust surrounding the southern tip of the Mohn's Ridge, and it likely cause for both.

6 Appendix A: Checkerboard test

To determine the resolution of the 3D gravity inverse model, we imposed a checkerboard pattern with a dimension of 125 km $\times$ 125 km, and a density perturbation of ± 50 kg/m^3 in the uppermost mantle (Fig. 4.12). This configuration is comparable to the regional anomalies we are investigating. The results show that the inversion has an even response over the model area, without lateral offsetting the anomalies. However, the ability to recover the true amplitude of density anomalies seems significantly reduced at this scale, but the lateral dimensions of the anomalies are clearly resolvable. In reality, we do not expect strong density contrasts anywhere near what was used in the checkerboard tests, and the modelled density anomalies are expected to be nearer to the true values than seen in these tests.
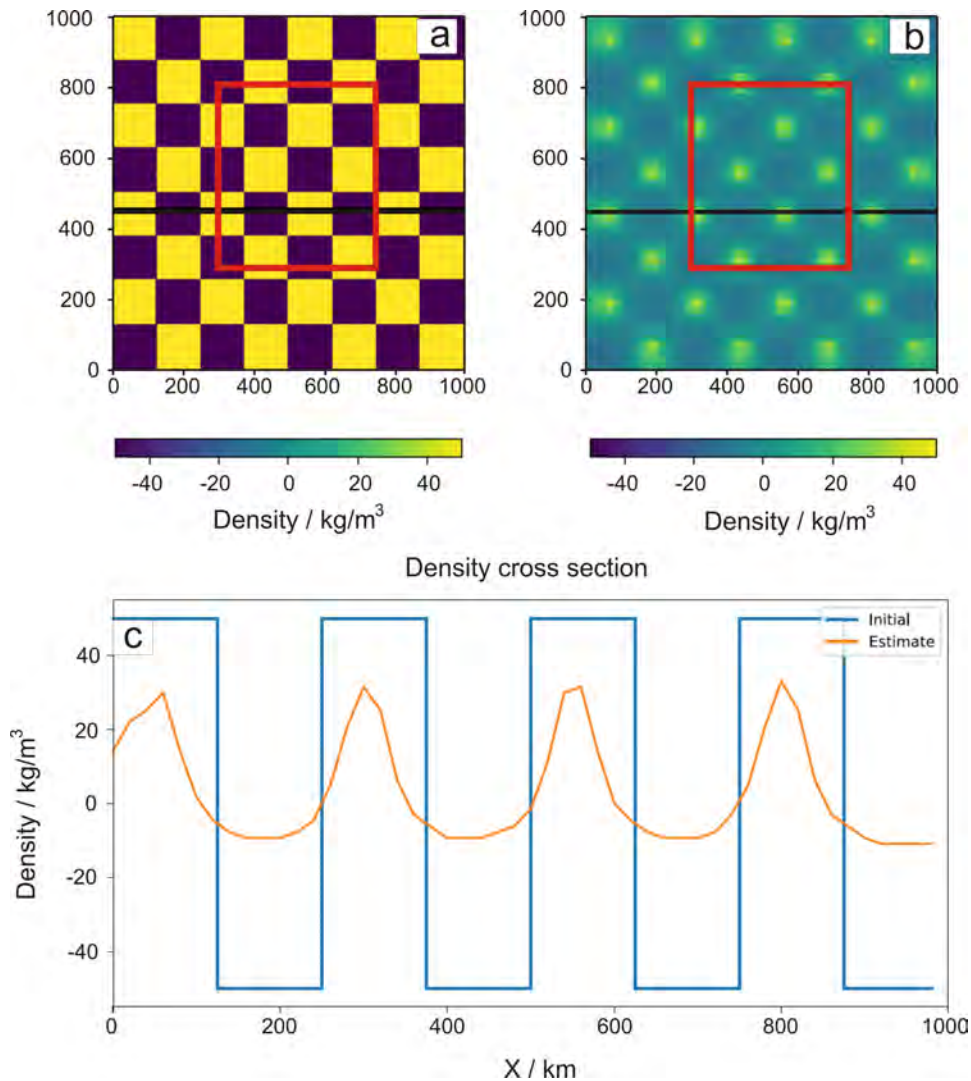
Figure 4.12: Checkerboard resolution test result performed using the gravity inversion algorithm "fatiando a terra" (*Uieda et al.*, 2013). (a) Input density perturbations of ± 50 kg/m^3 with cell of 125 km $\times$ 125 km. (b) Recovered density perturbations from the checkerboard tests. (c) Input density and recovered density perturbations along a section (black line) in Fig. 4.12a, b. Red boxes represent the size of our study area in relation to the extended model.

References

Adam, C., and V. Vidal (2010), Mantle flow drives the subsidence of oceanic plates, *Science*, *328*(5974), 83–85.

Andersen, O. B., P. Knudsen, and P. Berry (2010), The DNSC08GRA global marine gravity field from double retracked satellite altimetry models, *J. Geodesy*, *84*(3), doi: DOI:10.1007/s00190-009-0355-9.

Appelgate, B. (1997), Modes of axial reorganization on a slow-spreading ridge: The structural evolution of Kolbeinsey Ridge since 10 Ma, *Geology*, *25*, 431–434.

Bai, Y., S. E. Williams, R. D. Müller, Z. Liu, and M. Hosseinpour (2014), Mapping crustal thickness using marine gravity data: Methods and uncertainties, *Geophysics*, *79*(2), G27–G36.

Barton, P. J. (1986), The relationship between seismic velocity and density in the continental crust – A useful constraint?, *Geophys. J. R. Astron. Soc.*, *87*, 195–208.

Blischke, A., C. Gaina, J. R. Hopper, G. Péron-Pinvidic, B. Brandsdóttir, P. Guarnieri, O. Erlendsson, and K. Gunnarsson (2016), The Jan Mayen microcontinent: an update of its architecture, structural development and role during the transition from the Ægir Ridge to the mid-oceanic Kolbeinsey Ridge, *Geol. Soc. London Spec. Publ.*, *447*, doi: http://doi.org/10.1144/SP447.5.

Brandsdóttir, B., E. E. E. Hooft, R. Mjelde, and Y. Murai (2015), Origin and evolution of the Kolbeinsey Ridge and Iceland Plateau, N-Atlantic, *Geochem. Geophys. Geosyst.*, *16*, 612–634.

Breivik, A., R. Mjelde, J. I. Faleide, E. Flueh, and Y. Murai (2014), Magmatic development of the outer Vøring Margin from seismic data, *J. Geophys. Res.*, *119*, 6733–6755, doi:10.1002/2014JB011040.

References

Breivik, A. J., J. I. Faleide, and R. Mjelde (2008), Neogene magmatism northeast of the Aegir and Kolbeinsey Ridges, NE Atlantic: spreading ridge – mantle plume interaction?, *Geochem. Geophys. Geosyst.*, *9*(Q02004), doi:10.1029/2007GC001750.

Breivik, A. J., J. I. Faleide, R. Mjelde, and R. Flueh (2009), Magma productivity and early seafloor spreading rate correlation on the northern Vøring Margin, Norway – Constraints on mantle melting, *Tectonophysics*, *468*, 206–223, doi:10.1016/j.tecto.2008.09.020.

Breivik, A. J., R. Mjelde, J. I. Faleide, and Y. Murai (2012a), The eastern Jan Mayen microcontinent volcanic margin, *Geophys. J. Int.*, *188*, 798–818, doi:10.1111/j.1365-246X.2011.05307.x.

Breivik, A. J., R. Mjelde, A. K. Rai, and A. Frassetto (2012b), Geophyical survey of the Eggvin Bank and Logi Ridge-Greenland Sea, *Eos Trans. AGU*, *93*(52), Fall Meet. Suppl., Abstract T31B-2598.

Cammarano, F., and M. Guerri (2017), Global thermal models of the lithosphere, *Geophys. J. Int.*, *210*(1), 56–72.

Detrick, R., J. Collins, R. Stephen, and S. Swift (1994), In situ evidence for the nature of the seismic layer 2/3 boundary in oceanic crust, *Nature*, *370*, 288–290.

Dilek, Y. (1998), Structure and tectonics of intermediate-spread oceanic crust drilled at DSDP/ODP holes 504B and 896A, Costa Rica Rift, in Geolocial Evolution of Ocean Basin: Results From the Ocean Drilling Program, edited by A. Cramp et al., *Geol. Soc. Spec. Publ.*, *131*, 179–197.

Divins, D. L. (2004), Total sediment thickness of the world's oceans and marginal seas, World Data Cent. for Mar. Geol. and Geophys., Natl. Geophys. Data Cent., Boulder, Colo.

Doin, M. P., and L. Fleitout (1996), Thermal evolution of the oceanic lithosphere: an alternative view, *Earth Planet. Sci. Lett*, *142*(1-2), 121–136.

Elkins, L. J., K. W. W. Sims, J. Prytulak, T. Elliott, N. Mattielli, J. Blichert-Toft, J. Blusztajn, N. Dunbar, C. Devey, D. F. Mertz, J. G. Schilling, and M. Murrell (2011), Understanding melt generation beneath the slow-spreading Kolbeinsey Ridge using ^{238}U, ^{230}Th, and ^{231}Pa excesses, *Geochim. Cosmochim. Acta.*, *75*, 6300–6329.

Elkins, L. J., C. Hamelin, J. Blichert-Toft, S. R. Scott, K. W. W. Sims, I. A. Yeo, C. W. Devey, and R. B. Pedersen (2016), North Atlantic hotspot-ridge interaction near Jan Mayen Island, *Geochem. Persp. Lett.*, *2*, 55–67.

Fichtner, A., and J. Trampert (2011), Resolution analysis in full waveform inversion, *Geophys. J. Int.*, *187*(3), 1604–1624.

Funck, T., W. H. Geissler, G. S. Kimbell, S. Gradmann, M. K. Erlendsson, Ö, and U. K. Petersen (2016), Moho and basement depth in the NE Atlantic Ocean based on seismic refraction data and receiver functions, *Geol. Soc. Spec. Pub.*, *477*, doi:10.1144/SP447.1.

Furmall, A. V. (2010), Melt production and ridge geometry over the past 10 Myr on the southern Kolbeinsey Ridge, Iceland, Master's thesis, University of Oregon, USA.

Gaina, C., L. Gernigon, and P. Ball (2009), Palaeocene–Recent plate boundaries in the NE Atlantic and the formation of the Jan Mayen microcontinent, *J. Geol. Soc.*, *166*, 601–616, doi:10.1144/0016-76492008-112.

Gaina, C., S. C. Werner, R. Saltus, S. Maus, and T. C.-G. GROUP (2011), Circum-Arctic mapping project: new magnetic and gravity anomaly maps of the Arctic., *J. Geol. Soc.*, *35*, 39–48.

Goes, S., and S. Van der Lee (2002), Thermal structure of the north American uppermost mantle inferred from seismic tomography, *J. Geophys. Res.*, *107*(B3).

Götze, H. J., and B. Lahmeyer (1988), Application of three-dimensional interactive modeling in gravity and magnetics, *Geophyics*, *53*, 1096–1108.

Grose, C. J., and J. C. Afonso (2013), Comprehensive plate models for the thermal evolution of oceanic lithosphere, *Geochem. Geophys. Geosyst.*, *14*(9), 3751–3778.

Haase, C., J. Ebbing, and T. Funck (2016), A 3D crustal model of the NE Atlantic based on seismic and gravity data, *Geol. Soc. Spec. Pub.*, *447*.

Haase, K. M., C. W. Devey, and M. Wieneke (2003), Magmatic processes and mantle heterogeneity beneath the slow-spreading northern Kolbeinsey Ridge segment, North Atlantic, *Contrib. Mineral. Petrol.*, *144*, 428–448.

Hermann, T. (2013), The Northeast Greenland Margin-Tectonic Evolution, Ph.D. thesis, University of Jena.

References

Hermann, T., and W. Jokat (2016), Crustal structure off Kong Oscar Fjord, east Greenland: Evidence for focused melt supply along the Jan Mayen Fracture Zone, *Tectonophysics*, *691*, 110–119.

Hooft, E. E. E., B. Brandsdóttir, R. Mjelde, H. Shimamura, and Y. Murai (2006), Asymmetric plume ridge interaction around Iceland: The Kolbeinsey Ridge Iceland Seismic Experiment, *Geochem. Geophys. Geosyst.*, *7*(5), 1–26.

Howell, S. M., G. Ito, A. J. Breivik, A. Rai, R. Mjelde, B. Hanan, K. Sayit, and P. Vogt (2014), The origin of the asymmetry in the Iceland hotspot along the Mid-Atlantic Ridge from continental breakup to present-day, *Earth Planet. Sci. Lett.*, *392*, 143–153.

Huck, H. (2012), The Road to Open Source: Sharing a Ten Years Experience in Building OpendTect, the Open Source Seismic Interpretation Software, in *74th EAGE Conference and Exhibition-Workshops*.

Ito, G. (2001), Reykjanes 'V'-shaped ridges originating from a pulsing and dehydrating mantle plume, *Nature*, *411*, 681–684.

Ito, G. T., and J. Lin (1995), Mantle temperature anomalies along the past and paleoaxes of the Galápagos spreading center as inferred from gravity analyses, *J. Geophys. Res.*, *100*(B3), 3733–3745.

Jacobson, R. S. (1992), Impact of crustal evolution on changes of the seismic properties of the uppermost oceanic crust, *Rev. Geophys.*, *30*(1), 23–42.

Jakobsson, M., L. A. Mayer, B. Coakley, J. A. Dowdeswell, S. Forbes, B. Fridman, H. Hodnesdal, R. Noormets, R. Pedersen, M. Rebesco, H.-W. Schenke, Y. Zarayskaya, A. D. Accettella, A. Armstrong, R. M. Anderson, P. Bienhoff, A. Camerlenghi, I. Church, M. Edwards, J. V. Gardner, J. K. Hall, B. Hell, O. B. Hestvik, Y. Kristoffersen, C. Marcussen, R. Mohammad, D. Mosher, S. V. Nghiem, M. T. Pedrosa, P. G. Travaglini, and P. Weatherall (2012), International Bathymetric Chart of the Arctic Ocean (IBCAO) Version 3.0, *Geophys. Res. Lett.*, *39*(L12609), doi:10.1029/2012GL052219.

Jha, K., E. M. Parmentier, and J. P. Morgan (1994), The role of mantle-depletion and melt-retention buoyancy in spreading-center segmentation, *Earth. Planet. Sci. Lett.*, *125*(1-4), 221–234.

Jones, S. M., N. White, and J. Maclennan (2002), V-shaped ridges around Iceland: Implications for spatial and temporal patterns of mantle convection, *Geochem. Geophys. Geosyst.*, *3*(10), 1059, doi:10.1029/2002GC000361.

Kandilarov, A., R. Mjelde, R. B. Pedersen, B. Hellevang, C. Papenberg, C. J. Petersen, L. Planert, and E. Flueh (2012), The northern boundary of the Jan Mayen Microcontinent, North Atlantic determined from ocean bottom seismic, multichannel seismic, and gravity data, *Mar. Geophys. Res.*, *33*(1), 55–76.

Kandilarov, A., R. Mjelde, E. Flueh, and R. B. Pedersen (2015), V_p/V_s-ratios and anisotropy on the northern Jan Mayen Ridge, North Atlantic, determined from ocean bottom seismic data, *Polar Sci.*, *9*(3), 293–310.

Karato, S., and H. Jung (1998), Water, partial melting and the origin of the seismic low velocity and high attenuation zone in the upper mantle, *Earth Planet. Sci. Lett.*, *157*, 193–207.

Klingelhöfer, F., L. Géli, and R. S. White (2000a), Geophysical and geochemical constraints on crustal accretion at the very-slow spreading Mohns Ridge, *Geophys. Res. Lett.*, *27*(10), 1547–1550.

Klingelhöfer, F., L. Géli, L. Matias, N. Steinsland, and J. Mohr (2000b), Crustal structure of a super-slow spreading centre: a seismic refraction study of Mohns Ridge, 72°N, *Geophys. J. Int.*, *141*, 509–526.

Kodaira, S., R. Mjelde, H. Shimamura, K. Gunnarsson, and H. Shiobara (1997), Crustal structure of the Kolbeinsey Ridge, N. Atlantic, obtained by use of Ocean Bottom Seismographs, *J. Geophys. Res.*, *102*(B2), 3131–3151.

Kodaira, S., R. Mjelde, K. Gunnarsson, H. Shiobara, and H. Shimamura (1998a), Structure of the Jan Mayen microcontinent and implication for its evolution, *Geophys. J. Int.*, *132*, 383–400.

Kodaira, S., R. Mjelde, K. Gunnarsson, H. Shiobara, and H. Shimamura (1998b), Evolution of oceanic crust on the Kolbeinsey Ridge, north of Iceland, over the past 22 Myr, *Terra Nova*, *10*, 27–31.

Koptev, A., S. Cloetingh, E. Burov, T. François, and T. Gerya (2017), Long-distance impact of Iceland plume on Norway's rifted margin, *Sci. Rep.*, *7*.

References

Korenaga, J. (2008), Urey ratio and the structure and evolution of Earth's mantle, *Rev. Geophys.*, *46*(2).

Kroll, H., A. Kirfel, R. Heinemann, and B. Barbier (2012), Volume thermal expansion and related thermophysical parameters in the Mg, Fe olivine solid-solution series, *Eur. J. Mineral.*, *24*(6), 935–956.

Laske, G., G. Masters, Z. Ma, and M. Pasyanos (2013), Update on CRUST 1.0- A 1-degree Global Model of Earth's Crust., *Geophys. Res. Abstracts*, *15*, abstract EGU2013-2658.

Le Douaran, S., and B. Parsons (1982), A note on the correction of ocean floor depths for sediment loading, *J. Geophys. Res. Solid Earth*, *87*(B6), 4715–4722.

Marquart, G., H. Schmeling, and O. Čadek (2007), Dynamic models for mantle flow and seismic anisotropy in the North Atlantic region and comparison with observations, *Geochem. Geophys. Geosyst.*, *8*(2).

Meeßen, C., J. Sippel, M. Scheck-Wenderoth, C. Heine, and M. R. Strecker (2018), Crustal Structure of the Andean Foreland in Northern Argentina: Results From Data-Integrative Three-Dimensional Density Modeling, *J. Geophys. Res.: Solid Earth*, *123*(2), 1875–1903.

Mertz, D. F., W. D. Sharp, and K. M. Haase (2004), Volcanism on the Eggvin Bank (Central Norwegian-Greenland Sea, latitude ∼71°N): age, source, and relationship to the Iceland and putative Jan Mayen plumes, *J. Geodyn.*, *38*, 57–83, doi:10.1016/j.jog.2004.03.003.

Mjelde, R., R. Aurvåg, S. Kodaira, H. Shimamura, K. Gunnarsson, A. Nakanishi, and H. Shiobara (2002), Vp/Vs-ratios from the central Kolbeinsey Ridge to the Jan Mayen Basin, North Atlantic; implications for lithology, porosity and present-day stress field, *Mar. Geophys. Res.*, *23*(2), 123–145.

Mjelde, R., I. Eckhoff, S. Solbakken, S. Kodaira, H. Shimamura, K. Gunnarsson, A. Nakanishi, and H. Shiobara (2007), Gravity and S-wave modeling across the Jan Mayen Ridge, North Atlantic; implications for crustal lithology and continental break-up processes, *Mar. Geophys. Res.*, *28*, 27–41, doi:10.1007/s11001-006-9012-3.

Mjelde, R., T. Raum, A. J. Breivik, and J. I. Faleide (2008), Crustal transect across the North Atlantic, *Mar. Geophys. Res.*, *29*, 73–87, doi:10.1007/s11001-008-9046-9.

Müller, R. D., M. Sdrolias, C. Gaina, and W. R. Roest (2008), Age, spreading rates, and spreading asymmetry of the world's ocean crust, *Geochem, Geophys. Geosyst.*, *9*(4).

Naif, S., K. Key, S. Constable, and R. L. Evans (2013), Melt-rich channel observed at the lithosphere-asthenosphere boundary, *Nature*, *495*, 356–359, doi:10.1038/nature11939.

National Geophysical Data Center (2006), 2-minute gridded global relief data (ETOPO2) v2. National Geophysical Data Center, NOAA, doi:10.7289/V5J1012Q.

Nunns, A. (1982), The structure and evolution of the Jan Mayen Ridge and surrounding regions, in *Studies in continental margin geology*, vol. 34, edited by J. S. Watkins and C. L. Drake, pp. 193–208, Am. Assoc. Petrol. Geol., Tulsa, Oklahoma, USA.

Olesen, O., J. Ebbing, E. Lundin, E. Mauring, J. R. Skilbrei, T. H. Torsvik, E. K. Hansen, T. Henningsen, P. Midbøe, and M. Sand (2007), An improved tectonic model for the Eocene opening of the Norwegian-Greenland Sea: Use of modern magnetic data, *Mar. Petrol. Geol.*, *24*, 53–66, doi:10.1016/j.marpetgeo.2006.10.008.

Oxburgh, E. M., E. R.and Parmentier (1977), Compositional and density stratification in oceanic lithosphere-causes and consequences, *J. Geol. Soc., London*, *133*(4), 343–355.

Parnell-Turner, R., N. White, T. Henstock, B. Murton, J. Maclennan, and S. M. Jones (2014), A continuous 55-million-year record of transient mantle plume activity beneath Iceland, *Nat. Geosci.*, *7*(12), 914–919.

Peron-Pinvidic, G., L. Gernigon, C. Gaina, and P. Ball (2012a), Insights from the Jan Mayen system in the Norwegian-Greenland sea-I. Mapping of a microcontinent, *Geophys. J. Int.*, *191*, 385–412.

Peron-Pinvidic, G., L. Gernigon, C. Gaina, and P. Ball (2012b), Insights from the Jan Mayen system in the Norwegian-Greenland sea-II. Architecture of a microcontinent, *Geophys. J. Int.*, *191*, 413–435.

Pilidou, S., K. Priestley, E. Debayle, and O. Gudmundsson. (2005), Rayleigh wave tomography in the North Atlantic: high resolution images of the Iceland, Azores and Eifel mantle plumes, *Lithos.*, *79*, 453–474.

Priestley, K., and D. McKenzie (2006), The thermal structure of the lithosphere from shear wave velocities, *Earth Planet. Sci. Lett.*, *244*, 285–301.

References

Priestley, K., and D. McKenzie (2013), The relationship between shear wave velocity, temperature, attenuation and viscosity in the shallow part of the mantle, *Earth Planet. Sci. Lett.*, *381*, 78–91.

QGIS Devlopment Team (2009), *QGIS Geographic Information System*, Open Source Geospatial Foundation.

Rickers, F., A. Fichtner, and J. Trampert (2013), The Iceland Jan Mayen plume system and its impact on mantle dynamics in the North Atlantic region: Evidence from full-waveform inversion., *Earth Planet. Sci. Lett*, *367*, 39–51.

Ritsema, J., H. J. van Heist, and J. H. Woodhouse (1999), Complex shear wave velocity structure imaged beneath Africa and Iceland, *Science*, *286*, 1925–1928.

Rychert, C. A., and P. M. Shearer (2009), A global view of the lithosphere-asthenosphere boundary, *Science*, *324*(5926), 495–498.

Sandstå, R., N, R. B. Pedersen, R. Williams, D. Bering, M. Magnus, M. Sand, and H. Brekke (2012), Submarine Fieldwork on the Jan Mayen Ridge: Integrated Seismic and ROV-Sampling. Norwegian Petroleum Directorate, Stavanger, Norway.

Sandwell, D. T. (2001), Cooling of the oceanic lithosphere and ocean floor topography. University of California, San Diego, CA, USA.

Sandwell, D. T., R. D. Müller, W. H. Smith, E. Garcia, and R. Francis (2014), New global marine gravity model from CryoSat-2 and Jason-1 reveals buried tectonic structure, *Science*, *346*(6205), 65–67.

Schilling, J. (1999), Dispersion of the Jan Mayen and Iceland mantle plumes in the Arctic: A He-Pb-Nd-Sr isotope tracer study of basalts from the Kolbeinsey, Mohns, and Knipovich Ridges, *J. Geophys. Res.*, *104*, 10,543–10,569.

Schmidt, S., and H. J. Götze (1998), Interactive visualization and modification of 3-D models using GIS functions., *Phys. Chem. Earth*, *23*, 289–296.

Schmidt, S., C. Plonka, H.-J. Götze, and B. Lahmeyer (2011), Hybrid modelling of gravity, gravity gradients and magnetic fields, *Geophys. Prospect.*, *59*(6), 1046–1051.

Schoonman, C. M., N. J. White, and D. Pritchard (2017), Radial viscous fingering of hot asthenosphere within the Icelandic plume beneath the North Atlantic Ocean, *Earth Planet. Sci. Lett.*, *468*, 51–61.

Schutt, D. L., and C. E. Lesher (2006), Effects of melt depletion on the density and seismic velocity of garnet and spinel Iherzolite, *J. Geophys. Res.*, *111*, B05,401.

Scott, D. R., and D. Stevenson (1989), A self-consistent model of melting, magma migration and buoyancy-driven circulation beneath mid-ocean ridges, *J. Geophys. Res.*, *94* (B3), 2973–2988.

Shorttle, O., J. Maclennan, and S. M. Jones (2010), Control of the symmetry of plume-ridge interaction by spreading ridge geometry, *Geochem. Geophys. Geosyst.*, *11* (7).

Sleep, N. H. (1997), Lateral flow and ponding of starting plume material, *J. Geophys. Res.*, *102* (B5), 10,001–10,012.

Stein, C. A., and S. Stein (1992), A model for the global variation in oceanic depth and heat flow with lithospheric age, *Nature*, *359*, 123–129.

Stixrude, L., and C. Lithgow-Bertelloni (2005), Mineralogy and elasticity of the oceanic upper mantle: Origin of the low-velocity zone, *J. Geophys. Res.*, *110* (B03204), doi: 10.1029/2004JB002965.

Tan, P., A. J. Breivik, R. G. Trønnes, R. Mjelde, R. Azuma, and S. Eide (2017), Crustal structure and origin of the Eggvin Bank west of Jan Mayen, NE Atlantic, *J. Geophys. Res: Solid Earth.*, *122*, 43–62, doi:10.1002/2016JB013495, 2016JB013495.

Thiede, J., and G. Hempel (1991), Die Expedition ARKTIS-VII/1 mit FS "Polarstern", *Rep. Polar. Res.*, pp. 1–137.

Trønnes, R. G., S. Planke, B. Sundvoll, and P. Imsland (1999), Recent volcanic rocks from Jan Mayen: Low-degree melt fractions of enriched northeast Atlantic mantle, *J. Geophys. Res.*, *104* (B4), 7153–7168.

Uieda, L., and V. C. F. Barbosa (2011), 3D gravity inversion by planting anomalous densities, in *SBGf 2011 Expanded Abstracts*.

Uieda, L., V. C. Oliveira J., and V. C. Barbosa (2013), Modeling the Earth with fatiando a terra, in *Proceedings of the 12th Python in Science Conference (SciPy 2013)*, pp. 96–103.

Voss, M., and W. Jokat (2007), Continent-ocean transition and voluminous magmatic underplating derived from P-wave velocity of the East Greenland continental margin, *Geophys. J. Int.*, *170*, 580–604, doi:10.1111/j.1365-246X.2007.03438.x.

References

Weigel, W., E. R. Flüh, H. Miller, a. Butzke, G. a. Dehghani, V. Gebhardt, I. Harder, J. Hepper, W. Jokat, D. Kläschen, S. Kreymann, S. Schüßler, and Z. Zhao (1995), Investigations of the East Greenland continental margin between 70° and 72°N by deep seismic sounding and gravity studies, *Mar. Geophys.*, *17*, 167–199.

White, R. S., J. W. Bown, and J. R. Smallwood (1995), The temperature of the Iceland plume and origin of outward-propagating V-shaped ridges, *J. Geol. Soc.*, *152*, 1039–1045.

Xue, M., and R. M. Allen (2005), Asthenospheric channeling of the Icelandic upwelling: Evidence from seismic anisotropy, *Earth Planet. Sci. Lett.*, *235*, 167–182.

Zhang, Y., and T. Lay (1999), Evolution of oceanic upper mantle structure, *Phys Earth. Planet. In.*, *114*, 71–80.